esoscale Weather Systems of the Central United States

M.A. Shapiro

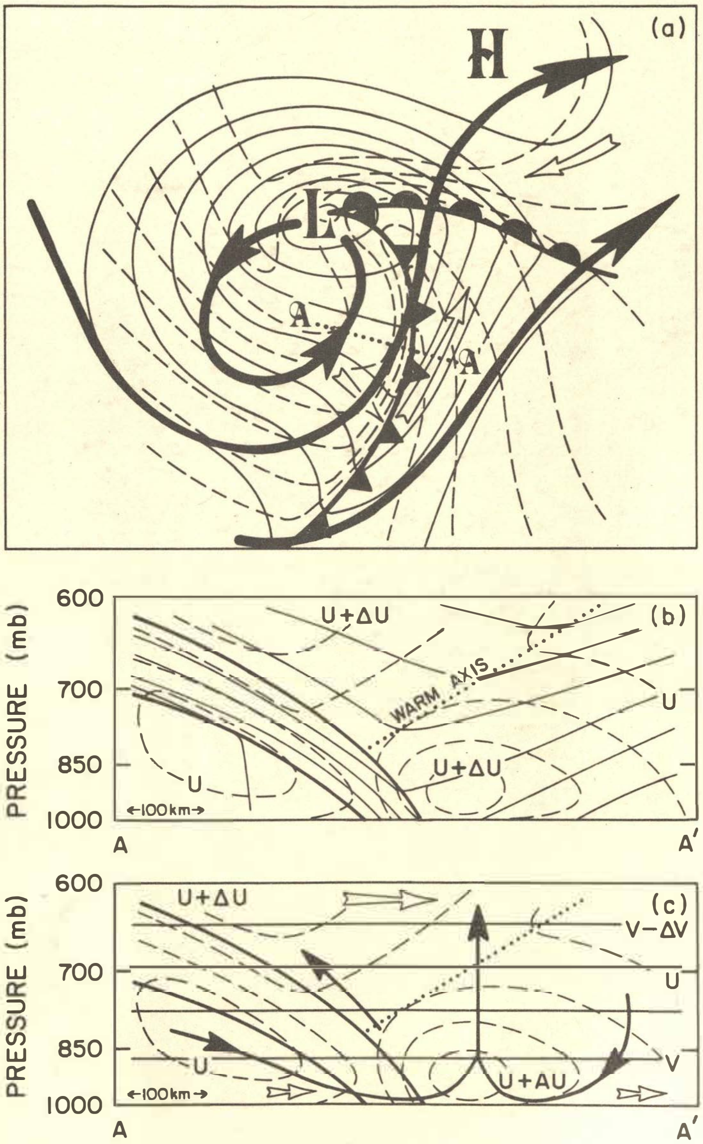

Cooperative Institute for Research in Environmental Sciences(CIRES)
National Oceanic and Atmospheric Administration(NOAA)
University of Colorado
Boulder, Colorado, U.S.A. 80309

Mesoscale Weather Systems of the Central United States

M.A. Shapiro

Cooperative Institute for Research
in Environmental Sciences (CIRES)
University of Colorado/NOAA
Boulder, Colorado 80309

August 1982

Table of Contents

Preface

This document presents a review of observations and theory of selected mesoscale phenomena which occur within, but are not necessarily exclusive to, the central region of the United States. This work originally appeared within the theoretical and phenomenological chapters of The National STORM Program,[1] a report which summarized our current understanding and the future directions in the observation, theory, modeling and prediction of mesoscale weather systems. At the suggestion of my university colleagues, I have extracted my contributions from the STORM report and consolidated them into the present document so that they may be used as an educational aid to graduate courses on mesoscale meteorological processes.

---

[1] The National STORM Program: Scientific and technical bases and major objectives. University Corporation for Atmospheric Research, 1982, Boulder, Colorado 80307.

The author's support for this contribution to the STORM document was provided through a contract between NOAA and UCAR (contract #NA81RAC00123).

1. Introduction

The central United States experiences a wide variety of mesoscale weather systems which occasionally produce severe weather events. The diversity of these systems is related, in part, to the diversity of the geography across the region. At the western edge, the Rocky Mountains act not only to force the planetary-scale (~10,000 km) waves of the Northern Hemispheric general circulation, but also enhance the development of synoptic-scale (~1,000 km) waves and cyclones in their lee. Within these lee cyclones are found the fronts and jet streams whose vertical circulations provide the dynamical lifting which triggers the onset of severe organized convective precipitation systems. On the eastern (lee) face of the Rocky Mountains, the steepness of the orography is a contributing factor in the development of mesoscale weather. During winter and spring, lee cyclones and/or Great Plains anticyclones force moist air up the mountain slope producing heavy snow and rain in the foothills and at higher elevations, while sometimes leaving minimal precipitation on the plains just tens of kilometers to the east. The combination of snow melt runoff in late spring and orographic warm rain over the remaining mountain snow pack can result in the flooding of mountain streams, especially in densely populated areas where the streams flow out onto the Great Plains. During late spring and summer, weak upper-tropospheric winds coupled with moist orographic lifting have led to growth of "super cell" convective storms which remain quasi-stationary between the Continental Divide and the Plains 3 km below, producing precipitation rates in excess of 50 mm h^{-1}. When such storms persist for several hours, the resulting flooding in canyons below has been destructive to life and property. The steepness of the lee forces mesoscale mountain lee waves under conditions of strong westerly flow over the Divide. Lee wave action can extend vertically from the earth's surface up to the lower stratosphere. Surface wind gusts from such waves have exceeded 60 m s^{-1} in foothills communities and their upper-tropospheric and lower stratospheric turbulence plays havoc with air transportation in transcontinental flight.

The northern portion of the region is the gateway for the frigid arctic air masses that cross the United States-Canadian border during winter and early spring. The blizzards of the central plains and midwest owe their extremely cold temperatures to these Canadian arctic air masses. The leading edge of the arctic air is marked by the arctic front. In addition to the mesoscale precipitation at the arctic front, the lower surface of the frontal inversion often caps a stratocumulus cloud layer and/or ground fog which can blanket substantial portions of the region. Such extensive ground and near-ground cloud cover has frequently crippled air and surface transportation. When cyclones form and travel along the arctic front, condensation within the warm southerly flow above the front falls as rain into the subfreezing arctic air. The resulting freezing rain of midwestern ice storms disrupts electric power transmission and telephone communication, devastates trees and foliage, and snarls road, rail, and air transportation.

The southern portion of the region is characterized by strong moisture contrasts. The extremely dry flow off the desert plateau of Mexico and New Mexico is a stark contrast to the moist maritime air which flows into the region from the Gulf of Mexico. The convergence of these dry and moist currents forms the Texas-Oklahoma dryline fronts, along which some of the most convective weather is spawned. Blinding duststorms are frequent mesoscale events over New Mexico, Texas, and Oklahoma in the dry southwesterly flow behind drylines and fronts prior to or during convective storm outbreaks. Convective systems play host to hail storms and tornadoes. The northward transport of Gulf moisture feeds the synoptic and convective precipitation systems throughout the Central Region. On rare occasions, the remnants of Pacific tropical cyclones cross the mountains of Mexico and enter the southwestern United States as poorly organized circulations with high moisture content. These systems provide the moisture source for convective outbreaks over the desert southwest, west Texas, and the Colorado Rockies, and have been responsible for summer and early fall flash flooding over the southwestern portion of the region.

The eastern edge of the region is bounded by the 90th meridian. This is neither a meteorological nor an orographic boundary, as mesoscale weather systems which form within the Central Region often propagate eastward influencing weather to the Atlantic coast and beyond.

The following treatment of the structure and theory of mesoscale weather systems of the central U.S. begins with a presentation of an approximated set of equations for the mesoscale. These equations are based upon the principles of mechanics and thermodynamics and are used to define the physical processes which give rise to the development and maintenance of mesoscale structures in wind velocity, temperature, moisture and chemical trace constituents. The equations contain terms which define the geostrophic, ageostrophic and diabatic processes which force the mesoscale plus the eddy flux terms of the sub-mesoscale processes. The inclusion of the eddy terms facilitates the discussion of the interdependency between the large and small scale processes. We will utilize these equations in conjunction with observations from observed and simulated mesoscale phenomena to illustrate the interactions by which the synoptic-scale deformations initiate the scale contraction of wind velocity, temperature and moisture gradients down to the mesoscale, which in turn creates the environment within which the smaller-scale processes, such as turbulent boundary layers, convective clouds, frontal precipitation and clear air turbulence, etc. evolve and ultimately feed back and modify the evolution of the meso- and synoptic-scale weather systems.

After developing a theoretical basis for the genesis of mesoscale gradients, we present examples of selected meso-scale phenomena which occur within (but are not necessarily exclusive to) the central United States. The weather systems discussed are upper- and low-level jet streams, fronts and associated turbulence, dryline fronts, arctic air mass outbreaks, orographic-frontal interactions, boundary-layer inversions and jets, frontal convection (squall lines), and mesoscale convective complexes (MCCs).

The discussion of specific mesoscale structures is followed by a case study of a Texas-Oklahoma squall line, illustrating the interactions of synoptic and mesoscale processes which culminate in the explosive outbreak of severe meso-convective and cumulus cloud-scale weather and boundary-layer turbulence.

2. Scale definitions and governing equations

In the preceding section, we have used the term "mesoscale" to describe a variety of atmospheric phenomena. Fujita (1963) and Orlanski (1975) refined the definition of mesoscale processes by partitioning them according to their characteristic space and time scales. Following Orlanski (1975), the mesoscale is subdivided into the meso-α (10^2-10^3 km, 1-5 days), fronts and hurricanes; meso-β (10-10^2 km, 3 h-1 day), nocturnal low-level jets, squall lines, internal waves, cloud clusters, mountain waves and lake disturbances; and meso-γ (1-10 km, 1 hr.), thunderstorms, inertia-gravity waves, clear air turbulence (CAT) and urban effects. The mesoscale is bounded by the large-scale motions, termed mesoscale, which include the baroclinic waves of the macro-β (2×10^3-10^4 km, 1 week) and by the microscale processes which range from the tornadoes of the micro-α (0.2-2 km, 10 min-1 hr) down to the turbulent dissipation by the micro-γ (20 m, 1 min). In selecting a set of governing equations for diagnosis, simulation, or prediction of a specific mesoscale phenomenon, it is important to consider the characteristic space and time scales as well as the dominant physical processes. For example, the formation of meso-α fronts and their associated jets is well described by the two-dimensional (y,p), inviscid and adiabatic geostrophic momentum equations (see Eliassen, 1948, 1962; Hoskins and Bretherton, 1972) which assume hydrostatic balance and that the acceleration of the horizontal velocity is approximated by the accleration of its geostrophic component, neglecting acceleration of the ageostrophic motions. In contrast, the meso-convective cloud systems of the meso-β and meso-α evolve in response to diabatic and turbulent processes and the state transformations of water within individual cloud elements. These systems must be studied three-dimensionally using a non-hydrostatic momentum equation with eddy stress terms, a thermodynamic energy equation containing heat sources and sinks as first order processes and moisture equations which incorporate cloud drop nucleation processes and the phase transformations between vapor, liquid and ice (see, i.e., Klemp and Wilhelmson, 1981).

For the present discussion, we shall apply the two-dimensional form of the geostrophic momentum equations to the evolution of the meso-α scale motions. The meso-β and -γ processes will be treated as small perturbations upon the meso-α which form in response to development of a "preferred" environment within meso-α systems, as is consistent with the current approach of short-range (12-48 hr) mesoscale numerical weather prediction which explicitly predicts the evolution of the meso-α scale, while implicitly including the meso-β and -γ scales through parameterizations of their processes.

The introduction of the geostrophic momentum equations by Eliassen (1962) provided the theoretical basis for diagnostic, analytical, and numerical studies of fronts and jet streams by Todson (1964), Hoskins and Bretherton (1972), and Shapiro (1981). The geostrophic momentum (GM) approximation (see Eliassen, 1948) is the foundation for these equations and assumes that the velocity acceleration $d\underset{\sim}{V}/dt$ is approximated by the acceleration of its geostrophic component $d\underset{\sim}{V}_g/dt$, neglecting the acceleration of the horizontal ageostrophic motions $d\underset{\sim}{V}_a/dt$, while retaining the horizontal and vertical ageostrophic advections of $\underset{\sim}{V}_g$

$$\frac{d\underset{\sim}{V}}{dt} \simeq \frac{d\underset{\sim}{V}_g}{dt} = \frac{\partial \underset{\sim}{V}_g}{\partial t} + (\underset{\sim}{V}_g + \underset{\sim}{V}_a)\cdot\nabla \underset{\sim}{V}_g + \omega \frac{\partial \underset{\sim}{V}_g}{\partial p} >> \frac{d\underset{\sim}{V}_a}{dt} \ . \qquad (1)$$

In the present discussion, we apply the GM approximation and assume hydrostatic, Boussinesq flow, neglecting latitudinal derivatives in the Coriolis parameter. As in earlier treatments by Sawyer (1956), Eliassen (1962), Williams (1967), Orlanski and Ross (1977), Gidel (1978), and Shapiro (1981), we further restrict this development to those systems embedded within small-amplitude wave regimes (i.e., near-straight fronts) possessing secondary circulations which are confined to the transverse (cross-front) plane. We shall include diabatic processes and the turbulent vertical fluxes of heat momentum and chemical trace constituents. Given these approximations, the GM equations are written

$$\frac{dU}{dt} = \frac{\partial U}{\partial t} + U\frac{\partial U}{\partial x} + (V + v_a)\frac{\partial U}{\partial y} + \omega\frac{\partial U}{\partial p} = fv_a - \frac{\partial \overline{U'\omega'}}{\partial p} \ , \qquad (2)$$

$$\frac{dV}{dt} = \frac{\partial V}{\partial t} + U\frac{\partial V}{\partial x} + (V + v_a)\frac{\partial V}{\partial y} + \omega\frac{\partial V}{\partial p} + \frac{\partial \overline{V'w'}}{\partial p} = -fu_a \approx 0 \ , \qquad (3)$$

$$\frac{d\theta}{dt} = \frac{\partial \theta}{\partial t} + U\frac{\partial \theta}{\partial x} + (V + v_a)\frac{\partial \theta}{\partial y} + \omega\frac{\partial \theta}{\partial p} + \frac{\partial \overline{\theta'\omega'}}{\partial p} \ , \qquad (4)$$

$$\frac{dq}{dt} = \frac{\partial q}{\partial t} + U\frac{\partial q}{\partial x} + (V + v_a)\frac{\partial q}{\partial y} + \omega\frac{\partial q}{\partial p} + \frac{\partial \overline{q'\omega'}}{\partial p} \ , \qquad (5)$$

$$U = -\frac{1}{f}\frac{\partial \Phi}{\partial y} \ , \quad V = \frac{1}{f}\frac{\partial \Phi}{\partial x} \ , \quad \frac{\partial U}{\partial x} + \frac{\partial V}{\partial y} \approx 0 \ , \qquad (6)$$

$$\frac{\partial U}{\partial p} = \frac{\partial m}{\partial p} = \gamma\frac{\partial \theta}{\partial y} \ , \quad \frac{\partial V}{\partial p} = -\gamma\frac{\partial \theta}{\partial x} \ , \qquad (7)$$

$$\frac{\partial v_a}{\partial y} + \frac{\partial \omega}{\partial p} = 0 \, , \tag{8}$$

$$v_a = - \frac{\partial \psi}{\partial p} \, , \quad \omega = \frac{\partial \psi}{\partial y} \, , \tag{9}$$

$$\gamma = \frac{R}{fp_o} \left(\frac{p_o}{p}\right)^{C_v/C_p} \, , \quad \frac{\partial \gamma}{\partial p} \simeq 0 \, , \tag{10}$$

$$m = U - fy \, , \tag{11}$$

where the respective equations are the equations for along- and cross-front momentum (2 and 3), thermodynamic energy (4), chemical trace constituent (5), geostrophic wind and its nondivergent characteristic for small $\partial f/\partial y$ (6), geostrophic thermal wind (7), mass continuity (8), secondary circulatory velocity components (9), Boussinesq flow (10), and geostrophic absolute momentum (11). See Table 1 for a list of symbols.

Equations describing the development of horizontal and vertical gradients of geostrophic momentum, potential temperature, and trace constituent are obtained through horizontal and vertical differentiation of Eqs. (2), (4), and (5), with the aid of (6) through (11), noting the definition of the transverse and horizontal Jacobian operators, $J_{yp}(\alpha,\beta)$ and $J_{xy}(\alpha,\beta)$, respectively.

$$J_{yp}(\alpha,\beta) = \frac{\partial \alpha}{\partial y}\frac{\partial \beta}{\partial p} - \frac{\partial \beta}{\partial y}\frac{\partial \alpha}{\partial p} \, , \tag{12}$$

$$J_{xy}(\alpha,\beta) = \frac{\partial \alpha}{\partial x}\frac{\partial \beta}{\partial y} - \frac{\partial \beta}{\partial x}\frac{\partial \alpha}{\partial y} \, . \tag{13}$$

Table 1 List of Symbols

α,β	generalized dependent variables
C_v	specific heat at constant volume
C_p	specific heat at constant pressure
C_D	surface drag coefficient
f	Coriolis parameter $[-2\Omega \sin\phi]$
f_o	mean Coriolis parameter
F_s	slope of a frontal discontinuity
g	gravity
Γ	dry adiabatic lapse rate
Γ_m	moist adiabatic lapse rate
i,j,k	unit vectors in the x,y,p directions
K_h	vertical diffusivity for heat
K_m	vertical diffusivity for momentum
K_t	three-dimensional trajectory curvature
m	along-front geostrophic absolute momentum
p	pressure
P	potential vorticity
Pr	Prandtl number
ψ	streamfunction of the secondary circulation
ϕ	latitude
Φ	geopotential [gz]
q	water vapor mixing ratio
q'	turbulent perturbation component of q
Q	total cross-front circulation forcing
Q_1	stretching deformation circulation forcing
Q_2	shearing deformation circulation forcing
Q_t	clear-air turbulence circulation forcing
Ri	Richardson number
s	distance along an isentrope
t	independent variable time
θ	potential temperature
θ'	turbulent perturbation potential temperature
θ_E	equivalent potential temperature
u	total along-front velocity component
U,u_a	geostrophic and ageostrophic components of u
U'	turbulent perturbation component of U
V	total horizontal velocity vector
V_g,V_a	geostrophic and ageostrophic vector components of V
v	total cross-front velocity component
V,v_a	geostrophic and ageostrophic components of v
w	z-coordinate vertical velocity
ω	p-coordinate vertical velocity
x,y	along-front and cross-front distance
z	geometric height

The frontal development equations are

$$\frac{d}{dt}\left(\frac{\partial m}{\partial y}\right) = -J_{yp}(m,\omega) - \frac{\partial^2 \overline{U'\omega'}}{\partial y \partial p} , \tag{14}$$

$$\frac{d}{dt}\left(\frac{\partial m}{\partial p}\right) = -J_{yp}(U,V) - J_{yp}(m,v_a) - \frac{\partial^2 \overline{U'\omega'}}{\partial p^2} , \tag{15}$$

$$\frac{d}{dt}\left(\gamma \frac{\partial \theta}{\partial y}\right) = J_{yp}(U,V) + \gamma J_{yp}(\theta,\omega) - \gamma \frac{\partial^2 \overline{\theta'\omega'}}{\partial y \partial p} + \gamma \frac{\partial}{\partial y}\left(\frac{d\theta}{dt}\right) , \tag{16}$$

$$\frac{d}{dt}\left(\frac{\partial \theta}{\partial p}\right) = -J_{yp}(\theta,v_a) - \frac{\partial^2 \overline{\theta'\omega'}}{\partial p^2} + \frac{\partial}{\partial p}\left(\frac{d\theta}{dt}\right) , \tag{17}$$

$$\frac{d}{dt}\left(\frac{\partial q}{\partial y}\right) = -J_{xy}(q,U) - J_{yp}(q,\omega) - \frac{\partial^2 \overline{q'\omega'}}{\partial y \partial p} , \tag{18}$$

$$\frac{d}{dt}\left(\frac{\partial q}{\partial p}\right) = -J_{xy}(q,\theta) - J_{yp}(q,v_a) - \frac{\partial^2 \overline{q'\omega'}}{\partial p^2} , \tag{19}$$

where the respective equations give the changes following an air parcel trajectory of the vertical component of vorticity, $\partial m/\partial y$ (14); horizontal component of vorticity or vertical shear of m, $\partial m/\partial p$ (15); γ times horizontal cross-front thermal gradient, $\partial \theta/\partial y$ (16); thermal stability, $\partial \theta/\partial p$ (17); and horizontal and vertical gradients in trace constituent, $\partial q/\partial y$ (18); and $\partial q/\partial p$ (19). Following Shapiro (1981), the right-hand side forcing for these equations is partitioned into terms involving geostrophic, ageostrophic, turbulent, and diabatic processes.

The transverse secondary circulation equation is formed (after Sawyer, 1956; Eliassen, 1962) by eliminating the temporal derivatives of Eqs. (15) and (16) through the thermal wind relationship (17).

$$-\gamma \frac{\partial\theta}{\partial p}\frac{\partial^2\psi}{\partial y^2} + 2\frac{\partial m}{\partial p}\frac{\partial^2\psi}{\partial y\partial p} - \frac{\partial m}{\partial y}\frac{\partial^2\psi}{\partial p^2} = -2J_{yp}(U,V) - \frac{\partial^2\overline{U'\omega'}}{\partial p^2}$$

$$+ \gamma\frac{\partial^2\overline{\theta'\omega'}}{\partial y\partial p} + \gamma\frac{\partial}{\partial y}\left(\frac{d\theta}{dt}\right) , \qquad (20)$$

where the four forcing terms on the right-hand sides of Eq. (20) represent the effects of geostrophic deformations on the meso-α and macro-β scale, turbulent fluxes of momentum, $\overline{U'\omega'}$ and heat $\overline{\theta'\omega'}$ of the meso-β and γ-scales and diabatic heat sources and sinks ranging from the macro-β to the meso-γ scale, respectively. It should be noted that (20) explicitly assumes thermal wind equilibrium following a three-dimensional parcel trajectory, and therefore the response to the geostrophic, diabatic, and turbulent forcing is assumed to be a nearly instantaneous adjustment through the forced secondary (ageostrophic) circulations. The ellipticity condition required for the numerical solution of (20) is a physical condition, in that the potential vorticity P must be greater than or equal to zero.

$$P = -\left.\frac{\partial m}{\partial y}\right|_{\theta} \frac{\partial\theta}{\partial p} = -J_{yp}\,(m,\theta) \geq 0 \ . \qquad (21)$$

When the actions of turbulent or diabatic processes cause the potential vorticity to become less than zero, then the motions become unstable to symmetric overturnings and the GM-circulation equation is hyperbolic in form. Symmetric instability (see Eliassen and Kleinschmidt, 1957; Hoskins, 1974; Emanuel, 1979) gives rise to internal transverse circulations on horizontal scales ranging from 10 to 100 km which act to restore the potential vorticity to its stable, greater-than-zero value. The character of the symmetric instability circulations is determined by solution of the hyperbolic form of the GM-circulation equation. Bennetts and Hoskins (1979) and Emanuel (1979) have proposed that frontal and meso-convective rain bands may result from vertical circulations arising from symmetric instability.

It is of interest to note the difference between the geostrophic momentum, semi-geostrophic, and quasi-geostrophic (QG) equations, as all three forms have been applied to the study of synoptic and mesoscale motions. The semi-geostrophic equations (see Hoskins, 1975) are the GM-equations transformed into geostrophic coordinates. The form of the semi-geostrophic equations is identical to the QG equations in conventional physical coordinates. The quasi-geostrophic equations assume that the acceleration of the horizontal velocity is given by its geostrophic component, neglects the horizontal and vertical ageostrophic advections of momentum and the horizontal ageostrophic advection of potential temperature. Thermal stability $\partial\theta/\partial p$ is taken as a function of pressure only, and the Coriolis parameter is set constant over the domain of interest. The two-dimensional inviscid, adiabatic QG equations, equivalent to the GM equations (2, 4, and 20), are

$$\frac{dU}{dt} = \frac{\partial U}{\partial t} + U\frac{\partial U}{\partial x} + V\frac{\partial U}{\partial y} = f_o v_a \ , \tag{22}$$

$$\frac{d\theta}{dt} = \frac{\partial \theta}{\partial t} + U\frac{\partial \theta}{\partial x} + V\frac{\partial \theta}{\partial y} + \omega\frac{\partial \theta}{\partial p}(p) = 0 \ , \tag{23}$$

$$-\gamma\frac{\partial \theta}{\partial p}(p)\frac{\partial^2 \psi}{\partial y^2} + f_o\frac{\partial^2 \psi}{\partial p^2} = -2J_{yp}(U,V) \ . \tag{24}$$

A comparison between the GM and QG secondary circulation equations (Eqs. 20 and 24) reveals that the geostrophic forcing $-2J_{yp}(U,V)$ is the same for both levels of approximation. What differs are the coefficients of the ageostrophic stream function differentials and the absence of the mixed derivative term for the QG equation. Differentiation of (24) with respect to y gives (after Hoskins et al., 1978) the two-dimensional form of the QG omega-equation for vertical motion,

$$-\gamma\frac{\partial \theta}{\partial p}(p)\frac{\partial^2 \omega}{\partial y^2} + f_o\frac{\partial^2 \omega}{\partial p^2} = -2\frac{\partial}{\partial y}\left[J_{yp}(U,V)\right] \ , \tag{25}$$

in which after manipulation, the right-hand side becomes the more familiar vertical derivative of the geostrophic vorticity advection plus the Laplacian of the geostrophic thermal advection. From (24) and (25), we note that quasi-geostrophic circulations and vertical motions are only related to the strength and spatial distribution of the geostrophic forcing and are not affected by spatial variations in thermal stability, baroclinicity, or absolute vorticity.

If we consider the secondary circulations which arise from the GM circulation equation (20), we note that it is not just the geostrophic forcing that determines the character of the circulation, but that the variable coefficients of the equations' left-hand side also influence the solution. Eliassen (1962) demonstrated that for a given point source of geostrophic forcing, the GM circulation cells are in the shape of ellipses whose major and minor axes are determined by the relative magnitudes of the thermal stability $\partial\theta/\partial p$ and vorticity $\partial m/\partial y$, and whose vertical slope is proportional to the baroclinicity $\partial\theta/\partial y$ or $\partial m/\partial p$. If $-\partial\theta/\partial p$ is large and $-\partial m/\partial y$ is small, the circulation ellipses lie on their sides and the ageostrophic displacements are predominantly horizontal. If, however, $-\partial\theta/\partial p$ is small (weak thermal stability) and $-\partial m/\partial y$ is large (large cyclonic relative vorticity), the circulation ellipses are upright with large vertical motions and relatively small horizontal ageostrophic displacements. A comparison between numerical simulations of fronts using both QG and GM models by Williams (1967) quantitatively demonstrated the influence of spatial variations in thermal stability, baroclinicity, and vorticity upon frontal secondary circulations. Since changes in the circulation coefficients are themselves tied to the secondary circulations [note the ageostrophic Jacobian terms in (14) through (16)], it is clear that the evolution of the meso-α is governed by an interdependency between geostrophic and ageostrophic processes which is further complicated by feedbacks from the smaller scale (meso-β through micro-γ) systems.

The assumption within GM theory that the ageostrophic response to geostrophic, diabatic, and turbulent forcing is nearly instantaneous with thermal wind equilibrium being maintained along isentropic trajectories becomes questionable when the time scale over which strong forcings are initiated is short ($\tau \sim 3$ h) when compared to the ~18 h period of an inertial oscillation. For example, consider meso-convective systems which develop into squall lines or mesoscale convective complexes (MCCs) within a time interval of 1 h (see example) and which contain cloud elements extending to above 11 km with precipitation rates of > 25 mm h^{-1}. The rapid "delta function" onset of vertical momentum flux and diabatic heating from such systems initially destroys thermal wind equilibrium and induces internal and inertia-gravity waves which attempt to disperse the imbalance created by such shocks to a previously balanced system. The imbalance takes the form of an ageostrophic vertical wind shear of the along-jet velocity component, $\partial U_a/\partial p$. The result is sub- or supergeostrophic vertical wind shear which is not balanced through the centripetal acceleration of curved flow (i.e., gradient thermal wind balance). The excited waves are capable of initiating convection in regions adjacent to the original convection (see Uccellini, 1975). Because of the lack of temporally continuous and high spatial resolution (~10 km) observations, there exists little if any direct documentation of the space and time scales over which the adjustments to forced imbalances take place, or the amplitude to which these imbalances grow before internal and inertia-gravity wave actions and/or ageostrophic circulations begin to develop. Our current knowledge of unbalanced motions is restricted to the study of such phenomena within primitive equation simulations and predictions which incorporate sub-grid-scale parameterizations. It remains for future research to advance our understanding of the responses to the rapid onset of strong convection and planetary boundary layer processes and to determine the effect of internal and inertia-gravity waves upon frontal and convective evolutions.

A further limitation in the application of GM theory occurs when jet-front systems form within large-amplitude, sharply curved baroclinic waves, where the acceleration of the ageostrophic velocity is of comparable magnitude to its geostrophic counterpart. These ageostrophic accelerations are primarily the result of the centripetal acceleration of curved flow which occurs when air parcels meander through the macro-β waves. Shapiro and Kennedy (1981) presented direct measurements illustrating the breakdown of the GM approximation for a jet-front embedded within a sharp upper-tropospheric wave. Under such conditions, the simulation and diagnosis of evolutions must be treated using nonlinear "balanced" theory (see Charney, 1955, 1962), intermediate approximated equations (see McWilliams and Gent, 1981) or with the hydrostatic primitive equations.

In formulating the conceptual models describing the synoptic evolutions which produce conditions favorable for the outbreak of severe convective systems, research and forecast meteorologists have coupled empirical techniques, quasi-geostrophic diagnostics, convective instability and boundary-layer theory. Consider the following examples. Empirical studies have shown that the superposition of a dry upper-level westerly jet stream current over a moist southerly low-level jet is conducive to convective development (see Beebe and Bates, 1955; Newton, 1963). Quasi-geostrophic theory is qualitatively applied by operational field forecasters to identify regions of synoptic-scale ascent by noting areas of upper-tropospheric cyclonic vorticity advection and/or local maxima of middle-tropospheric warm air advection. The thermal destabilization of the middle-troposphere by differential thermal advection between upper- and lower-troposphere layers (cold air advection aloft superimposed upon lower moist warm air advection) reduces the thermal stratification of the middle troposphere and develops the conditional instability ($\Gamma > \Gamma_m$) and convective instability ($\partial\theta_e/\partial p > 0$), which is released through moist convection. Mid-tropospheric vertical wind shear (baroclinicity) has been cited by Newton (1950) as an important factor in the formation and maintenance of meso-convective systems. In our discussion of specific mesoscale systems which follows, we shall relate the above and other concepts to specific processes within the GM secondary circulation and frontal development equations.

3. Upper-Level Jet Streams and Fronts

Upper-level jet streams and frontal layers have been cited as a triggering mechanism for the formation of extratropical cyclones and the onset of meso-convective development (Newton, 1963; Palmén and Newton, 1969; Uccellini and Johnson, 1979). Jet-front systems possess physical characteristics of both the macro-β and meso-α scales, as their length is macro-β or larger and their transverse structure contains meso-α velocity and thermal gradients. Meso-α velocity and temperature gradients are found where sloping frontal layers intersect the quasi-horizontal isobaric surfaces within the middle and upper troposphere (Palmén, 1948). In the layer of maximum wind near the tropopause, ageostrophic contractions create meso-α cyclonic wind shear (Shapiro, 1976) and the vertical deformations of the tropopause and stratospheric potential vorticity (Reed, 1955; Hoskins and Bretherton, 1972). Besides their association with extratropical weather events, the vertical circulations during upper-jet front development have been shown by Danielsen (1968) and Shapiro (1980) to promote the short period (~1 day) exchange of air and chemical trace constituents between the stratosphere and troposphere. Vertical wind-shear instability within jet-stream baroclinic layers creates vertical mixing, referred to as clear-air turbulence (CAT), which feeds back into the jet-front evolutions (Shapiro, 1976, 1981; Kung, 1977) and often produces hazardous flying conditions for commercial and military aircraft (Endlich, 1963; Kennedy and Shapiro, 1980).

The central United States is traversed by jet streams originating from both polar and subtropical latitudes. The polar jets are found within the meanders of the middle-latitude Rossby wave regime. Subtropical jet streams migrate across the southern portion of the Central Region within the small-amplitude Rossby waves of the Northern Hemispheric subtropical current (Krishnamurti, 1961). Individual jet "streak" impulses (wind speed maxima of finite length, ~3-10 × 10^3 km; Newton, 1959) form through the phase interactions between waves of the arctic and polar latitudes and polar and subtropical latitudes. For example, a meridional phase alignment of an arctic trough axis with a polar ridge, produces the classical Bergeron (1928) geostrophic confluence (difluence) to the west (east) of the phase alignment. The confluent deformation forces the formation of polar jet streaks and their associated upper fronts and mass circulations (Namias and Clapp, 1949; Murray and Daniels, 1951). Once formed, jet impulses propagate through the slower-moving synoptic waves (see Fig. 7) and, on occasion, trigger cyclogenesis and organized convective systems. Some of the most intense cyclonic and convective weather occurs when the ascending motions associated with upper jet-front mass circulations are in phase with the ascending motions found in advance of sharp upper-tropospheric troughs.

An example of an upper jet front over the central United States from Shapiro et al. (1982) is shown in Figs. 1 and 2. The 250 mb wind speed analysis at 0000 GMT 5 April 1981 (Fig. 1) contains a >75 m s^{-1} jet wind maximum. The jet core is located downstream from the confluence of polar and subtropical wind currents. On this day, the NCAR Sabreliner aircraft executed horizontal traverses along the line AA' of Fig. 1 between 540 and 180 mb, measuring wind velocity, potential temperature, and ozone

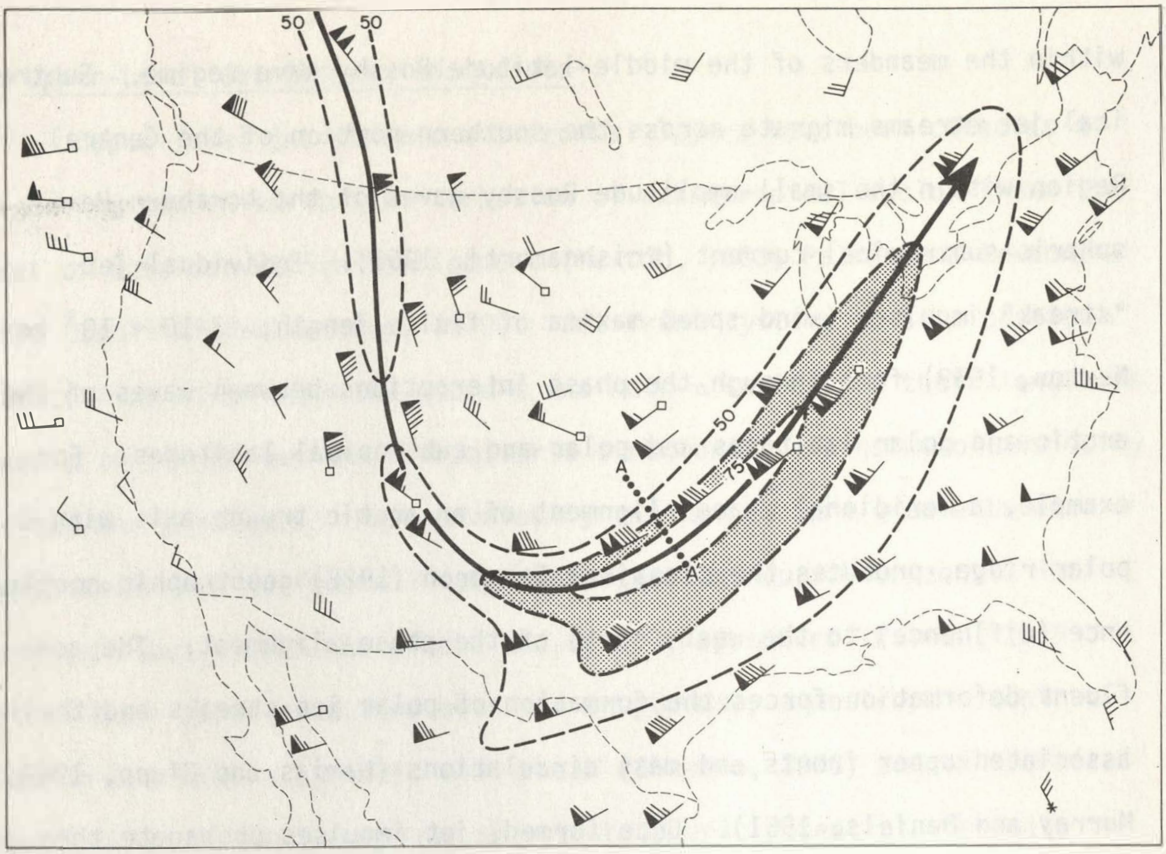

Fig. 1. 250 mb wind speed (dashed lines, m s^{-1}) at 0000 GMT 5 April 1981. Rawinsonde wind velocities (flag, 25 m s^{-1}; barb, 5 m s^{-1}; half barb, 2.5 m s^{-1}), commercial airline wind reports (open box vectors), satellite cloud motion winds (asterisked vectors), jet stream axes (heavy solid arrow) and 62.5 to 75.0 m s^{-1} wind speed interval (stippled area). AA' is the projection line for Sabreliner aircraft data of Fig. 2.

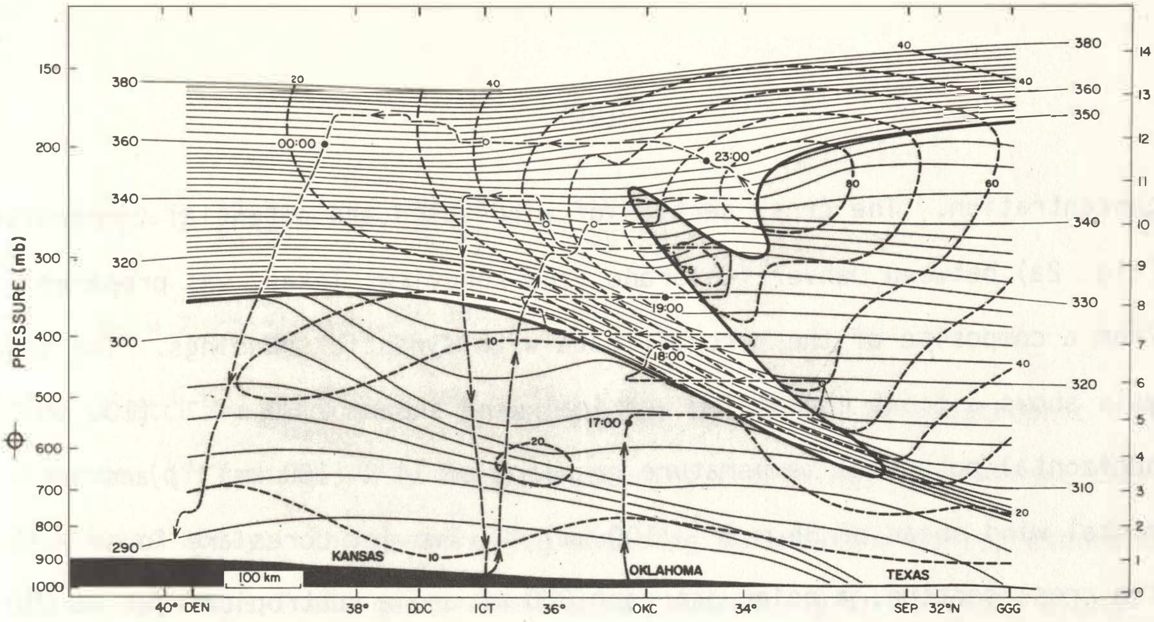

Fig. 2(a). Cross-section analysis of wind speed (m s^{-1}, heavy dashed lines) and potential temperature (K, thin solid lines) along line AA' for 1900 GMT 5 April 1981. Sabreliner flight track (thin dashed lines) with hourly (solid circles) and half-hourly (open circles) time hacks. Tropopause (10^{-5} K mb^{-1} s^{-1} isopleth of potential vorticity, heavy solid line). Rawinsonde soundings are from Denver, Colorado (DEN), Dodge City, Kansas (DDC), Oklahoma City, Oklahoma (OKC), Stephenville, Texas (SEP) and Longview, Texas (GGG).

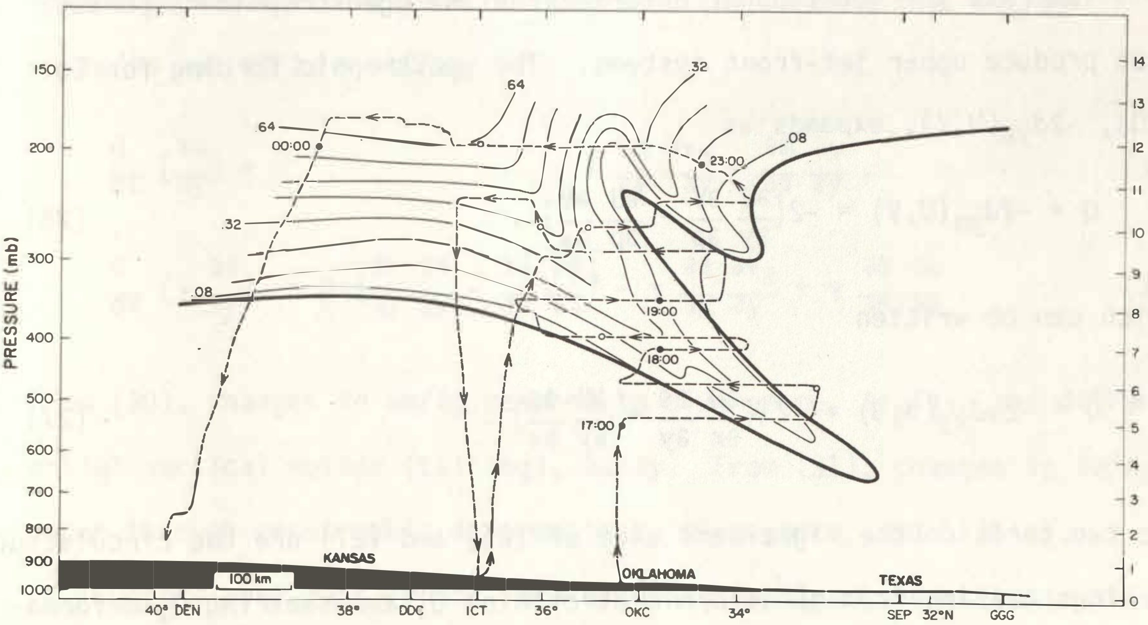

Fig. 2(b). Cross section of ozone (parts per million by volume) for Fig. 2(a).

concentration. The cross section of wind speed and potential temperature (Fig. 2a) between Denver, Colorado, and Longview, Texas, was prepared from a composite of the aircraft data with synoptic soundings. The analysis shows a front containing vertical wind shear of 30 m s^{-1} $(100\ \text{mb})^{-1}$, horizontal potential temperature gradient of 14 K $(100\ \text{km})^{-1}$, and horizontal wind shear of 35 m s^{-1} $(100\ \text{km})^{-1}$. Two jet cores are found within the cross section, a polar jet near 300 mb and a subtropical jet at 230 mb. The potential vorticity tropopause is folded downward on the cyclonic shear side to the two jets. The ozone analysis (Fig. 2b) shows the downward intrusion of ozone-rich stratospheric air which results from the vertical and horizontal displacements of the tropopause by the jet-front secondary circulations.

After Sawyer (1956) and Eliassen (1962), we utilized the inviscid, adiabatic form of the geostrophic momentum circulation equation (Eq. 20) to illustrate the geostrophic deformations and ageostrophic responses that produce upper jet-front systems. The geostrophic forcing for Eq. (20), $-2J_{yp}(U,V)$, expands as

$$Q = -2J_{yp}(U,V) = -2\left(\frac{\partial U}{\partial y}\frac{\partial V}{\partial p} - \frac{\partial U}{\partial p}\frac{\partial V}{\partial y}\right) , \tag{26}$$

which can be written

$$Q = -2\gamma J_{xy}(U,\theta) = -2\gamma\left(\frac{\partial U}{\partial x}\frac{\partial \theta}{\partial y} - \frac{\partial U}{\partial y}\frac{\partial \theta}{\partial x}\right) . \tag{27}$$

The two terms on the right-hand side of (26) and (27) are the circulation forcings arising from geostrophic stretching Q_1 and shearing Q_2 deformations

$$Q_1 = 2\,\frac{\partial U}{\partial p}\frac{\partial V}{\partial y} = -2\gamma\,\frac{\partial U}{\partial x}\frac{\partial \theta}{\partial y} = 2\gamma\,\frac{\partial V}{\partial y}\frac{\partial \theta}{\partial y}\,, \tag{28}$$

$$Q_2 = 2\,\frac{\partial U}{\partial y}\frac{\partial V}{\partial p} = 2\gamma\,\frac{\partial U}{\partial y}\frac{\partial \theta}{\partial x}\;. \tag{29}$$

The stretching deformation Q_1 represents the effect of geostrophic confluence (difluence) $\partial V/\partial y$ in strengthening (relaxing) cross-front thermal gradients $\partial\theta/\partial y$. The geostrophic shearing deformation Q_2 represents the effect of cross-front geostrophic wind shear $\partial U/\partial y$ in rotating along-front thermal gradients $\partial\theta/\partial x$ into (out of) the cross-front direction. The secondary circulations occur in response to the geostrophic deformations of the cross-front thermal gradient $\partial\theta/\partial y$. Figure 3 illustrates the geostrophic deformations which force secondary (ageostrophic) circulations.

The processes which force the development of horizontal gradients of wind and temperature are obtained by expanding the Jacobians of the adiabatic and inviscid form of (14) and (16), noting that $\partial v_a/\partial y = -\partial\omega/\partial p$ and $\partial U/\partial x = -\partial V/\partial y$

$$\frac{d}{dt}\left(\frac{\partial m}{\partial y}\right) = -\,\frac{\partial m}{\partial y}\frac{\partial v_a}{\partial y} - \frac{\partial m}{\partial p}\frac{\partial \omega}{\partial y}\,, \tag{30}$$

$$\frac{d}{dt}\left(\gamma\,\frac{\partial \theta}{\partial y}\right) = 2\gamma\left(\frac{\partial V}{\partial y}\frac{\partial \theta}{\partial y} - \frac{\partial U}{\partial y}\frac{\partial \theta}{\partial x}\right) - \gamma\,\frac{\partial \theta}{\partial y}\frac{\partial v_a}{\partial y} + \gamma\,\frac{\partial \theta}{\partial p}\frac{\partial \omega}{\partial y}\;. \tag{31}$$

From (30), changes in $\partial m/\partial y$ respond to divergence, $\partial v_a/\partial y$, and differential vertical motion (tilting), $\partial\omega/\partial y$. From (31), changes in $\partial\theta/\partial y$ occur through geostrophic deformations, divergence, and tilting.

Upper-level jets, which form within a confluent geostrophic deformation (see Namias and Clapp, 1949; Hoskins and Bretherton, 1972; Gidel and

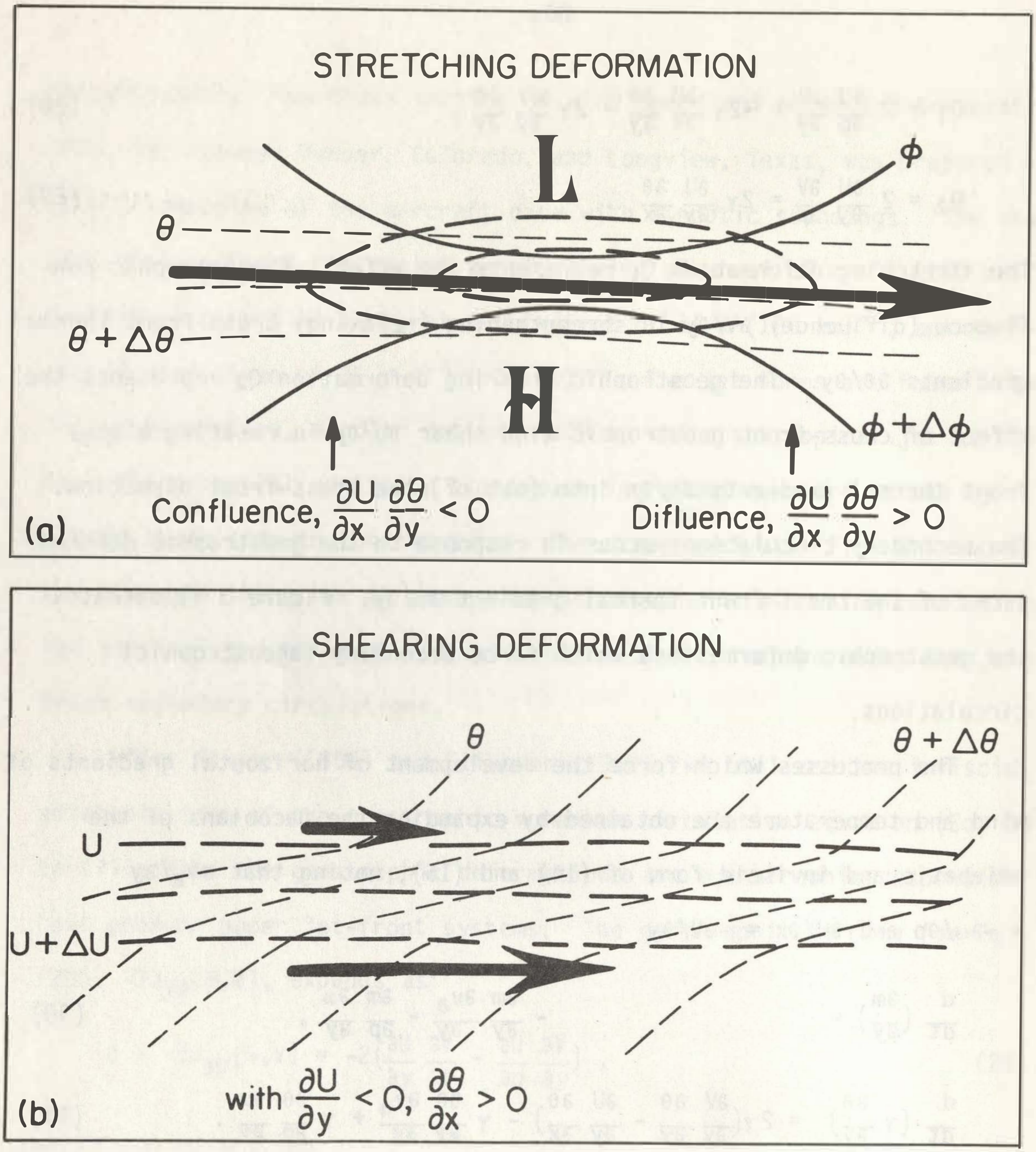

Fig. 3. (a) Stretching deformation for a mid-tropospheric jet-front. Geopotential height contours, heavy solid lines; along-front geostrophic wind speed, heavy dashed lines; potential temperature, thin dashed lines; jet axis, long straight arrow. (b) Shearing deformation within a mid-tropospheric cyclonic wind-shear front with a positive along-front thermal gradient. Isolines, same as (a), heavy solid arrows show cyclonic shear across the front.

Shapiro, 1979) are characterized by fronts near the tropopause which develop horizontal gradients in m through convergence in v_a. Increases in $\partial\theta/\partial y$ occur through geostrophic confluence plus ageostrophic convergence. The secondary circulations in the middle-tropospheric layer beneath these fronts are thermally direct, and the tilting effect acts to destroy gradients in m and θ in the presence of the geostrophic confluence. Figure 4 illustrates an analytical simulation of frontal formation near the tropopause and associated tropopause folding as forced by a confluent geostrophic deformation (after Hoskins and Bretherton, 1972). In contrast, mid-tropospheric frontal investigations by Reed and Sanders (1953), Newton (1954), Reed (1955), Danielsen (1968), Bosart (1970), and Shapiro (1970) revealed that the dominant frontal forcing mechanism was the tilting effect of a cross-front gradient in vertical motion where the maximum subsidence is at the warm side of the front ($\partial\omega/\partial y < 0$). This interpretation differs dramatically from that of the confluence theory which indicated ascending motions to the warm side of the middle-troposphere baroclinic layers ($\partial\omega/\partial y > 0$) during jet-front development. A reconciliation of the two interpretations by Shapiro (1981) illustrated that the combination of a confluent stretching deformation plus the cyclonic shearing deformation of a positive along-front thermal gradient ($\partial\theta/\partial x > 0$) forces strong sinking motions at the warm side of developing frontal layers. The resulting frontal formation was found to be primarily the result of tilting actions upon the m and θ fields. Thus, secondary circulations about upper jet-front systems may deviate from the classical thermally direct and indirect confluent entrance and difluent

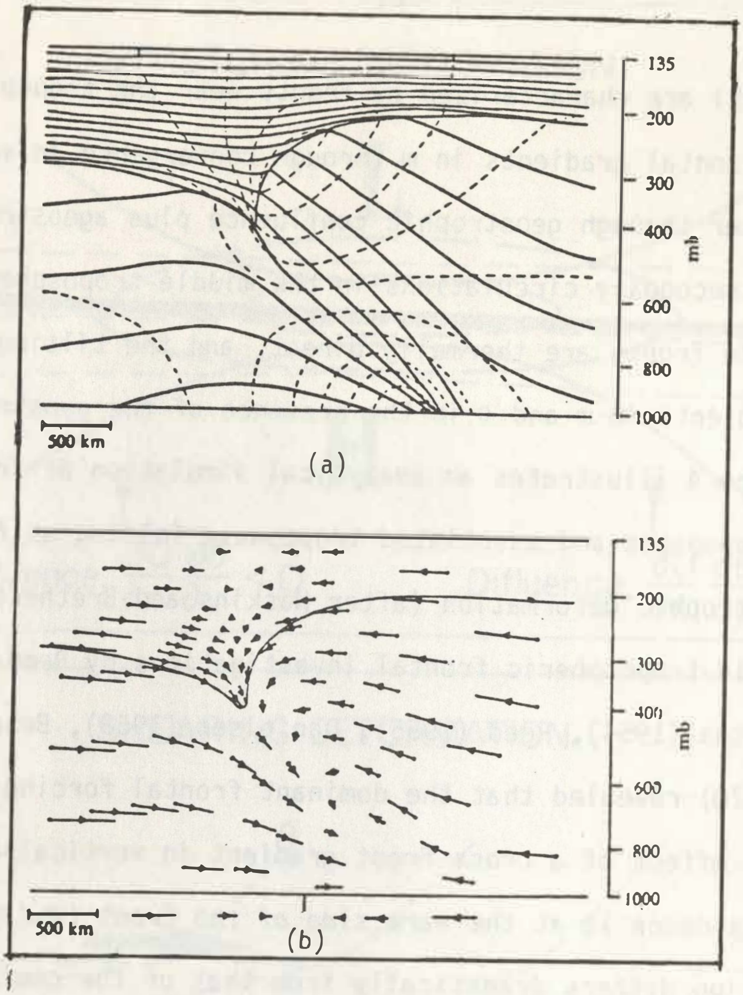

Fig. 4. Analytical simulation of tropopause folding and frontogenesis at the tropopause and at the ground. (a) Wind speed every 10.5 m s^{-1}, dashed lines; potential temperature every 7.8 K, thin solid lines; potential vorticity tropopause, heavy solid lines. (b) Cross-front motions (geostrophic plus ageostrophic) for (a). Basic confluent deformation is shown below the lower surface (after Hoskins and Bretherton, 1972).

exit region circulations, respectively, when alongfront thermal gradients $\partial\theta/\partial x$ are subjected to cross-front shearing deformations $\partial U/\partial y$. Such along-front thermal gradients are characteristic of jet-front systems embedded within sharp upper-tropospheric waves. Figure 5 shows the Shapiro (1975) numerical simulation of an upper front of the type described by Reed and Sanders (1953) and others, in which the front forms in response to tilting processes forced by a combination of geostrophic confluence and shearing deformations (with $\partial\theta/\partial x > 0$) within a baroclinic wave. Note the maximum sinking motion at the warm side of the developing frontal layer and the deep intrusion of stratospheric potential vorticity into the front.

Our understanding of jet-front systems has progressed to the point that the basic processes governing their evolution have been observed and diagnosed, simulated, and predicted with the laws of motion and thermodynamics. Yet a gap exists in identifying the spatial and temporal interplay between stretching deformations, shearing deformations, and baroclinic wave structure, which may all contribute to the development of specific atmospheric and simulated jet-front systems. The treatments by Namias and Clapp (1949), Sawyer (1956), Eliassen (1962), Hoskins and Bretherton (1972), Williams (1974), Orlanski and Ross (1977), and Gidel and Shapiro (1979) have described fronts and jet streams which are forced by either pure stretching or shearing deformations. The stretching deformation experiments set $\partial U/\partial x$ as constant in space and time and the shearing deformation fronts do the same for $\partial\theta/\partial x$. The atmospheric frontal studies by Reed and Sanders (1953), Newton (1954), Reed (1955),

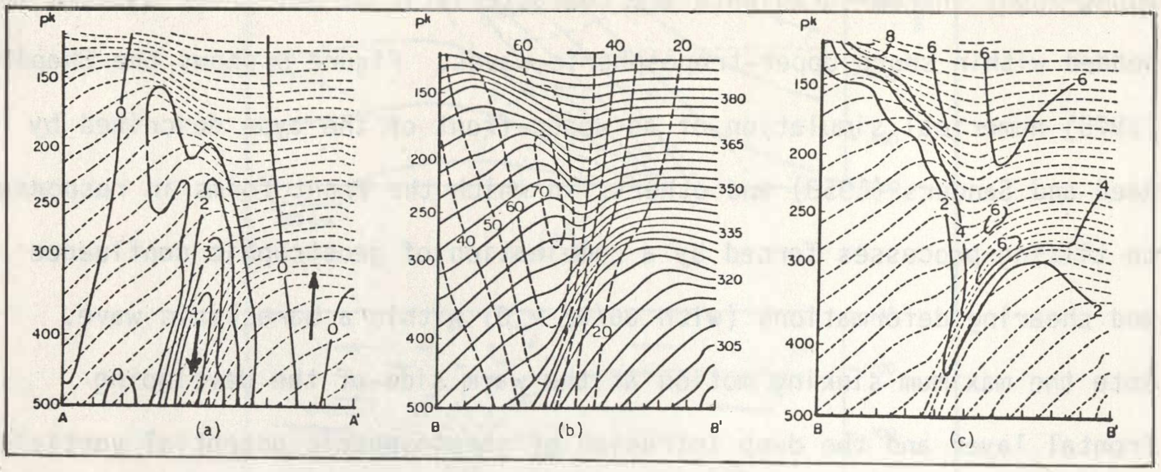

Fig. 5. Selected cross-sections from a three-dimensional numerical simulation of mid-tropospheric frontal formation and tropopause folding. (a) Cross-section of vertical motion (10^{-3} mb s^{-1}) taken through the frontogenetical entrance region of the model front. Potential temperature, dashed lines, same as (b). (b) Cross-section of wind speed (m s^{-1}), dashed lines; potential temperature (K), solid lines taken through the most intense portion of the front downstream from the (a) entrance. (c) Potential vorticity (10^{-5} s^{-1} K mb^{-1}) solid lines for (b) (after Shapiro, 1975). Distance AA' is 1000 km.

Staley (1960), Shapiro (1970), Bosart (1970), and Shapiro (1981) depict most jet-front systems at specific stages of their development. The diagnosis of frontal forcing processes at one instant does not necessarily imply that these same processes act throughout the full development of each frontal system. For example, in the study by Bosart (1970), three-hour synoptic soundings were available and results showed that the first six hours of the frontal development were dominated by confluent deformations and a weak thermally direct circulation, whereas during the second 6 h interval the tilting effect of a thermally indirect circulation was responsible for the final scale contraction of the frontal gradients.

There are numerous possible combinations of geostrophic stretching and shearing deformations which have yet to be examined as forcings for jet-front circulations and their analytical and numerical simulations. By varying the angle between the isotherms and the axis of dilation of the jet streak confluent deformation, one can develop scale contractions of velocity and thermal gradients by a variety of geostrophic and ageostrophic forcings within the Eqs. (14)-(17), frontal development equations. Figure 6 illustrates some combinations of stretching and shearing deformation patterns that determine the position of total geostrophic forcing and vertical motions relative to jet-front systems. In this figure, the regions of maximum forcing are defined by the density of (U,θ) isopleth intersections. The sign of the total forcing is easily inferred by noting the change of U along an isentrope (θ = constant with cold air to the left) since

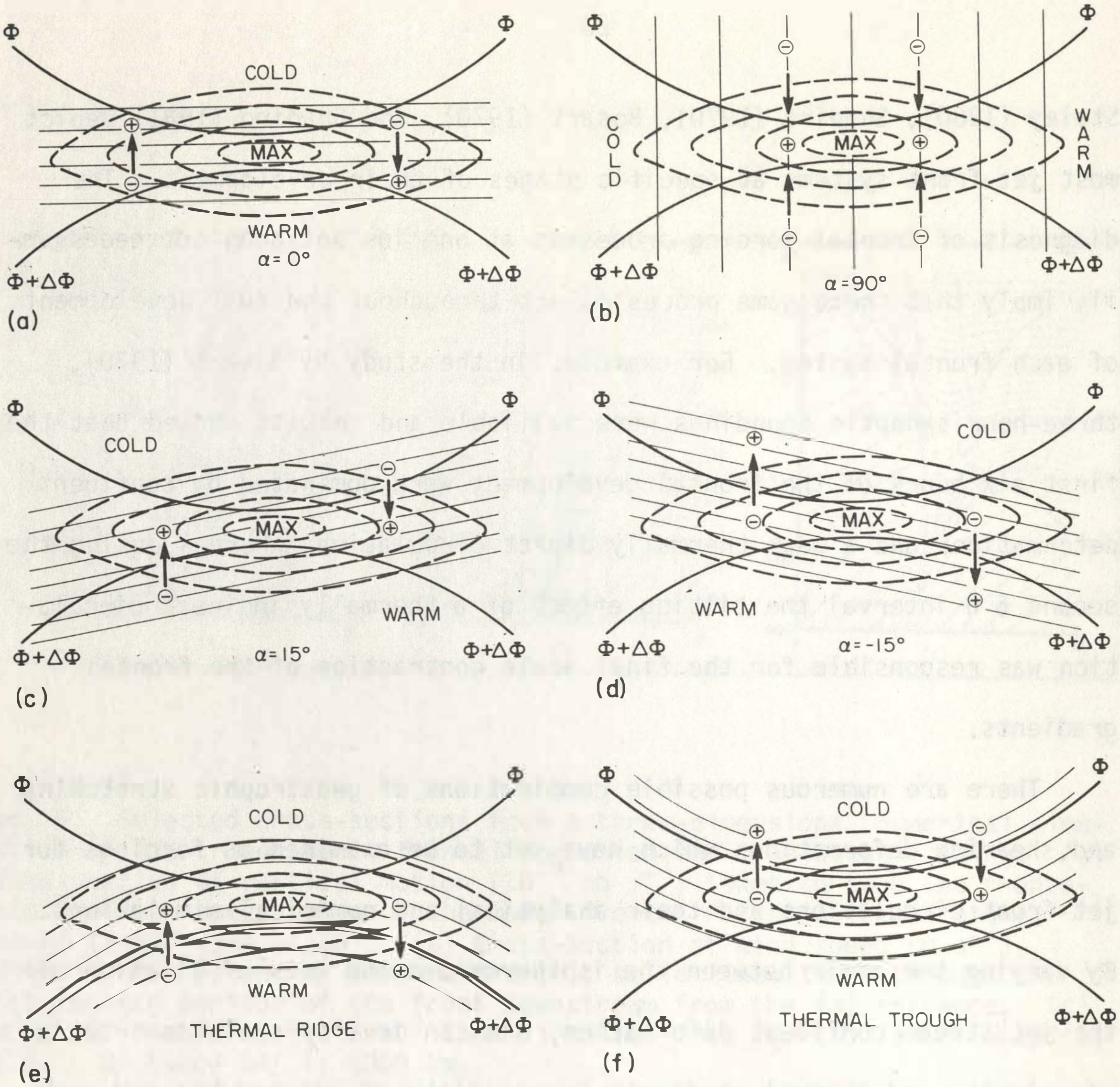

Fig. 6. Schematic illustration of mid-tropospheric geostrophic deformation fields for a straight jet stream wind maximum. Heavy solid lines, geopotential height; heavy dashed lines, isotachs; thin solid lines, isentropes; heavy solid arrow, sense of the geostrophic secondary circulation Q-forcing term of Eq. 20. North- and southward-directed Q-vectors indicate thermally direct or indirect circulation forcing, respectively. Plus and minus signs give sense of the vertical motion ω for given distributions of Q, $\omega > 0 = (+)$, $\omega < 0 = (-)$. (a) Pure stretching deformation. (b) Pure shearing deformation with $\partial\theta/\partial x > 0$. (c) Stretching plus shearing deformation with $\partial\theta/\partial x > 0$. (d) Same as (c), but for $\partial\theta/\partial x < 0$. (e) Stretching plus shearing deformations in a thermal ridge with $\partial\theta/\partial x > 0$ in the confluent entrance and $\partial\theta/\partial x < 0$ in the difluent exit. (f) Same as (e), but for a thermal trough with $\partial\theta/\partial x < 0$ in the entrance and $\partial\theta/\partial x > 0$ in the exit.

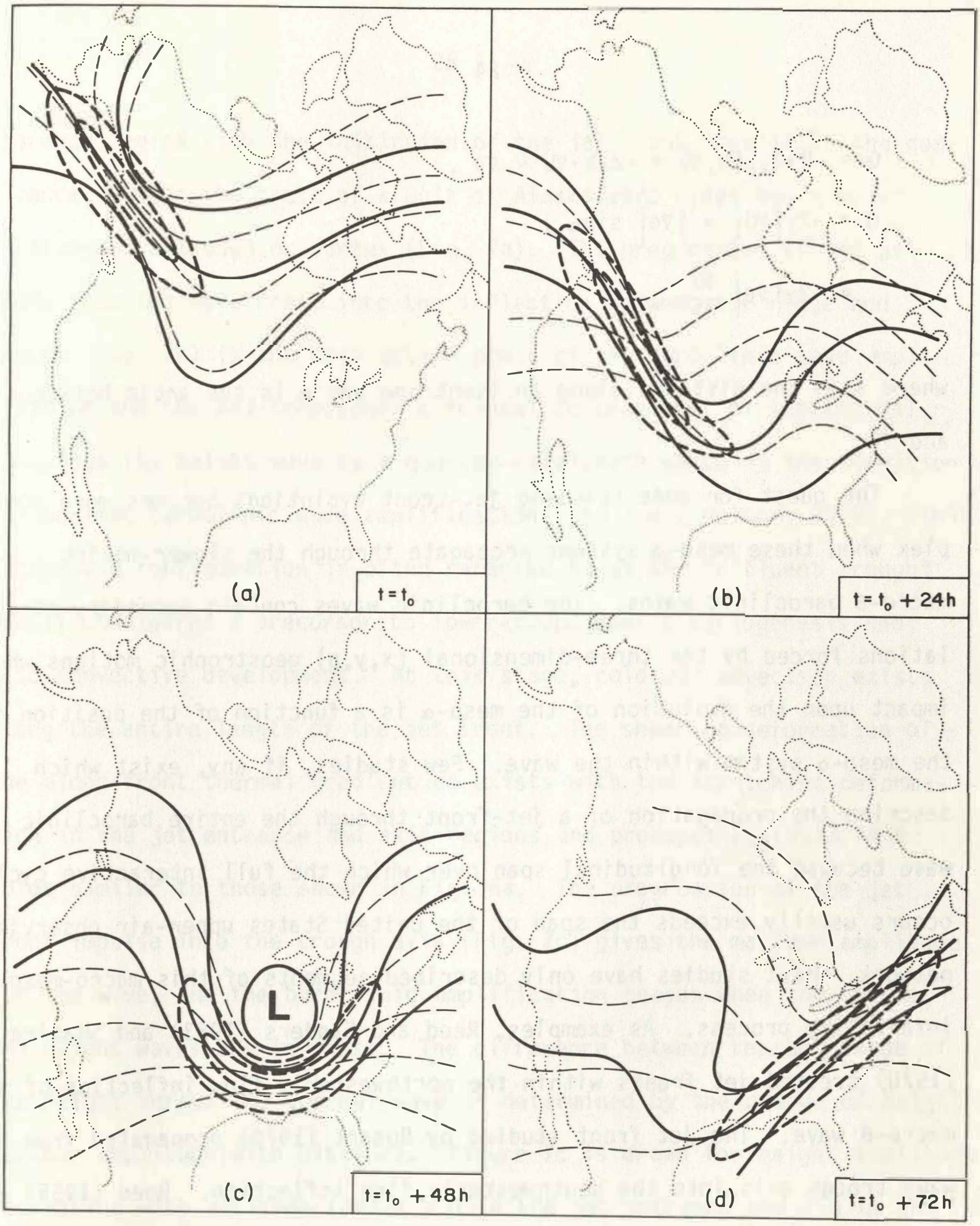

Fig. 7. Schematic depiction of the propagation of a mid-tropospheric (~400 mb) jet-front impulse through a synoptic wave over a 72 h time span. (a) Formation of initial jet-front impulse in the confluence of mid- and polar-latitude currents. (b) Jet-front situated in northwesterly flow inflection of amplifying wave. (c) Jet-front at the trough axis of fully developed wave. (d) Jet-front situated in the southwesterly flow inflection of the decaying wave. Geopotential height contours, heavy solid lines; isotachs, heavy dashed lines; potential temperatures, thin dashed lines.

$$Q = -2\gamma J_{xy}(U,\theta) = -2\gamma\hat{k}\cdot\nabla U \times \nabla\theta \ ,$$

$$Q = -2\gamma\left|\nabla U\right| \times \left|\nabla\theta\right| \sin\alpha \ ,$$

$$= -2\gamma\left|\nabla\theta\right| \frac{\partial U}{\partial s} \ , \qquad (32)$$

where s is the distance along an isentrope and α is the angle between ∇U and $\nabla\theta$.

The quest for understanding jet-front evolutions becomes more complex when these meso-α systems propagate through the slower-moving macro-β baroclinic waves. The baroclinic waves contain secondary circulations forced by the three-dimensional (x,y,p) geostrophic motions whose impact upon the evolution of the meso-α is a function of the position of the meso-α system within the wave. Few studies, if any, exist which describe the propagation of a jet-front through the entire baroclinic wave because the longitudinal span over which the full interactive cycle occurs usually exceeds the span of the United States upper-air observing network. Past studies have only described segments of this macro-meso interactive process. As examples, Reed and Sanders (1953) and Shapiro (1970) treated jet fronts within the northwesterly flow inflection of a macro-β wave. The jet front studied by Bosart (1970) propagated from the wave trough axis into the southwesterly flow inflection. Reed (1955) and Shapiro (1981) diagnosed jet-front processes in the southwesterly flow of the wave inflection.

Figure 7 presents a schematic depiction of the interaction of a traveling jet-front impulse with a slower-moving baroclinic wave. The sequence begins with the initiation of the jet front impulse in the confluence between the crest of a Gulf of Alaska wave ridge and a polar latitude wave trough or vortex (Fig. 7a). The progression of the jet front from the wave crest into the inflection between the ridge and trough (Fig. 7b) is the most active phase of the baroclinic wave amplification and the mid-tropospheric frontal contraction, as the thermal wave lags the height wave by a quarter-wavelength which is the condition for maximum baroclinic wave amplification (see i.e., Holton, 1979). This macro-meso configuration is often referred to as the "difluent trough" and is considered a precursor to lower-tropospheric cyclogenesis and meso-convective development. At this stage, cold air advection exists along the entire length of the jet front. The shearing deformation of the along-front thermal gradient co-exists with the stretching deformation in the jet entrance and exit regions and produces $J_{xy}(U,\theta)$ solenoids similar to those shown in Fig. 6a. The progression of the jet front impulse into the trough axis (Fig. 7c) gives the maximum amplitude for the wave, and the baroclinic amplification ceases when the thermal and height waves are in phase. The difference between the amplitude of the height versus the thermal wave is determined by the change of height contour amplitude with altitude. Figure 7c is drawn for height amplitude decreasing with altitude ($\partial\theta/\partial x > 0$ in the jet entrance and < 0 in the exit). In the final phase of the sequence (Fig. 7d), the impulse passes on into the inflection between the trough axis and the downstream ridge. The thermal wave leads the height wave which damps the wave amplitude. The entire jet front impulse contains warm air advection since $\partial\theta/\partial x < 0$

and the combined effects of stretching and shearing deformations are similar to those shown in Fig. 6b.

Our current ability to describe the complex sequence of events associated with macro-β meso-α interactive processes is limited by the coarse temporal (12 h) and spatial (~500 km) resolution of the operational upper-air observing network. In addition, inaccuracies in wind, temperature, and moisture measurements imposed by the archaic rawinsonde technology preclude the possibility of obtaining data bases with sufficient accuracy to resolve the temporal and spatial changes of the meso-α. At its best, the present observing system has allowed us to determine the sign and order of magnitude of the evolutionary processes. It remains for future improvements in upper-air observing technology, and the implementation thereof, to provide the time- and space-scale measurements from which meteorologists can observe, diagnose, and further their understanding of continuous evolution of the meso-α systems and their interactions with the macro-β baroclinic waves.

Fine-Scale Structure

The jet-front systems of the middle troposphere and lower stratosphere contain waves and turbulence which are important components in their evolution. Turbulent vertical fluxes of heat and momentum on the meso-β through micro-γ scale act as a "brake" upon the scale contraction of wind and temperature gradients which are continuously forced by the macro-β and macro-band meso-α geostrophic deformations and secondary circulations (see Roach, 1950). In addition, the turbulent fluxes feed back into the geostrophic motions through their contributions to the secondary circulations. It is well-documented that the fronts above and below jet streams are preferred regions for the vertical mixing of heat, momentum, and chemical trace constituents (Endlich, 1963; Lumley and Panofsky, 1964; Kennedy and Shapiro, 1975, 1980; Shapiro, 1980).

An example from Kennedy and Shapiro (1980) illustrates the turbulent fluxes within an upper front over the central United States on 11 April 1978. The cross section (Fig. 8) shows the jet speeds exceeding 80 m s^{-1} and vertical wind speed and directional shears of 40 m s^{-1} $(100 \text{ mb})^{-1}$ and 90 deg. $(100 \text{ mb})^{-1}$, respectively, within the frontal layer. The intensity of the vertical shear may be seen in the Sabreliner descent through the front (Fig. 9). The Sabreliner encountered severe CAT on two penetrations of this upper front. The measured downward flux of heat and momentum (Fig. 10) contained spectral contributions ranging from the < 50 km meso-β down to the < 1 km micro-γ turbulent dissipation. A composite of the Sabreliner and commercial aircraft CAT encounters (Fig. 11) illustrates the typical areal extent of CAT mixing within upper jet-front systems.

The impact of turbulent vertical fluxes upon the evolution of sloping frontal layers is through the flux terms of (14)-(20). For a flux distribution that is proportional to the vertical wind shear and/or inverse of the Richardson number (Gidel and Shapiro, 1979), the turbulent motions act to dissipate vertical and horizontal gradients of the meso-α scale structure.

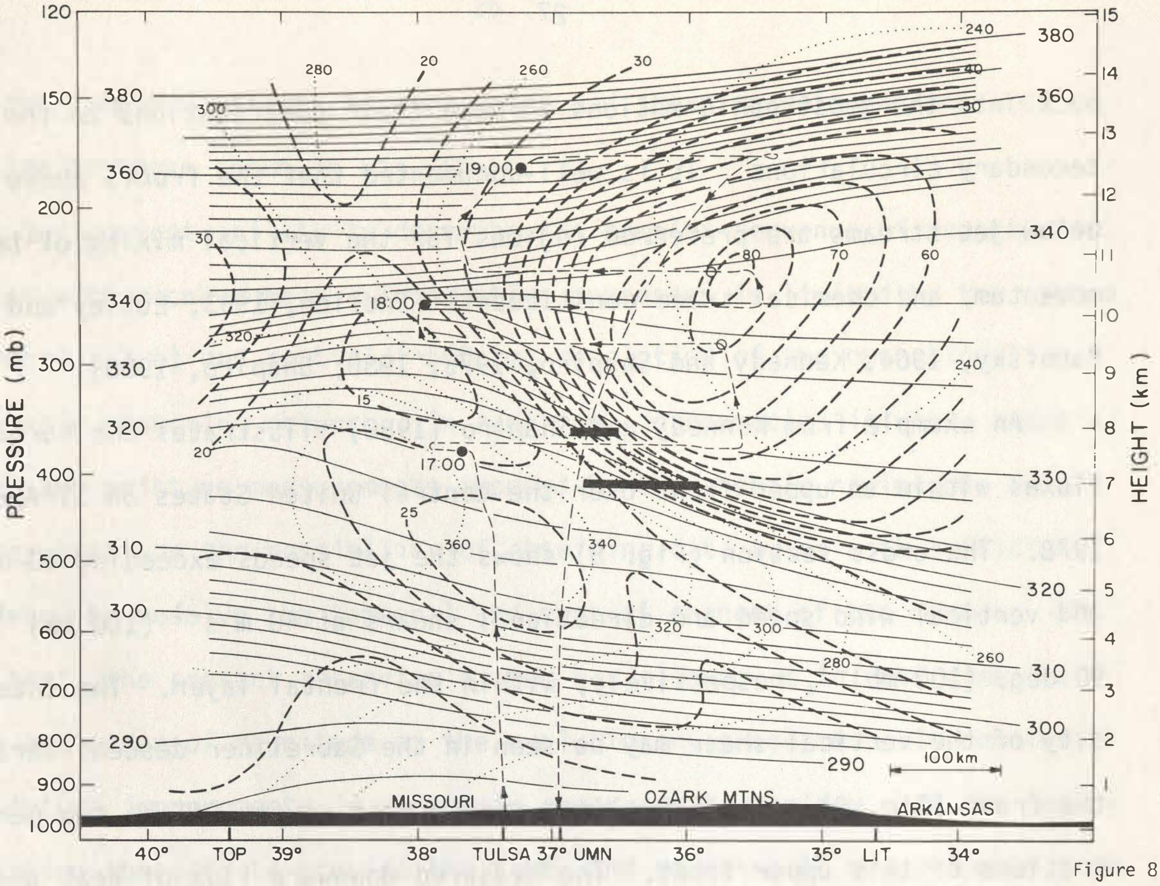

Figure 8

Fig. 8. Cross-section of potential temperature (K, solid lines), wind speed (m s^{-1}, dashed lines) and wind direction (deg. dotted lines) on 11 April 1978. Flight track indicated with arrowed dashed line. Solid circles indicate hours GMT, open circles half-hours. NWS balloon soundings from Topeka (TOP), Monett (UMN) and Little Rock (LIT) aided in this analysis. Two heavy solid line segments represent the turbulent passes shown in Fig. 10 (after Kennedy and Shapiro, 1980).

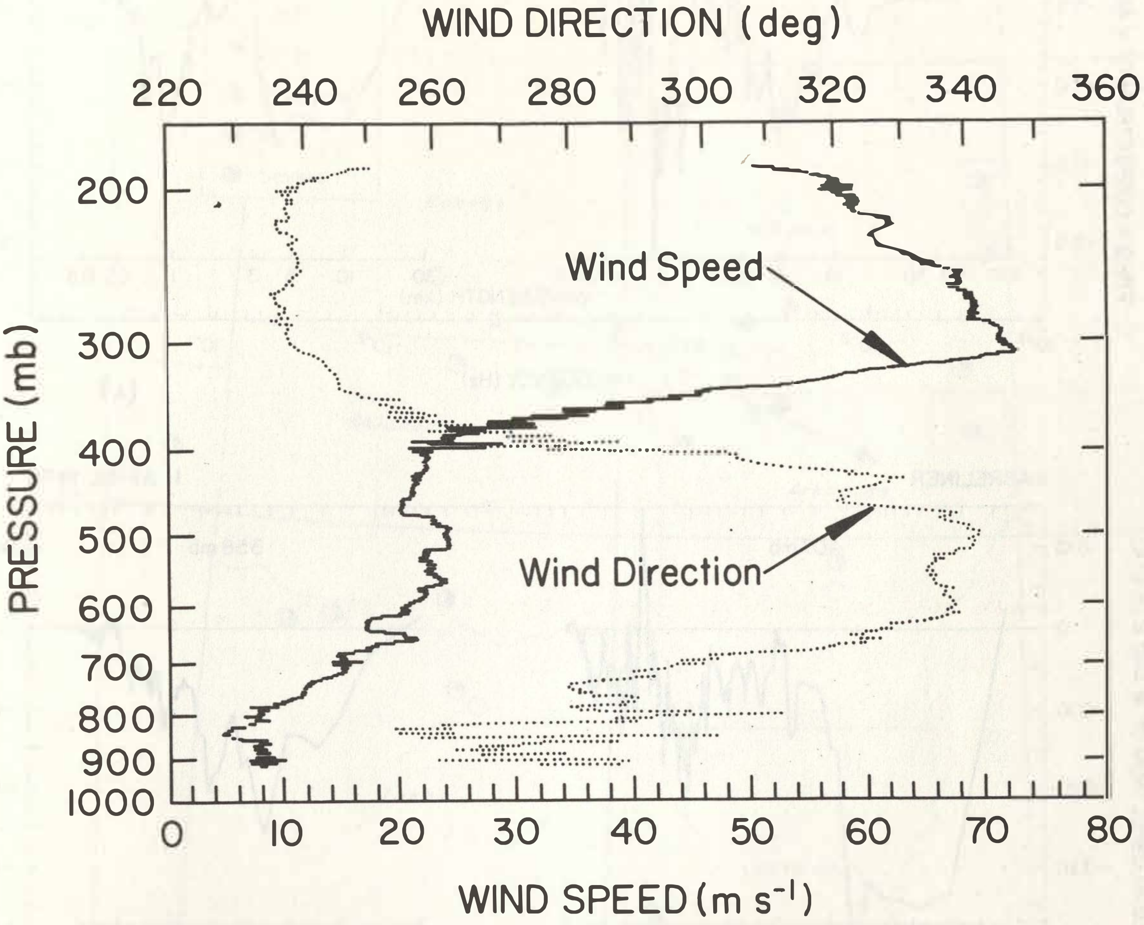

Fig. 9. Sabreliner sounding of wind speed and direction through the frontal zone of 11 April 1978. The descent from 185 mb in the flight track on Fig. 8 (center) shows the location and time of the sounding (after Kennedy and Shapiro, 1980).

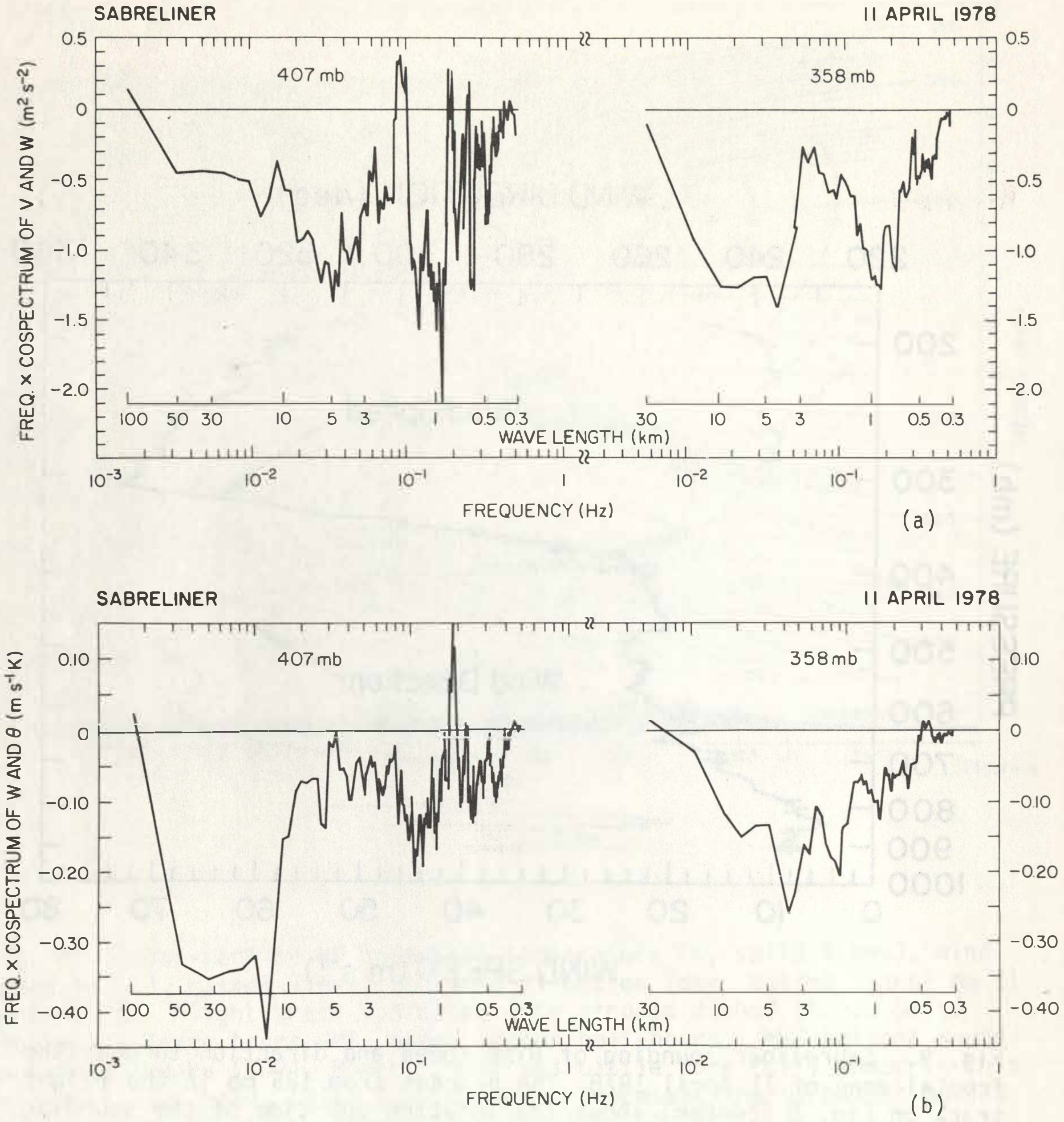

Fig. 10. Vertical flux of heat and momentum in clear-air turbulence for turbulent patches in Fig. 8. (a) Cospectra of horizontal and vertical wind for the 407 and 358 mb passes through clear-air turbulence, 11 April 1978. Ordinate is multiplied by frequency to render a variance area-conserving plot. (b) As in (a), except for vertical wind and potential temperature.

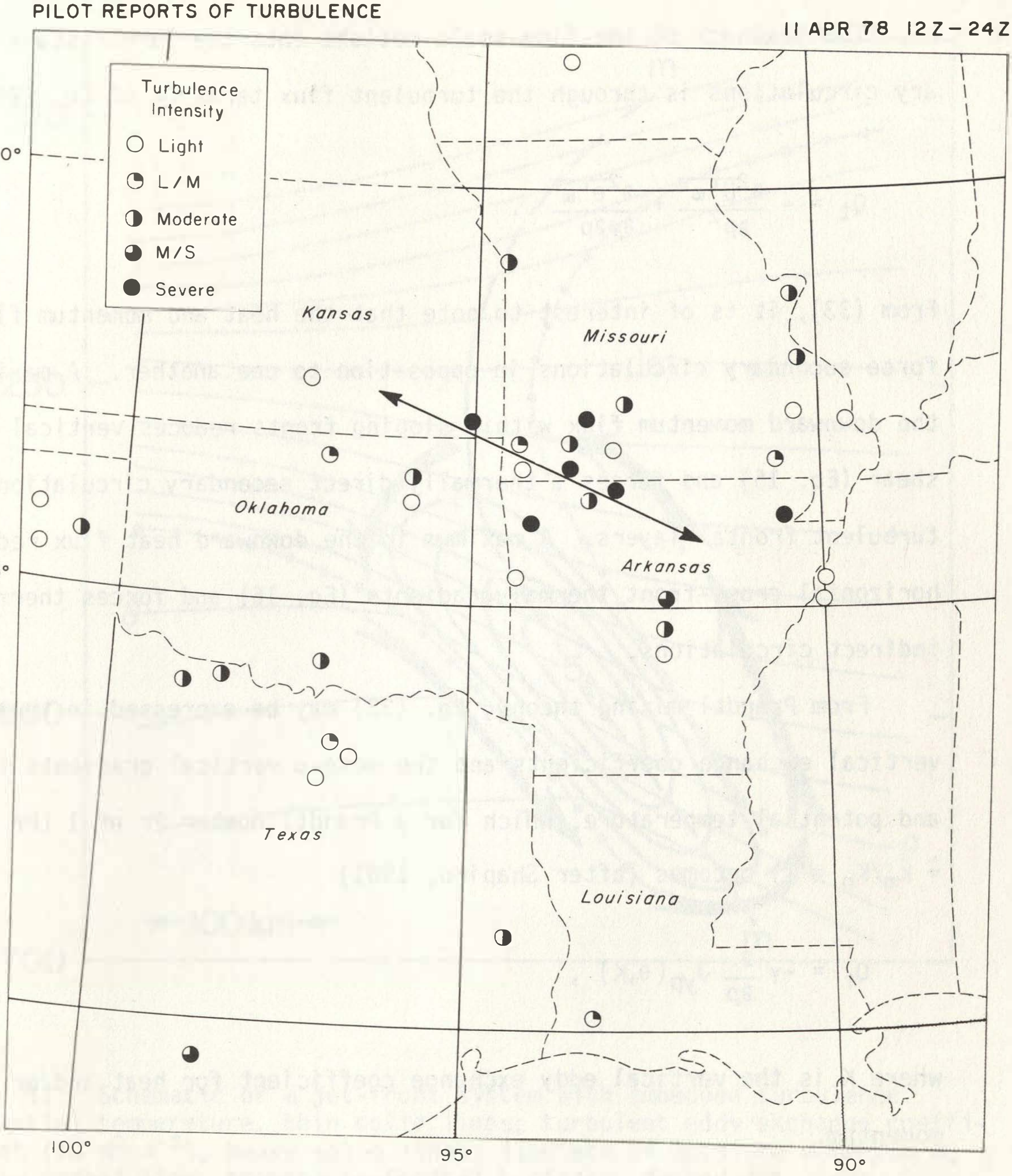

Fig. 11. Pilot reports of turbulence over the central United States from 1200 to 2400 GMT 11 April 1978. The approximate tracks of the Sabreliner during its research flight on this day (Fig. 8) are represented by the oblique line near the center.

The feedback of the fine-scale motions into the larger-scale secondary circulations is through the turbulent flux terms Q_t of Eq. (20)

$$Q_t = - \frac{\partial^2 \overline{U'\omega'}}{\partial p^2} + \frac{\partial^2 \overline{\theta'\omega'}}{\partial y \partial p} \quad . \tag{33}$$

From (33), it is of interest to note that the heat and momentum fluxes force secondary circulations in opposition to one another. A maximum in the downward momentum flux within sloping fronts reduces vertical wind shear (Eq. 15) and forces a thermally direct secondary circulation about turbulent frontal layers. A maximum in the downward heat flux reduces horizontal cross-front thermal gradients (Eq. 16) and forces thermally indirect circulations.

From Prandtl mixing theory, Eq. (33) may be expressed in terms of vertical exchange coefficients and the meso-α vertical gradients in wind and potential temperature, which for a Prandtl number Pr of 1 (Pr $= K_m/K_h = 1$) becomes (after Shapiro, 1981)

$$Q_t = -\gamma \frac{\partial}{\partial p} J_{yp}(\theta, K) \quad , \tag{34}$$

where K is the vertical eddy exchange coefficient for heat and/or momentum.

The relative importance of momentum versus heat fluxes in the turbulent forcing of secondary circulations may be qualitatively illustrated by considering a representative distribution of K and θ within an upper

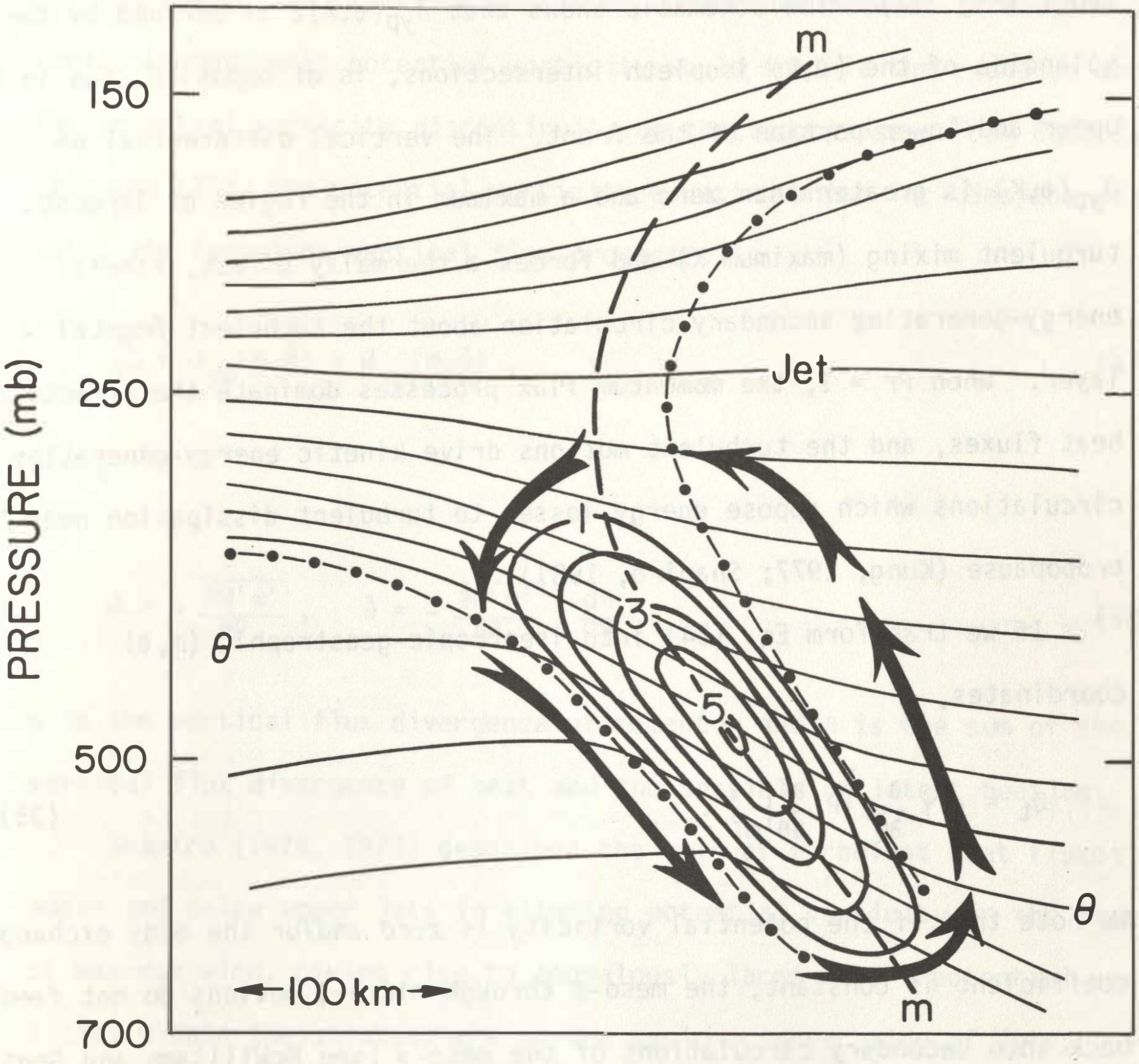

Fig. 12. Schematic of a jet-front system with embedded turbulence. Potential temperature, thin solid lines; turbulent eddy exchange coefficient ($10\ m^2\ s^{-2}$), heavy solid lines; isopleth of absolute momentum m, heavy dashed line; tropopause-frontal surfaces, dashed-dot lines.

front (Fig. 12). The schematic shows that $J_{yp}(\theta,K)$, as defined by the solenoids of the (θ,K) isopleth intersections, is of opposite sign in the upper and lower portion of the front. The vertical differential of $J_{yp}(\theta,K)$ is greater than zero and a maximum in the region of largest turbulent mixing (maximum K) and forces a thermally direct, kinetic energy-generating secondary circulation about the turbulent frontal layer. When Pr = 1, the momentum flux processes dominate the effects of heat fluxes, and the turbulent motions drive kinetic energy-generating circulations which oppose energy losses to turbulent dissipation near the tropopause (Kung, 1977; Shapiro, 1981).

If we transform Eq. (34) into isentropic-geostrophic (m,θ) coordinates,

$$Q_t = -\gamma \frac{\partial}{\partial p} \left[P \left.\frac{\partial K}{\partial \theta}\right|_m\right] . \tag{35}$$

We note that if the potential vorticity is zero and/or the eddy exchange coefficient is constant, the meso-β through micro-γ motions do not feed back into secondary circulations of the meso-α [see McWilliams and Gent, 1980; Shapiro, 1981, for a discussion of (m,θ) coordinates].

Air and chemical trace constituents are exchanged between the stratosphere and troposphere through the actions of the fine-scale motions. In the absence of diabatic and viscous processes, potential vorticity is invariant along a three-dimensional trajectory

$$\frac{dP}{dt} = \frac{d}{dt} J_{yp}(m,\theta) = 0 , \tag{36}$$

and the one to two orders-of-magnitude difference between stratospheric versus tropospheric potential vorticity would inhibit the exchange across the potential vorticity discontinuity of the tropopause. From Eqs. (14)-(17) and (36), the potential vorticity equation which includes the diabatic and turbulent vertical flux processes is

$$\frac{dP}{dt} = J_{yp}(\theta, \dot{m}) - J_{yp}(m, \dot{\theta}) , \qquad (37)$$

where

$$\dot{m} = - \frac{\partial \overline{U'\omega'}}{\partial p} , \quad \dot{\theta} = - \frac{\partial \overline{\theta'\omega'}}{\partial p} + \frac{d\theta}{dt} . \qquad (38)$$

m is the vertical flux divergence of momentum and θ is the sum of the vertical flux divergence of heat and the sensible or latent heating.

Shapiro (1976, 1978) described the role of turbulent heat fluxes above and below upper jets in altering potential vorticity in the layer of maximum wind, giving rise to anomalously large meso-α potential vorticity within the stratosphere on the cyclonic shear side of jets. Gidel and Shapiro (1979) parameterized heat and momentum fluxes within a numerical simulation of jet-front formation and demonstrated the role of the turbulent fluxes in changing potential vorticity which allows for the free exchange of air between the stratosphere and troposphere. It should be emphasized that turbulent fluxes redistribute existing potential vorticity such that increases in one region are balanced by losses in another. The integral of the potential vorticity over the entire jet-front domain is conserved and may be changed only through diabatic heat sources and sinks within and turbulent dissipation at or fluxes through the boundary of the domain.

The role of turbulent mixing processes in exchanging chemical trace constituents (ozone, water vapor, anthropogenic pollutants, etc.) between the stratosphere and troposphere is described in Shapiro (1980). Results revealed a simultaneous downward flux of stratospheric ozone and upward flux of tropospheric dust particles across the "folded" tropopause associated with jet-front systems. The concentrations of chemical trace constituents within tropopause folds and the adjacent troposphere are altered through the vertical divergence of the eddy flux of these constituents (see Eq. 5).

Our understanding of the fine-scale structure of upper-level jet-front systems is limited by the sparseness of direct observations. Research aircraft measurements have provided estimates of the kinetic energy budget of turbulent patches (Dutton, 1969; Kennedy and Shapiro, 1975, 1980) and illustrate the nonsteady character of vertical mixing processes as the diagnosed cases did not always yield a balance between turbulent energy gains from the mean vertical shear and losses to thermal buoyancy and turbulent dissipation. Geosynchronous spacecraft show visible images of wave structures having wavelengths of 1 to 50 km which appear as lenticular cloud bands below or above frontal layers or beneath the tropopause. Wavelengths, wave front orientations, and phase velocities are easily discernible from high space-time resolution images. However, the energy transfers by the turbulent fluxes are indeterminant, and it is not possible to differentiate between cloud structures induced by ducted gravity waves and turbulent fluxing motions discussed above. Ground-based measurements by weather radar have documented the life cycle of breaking waves within elevated frontal layers and low-level inversions (Reed and Hardy, 1972; Metcalf, 1975). The reflection of the radar pulse by turbulence gives wave amplitude, orientation, wavelength, and propagation velocity, but not the thermal and three-dimensional air motion distribution. Because of the limitations of these observing systems, it remains for technological advances, such as the refinement of doppler lidars and UHF/VHF radars, to provide a continuously monitoring observational system to measure the four-dimensional life cycle of the fine-scale structures embedded within jet-front systems.

Our understanding of the sources for the instabilities from which meso-β through micro-γ motions within fronts arise is quite speculative. A wide variety of structures is observed within mesoscale systems. Their wavelengths range from 30 km to < 1 km and their orientations are both longitudinal to and transverse to the meso-α vertical wind shear vector (Reed and Hardy, 1972; Kennedy and Shapiro, 1975, 1980; Shapiro and Kennedy, 1976). The sparsity of observational documentation allows us only to hypothesize as to the various physical mechanisms, and at most fantasize about interactions between several mechanisms acting simultaneously, which contribute to the turbulent fluxes within a specific mesosystem.

We may summarize several mechanisms which can excite fine-scale motions within upper fronts:

1. Kelvin-Helmholtz shearing instability is generated by the vertical scale contraction of velocity gradients to the limit at which the Richardson number becomes less than 0.25. The instability is released by the Kelvin-Helmholtz waves whose wavefronts are oriented normal to the mean vertical wind shear vector across the unstable layer. The energy of the turbulent mixing is drawn from vertical shear of the meso-α.

2. Dry or moist convective overturnings in the layer beneath fronts can perturb ducted gravity waves within thermally stable frontal layers above. Trapped gravity waves are not efficient at transferring heat and momentum vertically (Shapiro and Kennedy, 1975), but may create subcritical Richardson number shear layers of their ridges and troughs within which mixing can occur.

3. Diabatic (latent) heating at frontal boundaries, or turbulent mixing within, can render potential vorticity less than zero and generate symmetric instability overturnings within fronts.

4. Meso-convective heating and/or momentum fluxes may generate negative potential vorticity at the anticyclonic shear side of jet streams in the layer between the tropopause and the upper surface of fronts. The resulting symmetric instability overturnings are transverse (wave fronts parallel to the wind) and can initiate wave motions and turbulence in vertical shear layers above the tropopause and below in the mid-tropospheric front.

It remains for future research to determine the exact nature and four-dimensional evolution of the fine-scale motions within jet-front systems. Through an understanding of the relationship between meso-α instabilities and the induced fine-scale processes, we may develop realistic parameterization of these processes within mesoscale numerical simulation and prediction models.

4. Surface Fronts

The relationship between synoptic cyclones, surface fronts, and precipitation was composited into the "Norwegian cyclone model" by Bjerknes (1919) and Bjerknes and Solberg (1922). By combining surface observations, cloud motion winds, and upper-air observations from kites and balloons, these pioneering researchers set forth the conceptual model for diagnosing and predicting three-dimensional air motions and associated weather within cyclones and about fronts. The advances in understanding and forecasting northern European weather achieved through this model led to its utilization as a forecasting tool over extratropical latitudes of both the Northern and Southern Hemispheres. Though weather predictions are presently made using dynamical-numerical techniques, the operational models lack sufficient computational resolution to resolve frontal-scale structures and their associated precipitation systems. For this reason, the numerical output is "sharpened up" by a subjective utilization of the Norwegian cyclone model which places the fronts and precipitations within the numerically predicted cyclones.

The differences in topography and land-water distribution between the central United States and northern Europe led to more complex conceptual models of surface frontal evolutions and associated precipitation systems (see Newton, 1963; Carlson, 1980). These orographic influences generate regional frontal phenomena such as (1) cold air damming and upslope precipitation as surface fronts interact with the lee of the Rocky Mountains, (2) virtual temperature (moisture) fronts or drylines which form between dry Mexican plateau flows and moist Gulf of Mexico

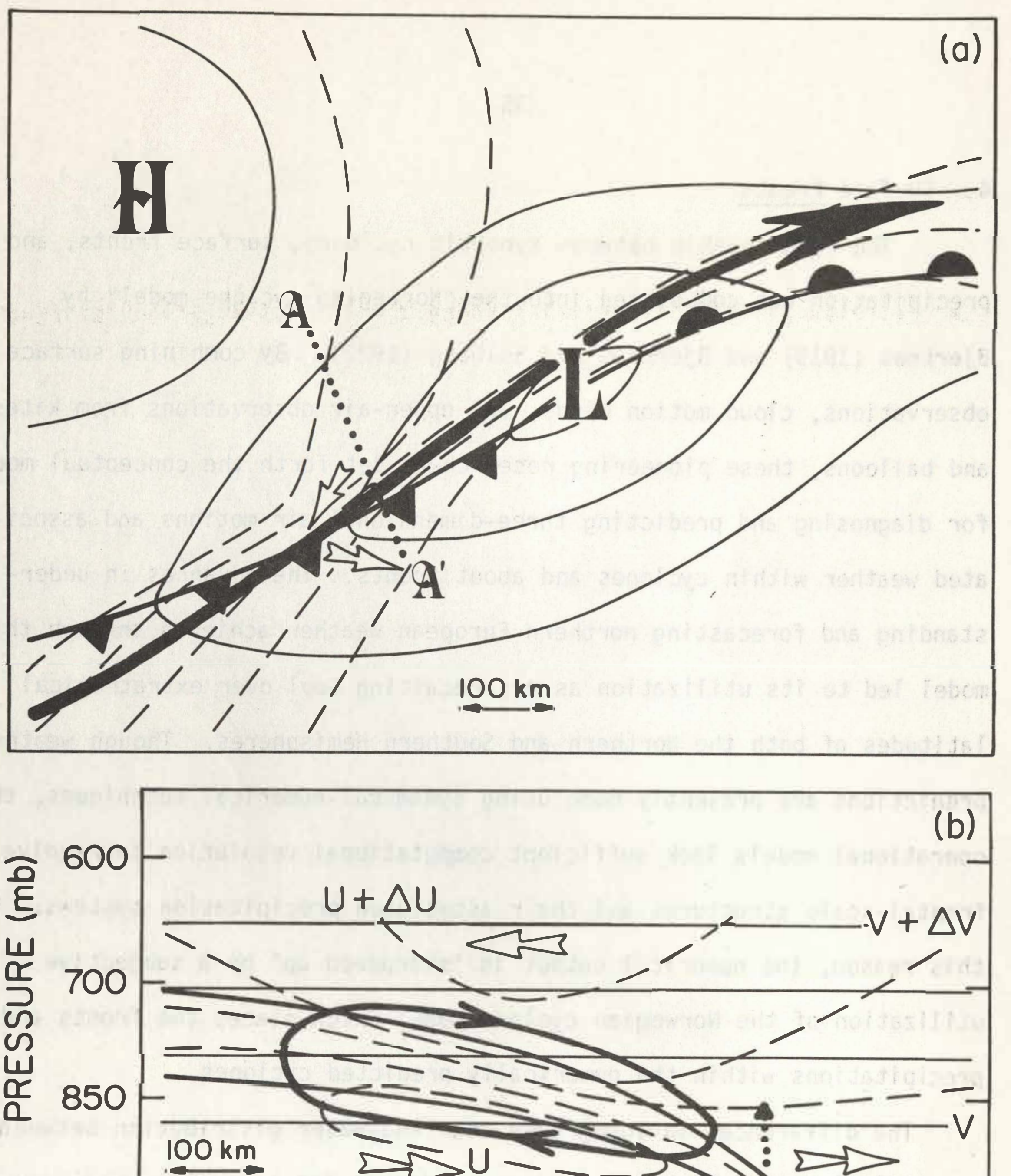

Fig. 13. (a) Schematic of an incipient cyclone with a subsiding cold front. Cold and warm front leading edges, conventional symbols; surface isobars, solid lines; surface temperature, dashed lines; mid-tropospheric height contour and direction of flow, heavy solid barbed arrow; surface geostrophic flow, opened short arrows. (b) Cross-section along line AA' across the front of (a). Frontal boundaries, heavy solid lines; along-front geostrophic wind U, dashed lines; cross-front geostrophic wind V, thin solid lines; direction of V, open arrows; secondary circulation forced by the geostrophic shearing deformation with $\partial V/\partial p < 0$, heavy barbed line; boundary-layer convergence and vertical motion at leading edge of front, dotted arrows.

air, (3) cold front-dryline occlusions which occur when Pacific cold fronts intercept moist Gulf air at the dryline, forcing the dry surface air aloft in the occlusion process, and (4) lee fronts which form under conditions of northerly flow where the sharp gradients in surface roughness between the east-west-oriented canyon topography of the lee slope and smooth plains force surface frontal convergence and precipitation in the lee. In the discussion that follows, we shall first treat the classical surface fronts within the various phases of the evolution of the Norwegian cyclone. Geostrophic forcings, ageostrophic responses, and boundary-layer heating and vertical flux processes will be described within the context of specific frontal evolutions. The discussion of the classical surface fronts (i.e., cold fronts and warm fronts) is followed by a discussion of some local frontal phenomena characteristic of the Central U.S.

Incipient phase

The Sawyer-Eliassen circulation equation (Eq. 20) may be applied to the fronts within the Norwegian cyclone model. The incipient phase of the developing cyclone (Fig. 13a) is characterized by a weak surface circulation which grows within the pre-existing baroclinicity of the polar front. The surface flow is from the north behind the cold front but switches to the southwest in the mid-troposphere above. The cold front is oriented nearly east-west during this phase of the cyclone and the cyclonic shearing deformation acts to destroy the cross-front thermal gradient. The vertical cross-section through the front (Fig. 13b) taken along the line AA' of Fig. 13a shows the front-normal geostrophic wind increasing with height $\partial V/\partial p < 0$, in the presence of cyclonic shear in the along-front flow $\partial U/\partial y < 0$. The resulting shearing deformation for (20) drives a thermally indirect circulation about the front, with subsiding motions above and ascending below. Ascending motions and convergence necessary to maintain the frontal structure at the leading edge are driven by surface boundary layer processes (Keyser and Anthes, 1982). The classical example of a surface cold front of this type was presented by Sanders (1955). Numerical treatments by Orlanski and Ross (1977) and Gidel (1978) with $\partial V/\partial p < 0$ were of limited success because of the noninclusion of boundary-layer physics.

Figures 14-17 present an example of a subsiding cold front over the central United States on 11 March 1975. During the early morning hours (1200 GMT, Fig. 14), the front was stalled across Kansas, well defined by its wind shift but poorly defined in the surface thermal field. The north side of the front was blanketed by stratocumulus and fog which were capped by the lower surface of the frontal inversion. South of the surface front, the air was cloudfree, permitting radiative nocturnal cooling which was inhibited north of the front by the insulating cloud layer. The northeasterly geostrophic flow beneath the front switched to southwesterly flow aloft, as is characteristic of eastwest-oriented subsiding cold fronts (Fig. 13). The potential temperature cross-section (Fig. 16a) shows the merging of the thermal structure of the front with the nocturnal boundary-layer inversion. The detailed structure of the leading edge of the front beneath the boundary layer inversion was documented

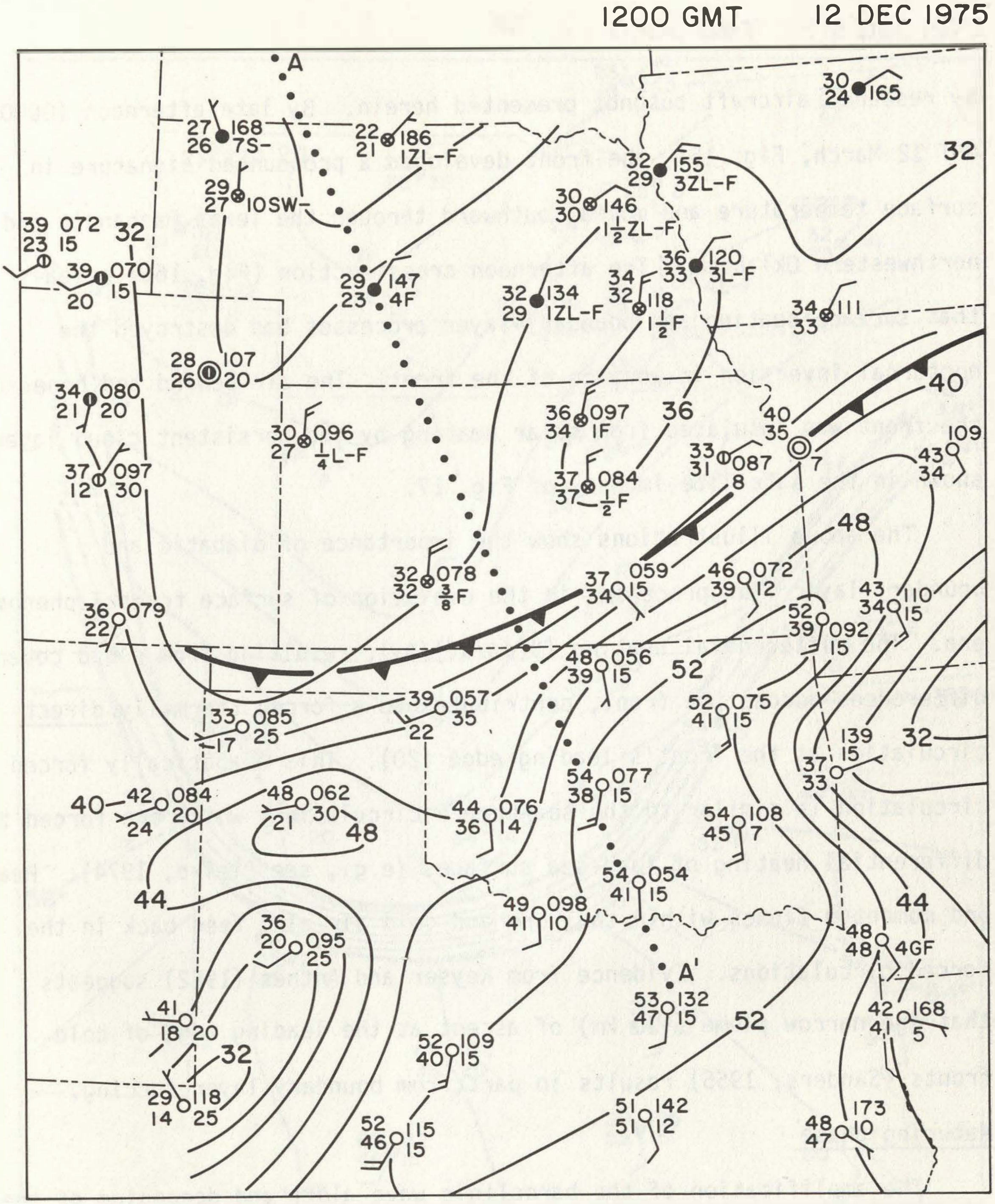

Fig. 14. Surface frontal and temperature (°F) analysis at 1200 GMT 12 December 1975. Line AA', projection line for Fig. 16(a) cross section.

by research aircraft but not presented herein. By late afternoon (0000 GMT 12 March, Fig. 15), the front developed a pronounced signature in surface temperature and moved southward through the Texas Panhandle and northwestern Oklahoma. The afternoon cross section (Fig. 16b) reveals that surface heating and boundary-layer processes had destroyed the nocturnal inversion in advance of the front. The air behind and beneath the front was insulated from solar heating by the persistent cloud layer shown in the satellite imagery of Fig. 17.

The above illustrations show the importance of diabatic and boundary-layer flux processes in the evolution of surface frontal phenomena. The differential heating ($\partial(d\theta/dt)/\partial y$), resulting from cloud cover differences across the front, contributes to a forced thermally *direct* circulation at the front's leading edge (20). This diabatically forced circulation is similar to the sea-breeze circulations which are forced by differential heating of land-sea surfaces (e.g., see Pielke, 1974). Heat and momentum fluxes within the warm and cold air also feed back in the forced circulations. Evidence from Keyser and Anthes (1982) suggests that the narrow plume (~20 km) of ascent at the leading edge of cold fronts (Sanders, 1955) results in part from boundary-layer forcing.

Maturing phase

The amplification of the baroclinic wave aloft and deepening of the surface cyclone create geostrophic deformations that are favorable for the scale contraction of cold and warm fronts and their associated secondary circulations. During the maturing phase of the cyclone (Fig. 18a), the cold front takes on a north-south orientation and is forced by

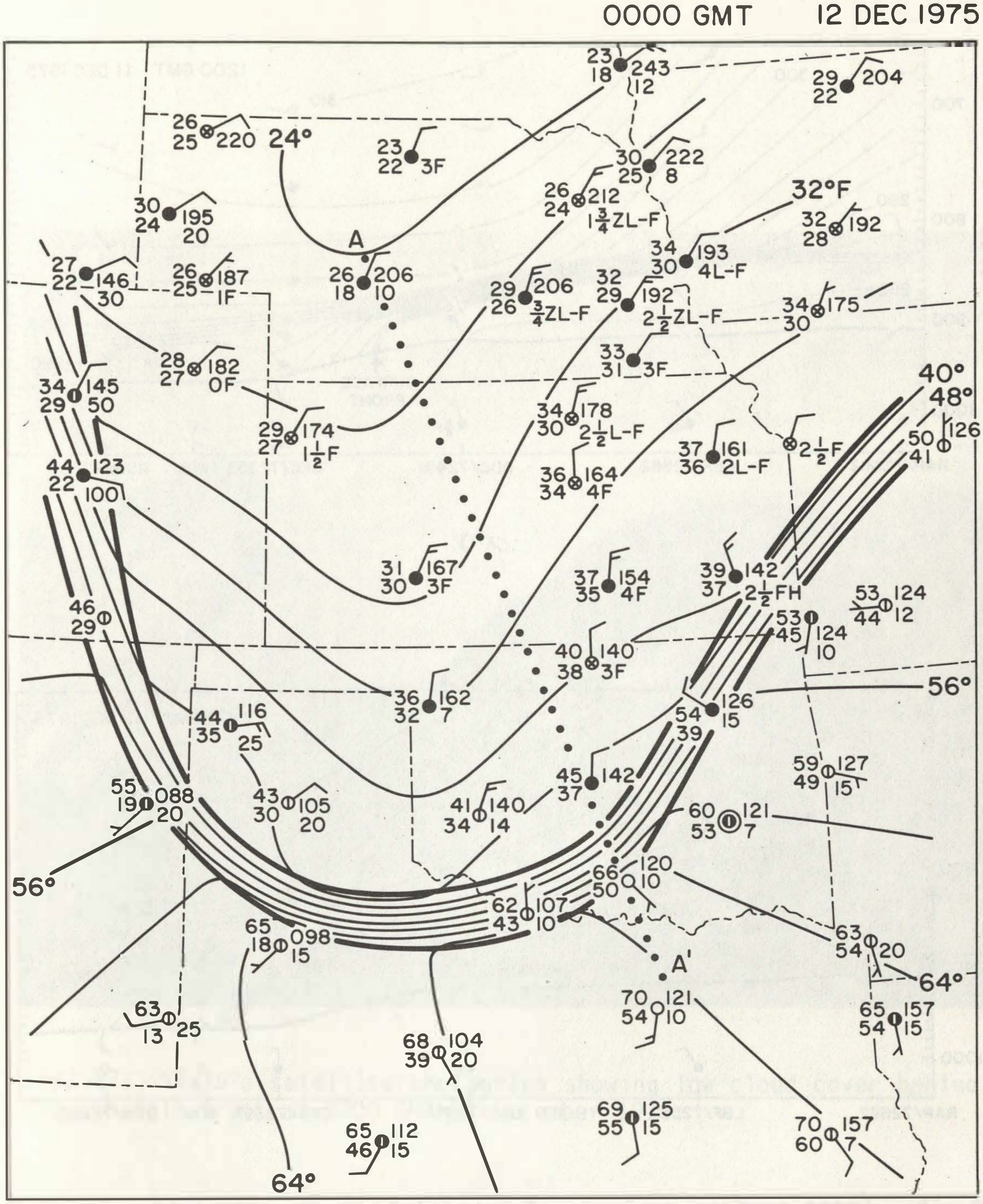

Fig. 15. Surface temperature (°F, thin lines) analysis at 0000 GMT 12 December 1975. Frontal boundaries, heavy solid lines, line AA', projection line for Fig. 16(b).

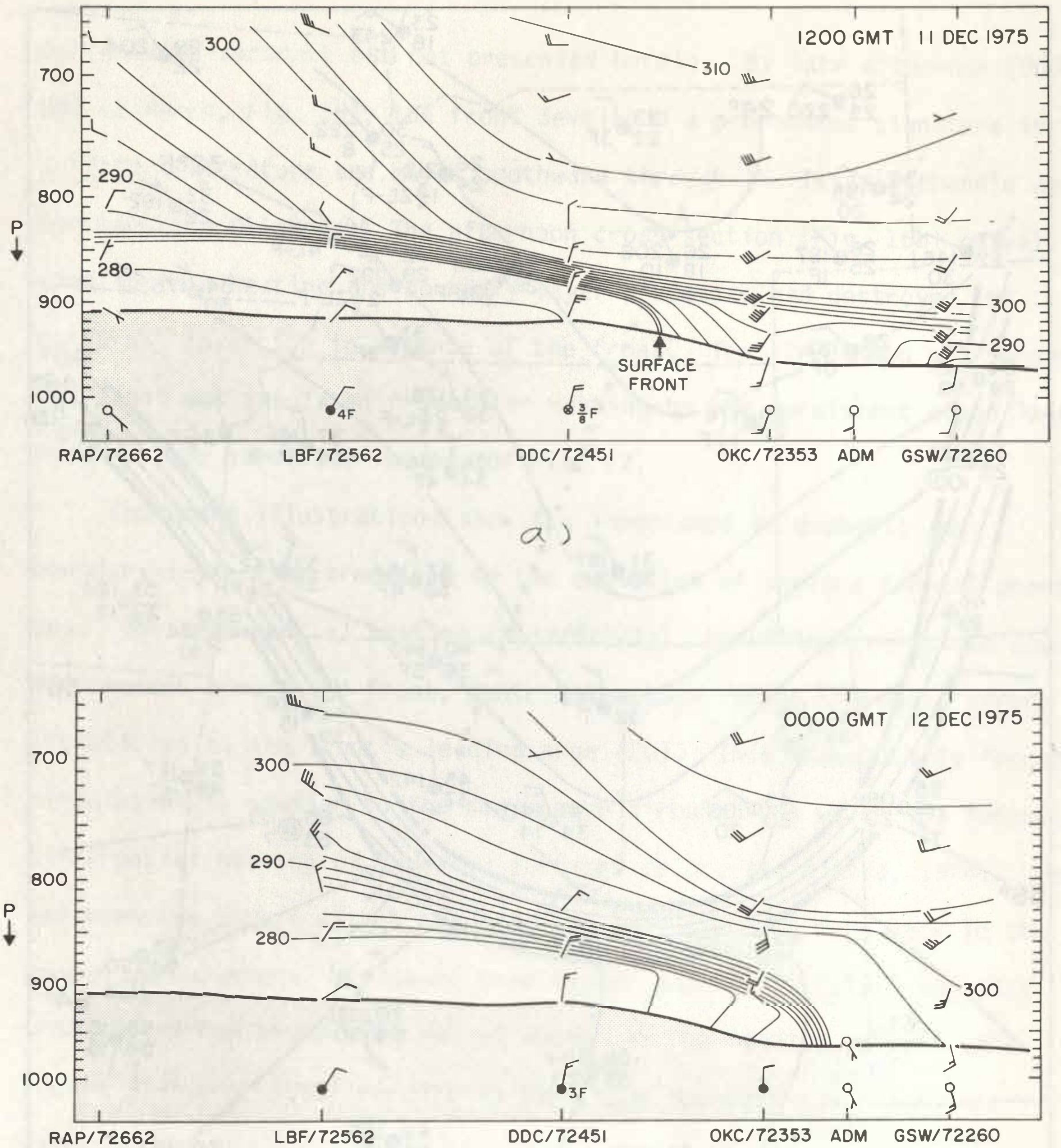

Fig. 16. Cross-section analysis of potential temperature (K) through the subsiding cold front of Figs. 14 and 15. (a) 1200 GMT 11 December 1975. (b) 0000 GMT 12 December 1975. Wind flags and barbs (kts), surface observations indicated at lower portion of figures.

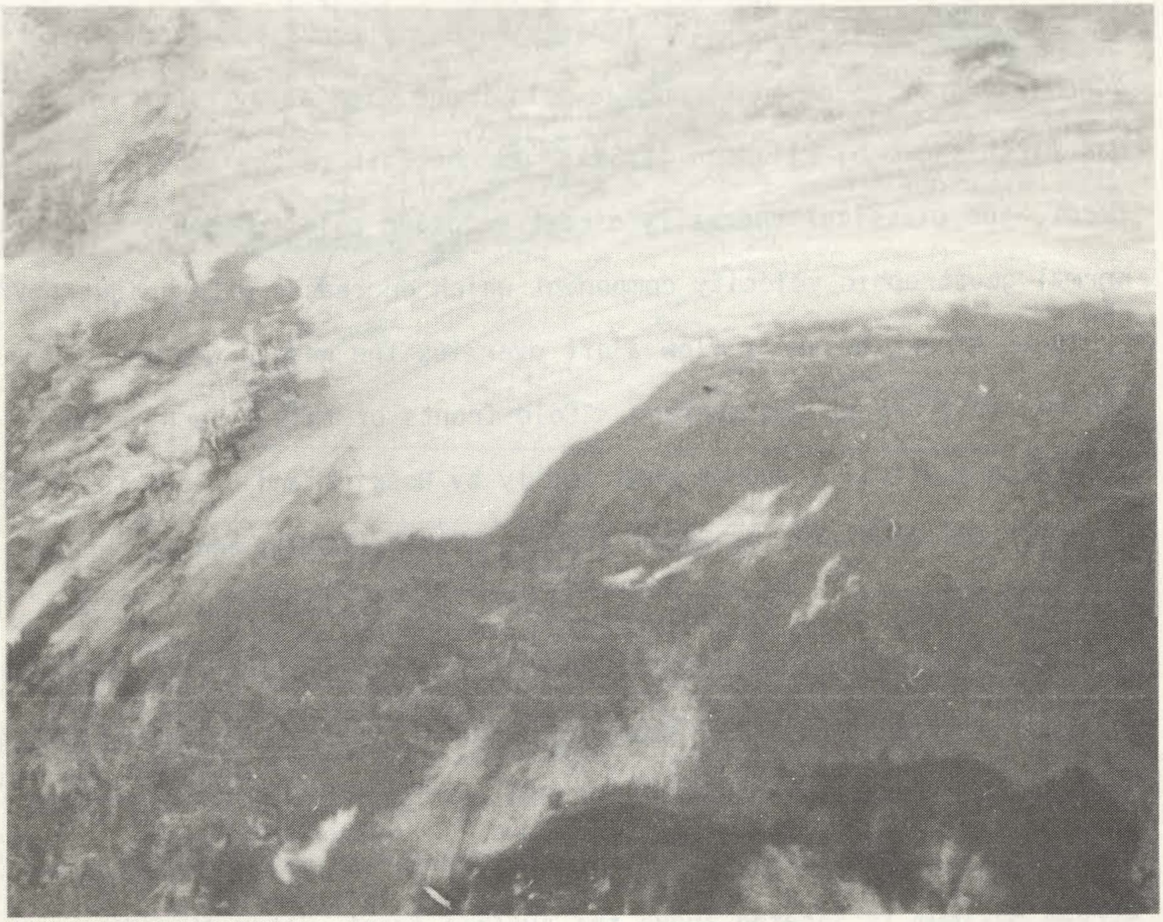

Fig. 17. Visible satellite photograph showing low cloud cover behind Fig. 15 cold front at 2000 GMT 11 December 1975.

a shearing deformation having a negative along-front thermal gradient ($\partial\theta/\partial x < 0$) in the presence of cyclonic shear ($\partial u/\partial y < 0$) across the front. This geostrophic forcing drives a thermally direct circulation with ascending motions at the leading edge and above the front. The schematic cross section through a cold front with $\partial\theta/\partial y < 0$ (Fig. 18b) was first shown by Eliassen (1962). In contrast to the subsiding cold front, the classical thermally direct maturing cold front has a front-normal geostrophic velocity component which decreases with height ($\partial V/\partial p > 0$), as strong westerly flow aloft overlies the weaker westerly flow behind the front at the surface. Cold fronts of this type have been studied analytically and/or numerically by Hoskins and Bretherton (1972), Orlanski and Ross (1977), Gidel (1978), Blumen (1980), and Keyser and Anthes (1982).

An example of a north-south-oriented cold front over the southwestern United States (Fig. 19) shows geostrophic cold air advection behind and warm air advection ahead of the 850 mb intersection of the front, with $\partial\theta/\partial x < 0$ and $\partial U/\partial y < 0$ within the front. A strong westerly jet stream maximum is located above the surface front within the mid- and upper-troposphere (Fig. 20) and hence there is a decrease in the front-normal geostrophic wind with height ($\partial V/\partial p > 0$). The detailed structure and evolution of this front are the subject of the case study presented in section 8.

The evolution of the warm front during the maturing phase of the cyclone takes place within the Bergeron stretching geostrophic deformation in the northeastern sector of the cyclone (Fig. 18a). The confluent

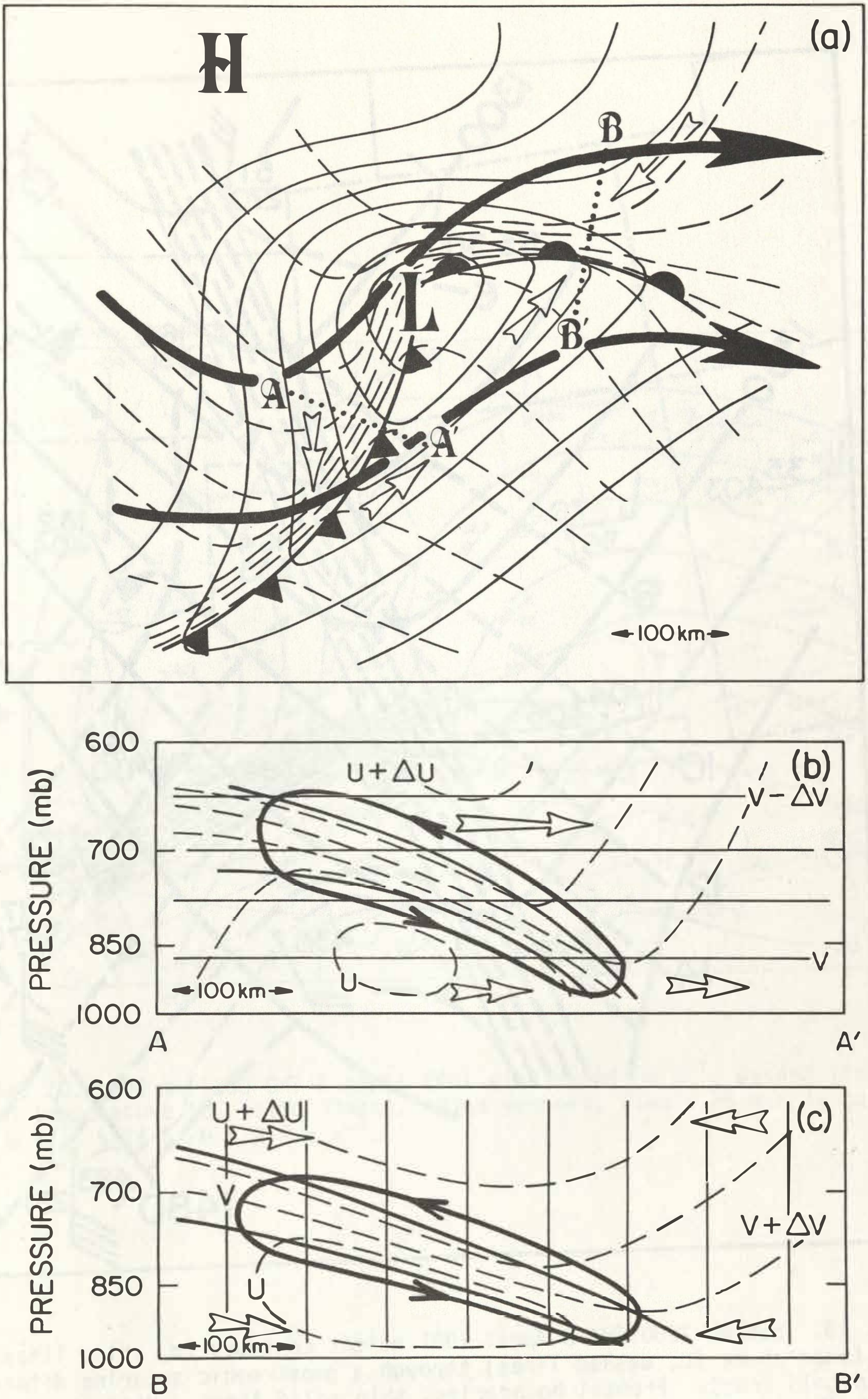

Fig. 18. (a) Same as Fig. 13(a) but for maturing cyclone with cold and warm fronts. Lines AA' and BB', projections for (b) and (c), respectively. (b) Cross section along AA' through the (a) cold front. Frontal boundaries, isopleths and secondary circulation with ($\partial V/\partial p > 0$), same as Fig. 13(b). (c) Cross section along BB' of (a) through the warm front.

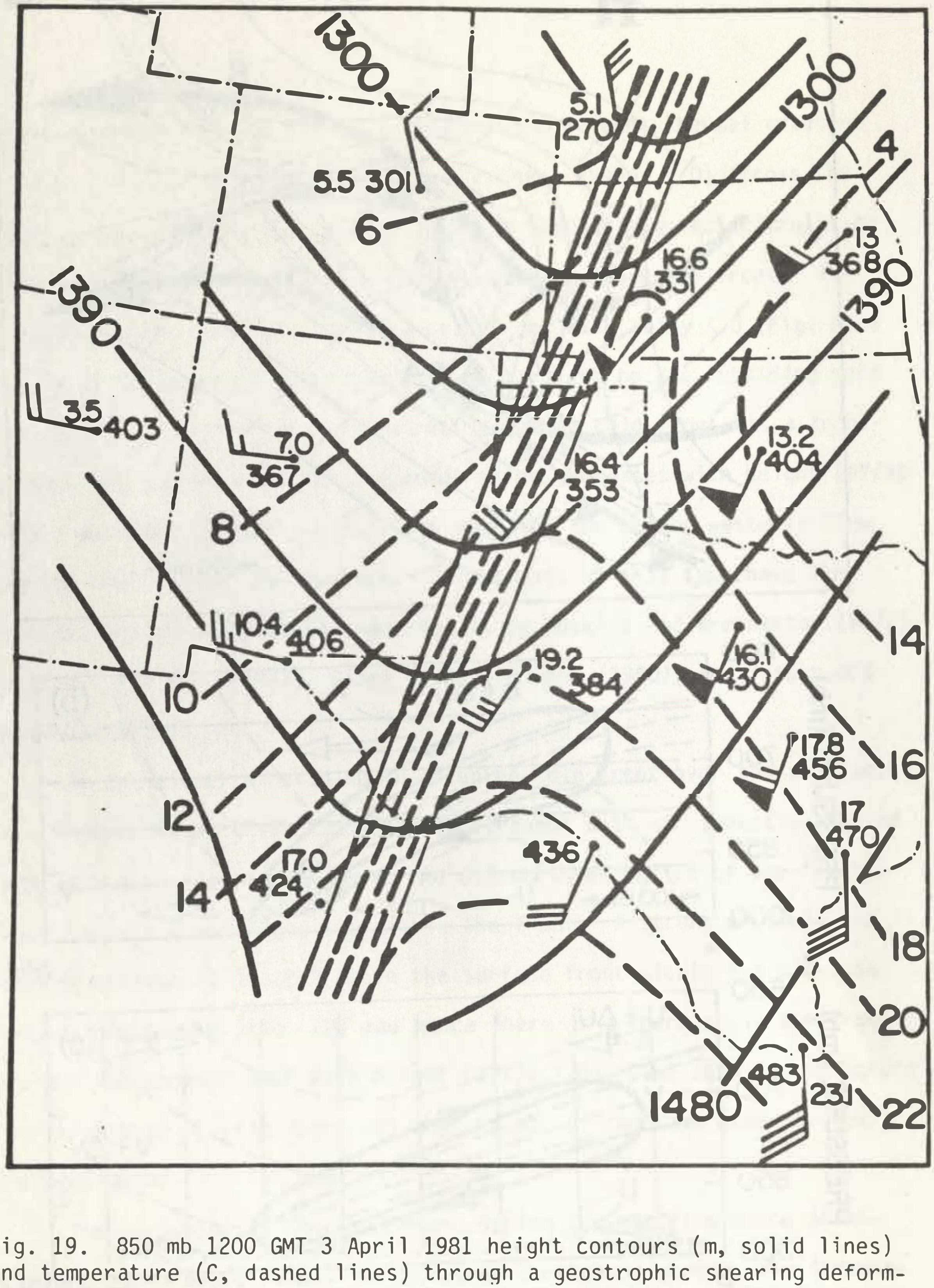

Fig. 19. 850 mb 1200 GMT 3 April 1981 height contours (m, solid lines) and temperature (C, dashed lines) through a geostrophic shearing deformation cold front. Frontal boundaries, thin solid lines. Wind flags and barbs (kts).

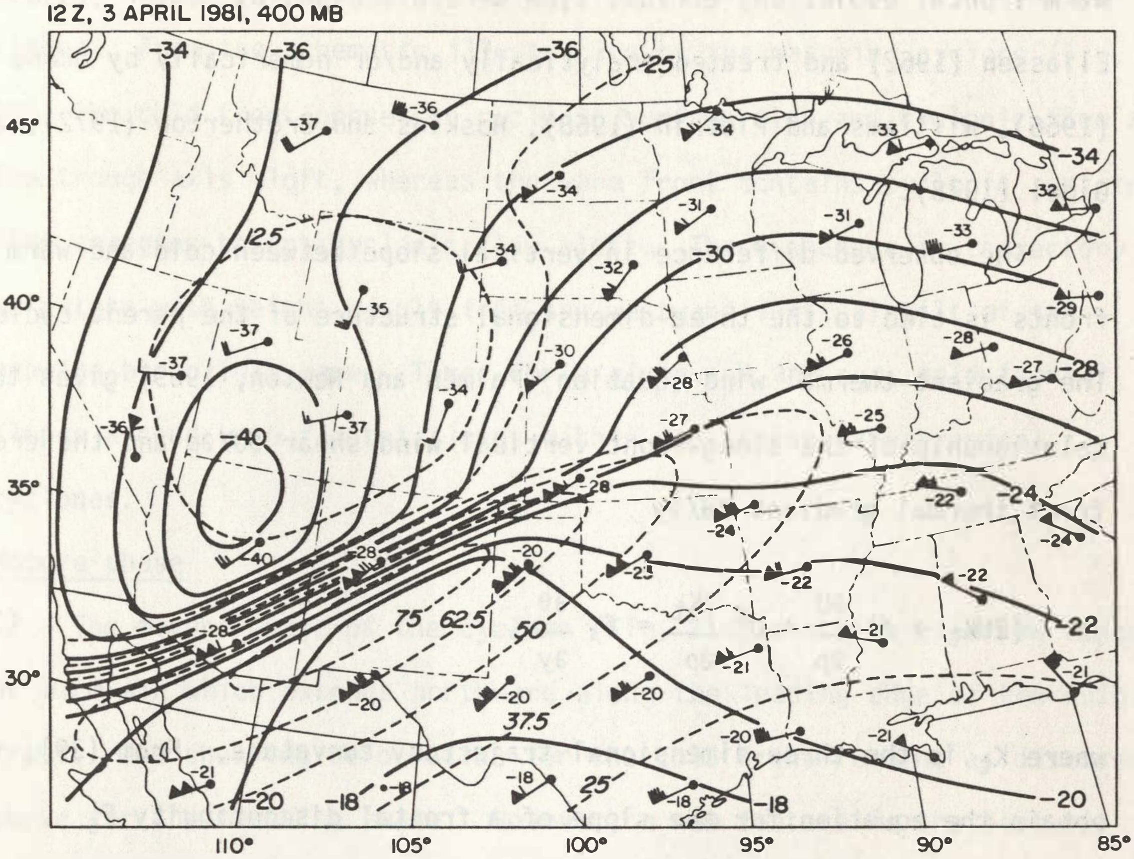

Fig. 20. 400 mb 1200 GMT 3 April 1981 wind speed (m s^{-1}, dashed lines) and temperature (C, solid lines). Wind vectors, flag = 25 m s^{-1}; barb = 5 m s^{-1}; half barb = 2.5 m s^{-1}.

stretching deformation ($\partial V/\partial y < 0$) across the frontal region forces a thermally direct secondary circulation about the warm front (Fig. 18c). Warm frontal evolutions of this type were discussed by Sawyer (1956) and Eliassen (1962) and treated analytically and/or numerically by Stone (1966), Williams and Plotkin (1968), Hoskins and Bretherton (1972), and Gidel (1978).

The observed difference in vertical slope between cold and warm fronts is tied to the three-dimensional structure of the parent cyclone. The gradient thermal wind equation (Palmén and Newton, 1969) gives the relationship of the along-front vertical wind shear $\partial U/\partial p$ and the cross-front thermal gradient $\partial\theta/\partial y$

$$(2UK_t + f)\frac{\partial U}{\partial p} + U^2\frac{\partial K_t}{\partial p} = f\gamma\frac{\partial\theta}{\partial y}, \tag{39}$$

where K_t is the three-dimensional trajectory curvature. From (39), we obtain the equation for the slope of a frontal discontinuity F_s

$$F_s = \gamma^{-1}\left\{\left(\frac{2UK_t}{f} + 1\right)\frac{\Delta_p U}{\Delta_p \theta} + \frac{U^2}{f}\frac{\Delta K_t}{\Delta_H \theta}\right\}, \tag{40}$$

where $\Delta_p U$ and $\Delta_p K_t$ are the vertical changes in U and K_t across the front, $\Delta_H\theta$ is horizontal difference in θ across the front, and $F_s = \Delta p/\Delta y$. For straight flow ($K_t = 0$, $\Delta_p K_t = 0$), the frontal slope is determined by the ratio $\Delta_p U/\Delta_H\theta$. Neglecting vertical changes in trajectory curvature, Palmén and Newton (1969) noted that fronts with cyclonic curvature ($K_t > 0$) have greater slope than those with anticyclonic curvature ($K_t < 0$) for given $\Delta_p U$ and $\Delta_H \theta$, but did not consider vertical changes in K_t as a modifying factor affecting frontal slopes. From the schematic illustration of the maturing cyclone (Fig. 18), the cold front possesses cyclonic surface flow and cyclonic flow at the trough axis aloft, whereas the warm front contains cyclonic surface flow changing to anticyclonic flow aloft. These changes in trajectory curvature with height result from the westward vertical tilt of the growing baroclinic wave. Thus, for a given $\Delta_p U$ and $\Delta_H \theta$, cold frontal slopes exceed warm frontal slopes within amplifying extratropical cyclones.

Mature phase

The mature phase of the cyclone (Fig. 21a) contains a narrow tongue of warm air which extends northward along the leading edge of the cold front. The shearing deformation for the cold front remains as discussed above for the maturing phase. However, a new feature is the eastwest thermal gradient ($\partial\theta/\partial x < 0$) to the east of the warm tongue axis (the baroclinic warm sector) which is associated with a low-level jet stream out in advance of the cold front. This thermal gradient within the cyclone warm sector is directed in the sense such that the near-surface southerly jet diminishes rapidly with height. The presence of low-level jets in advance of cold fronts was discussed by Means (1954), Newton (1958), Wexler (1961), Bonner (1963), and Bonner and Paegle (1970). Uccellini (1980) stressed that these low-level wind systems are a partly a manifestation of the evolution of the parent cyclone and are not just

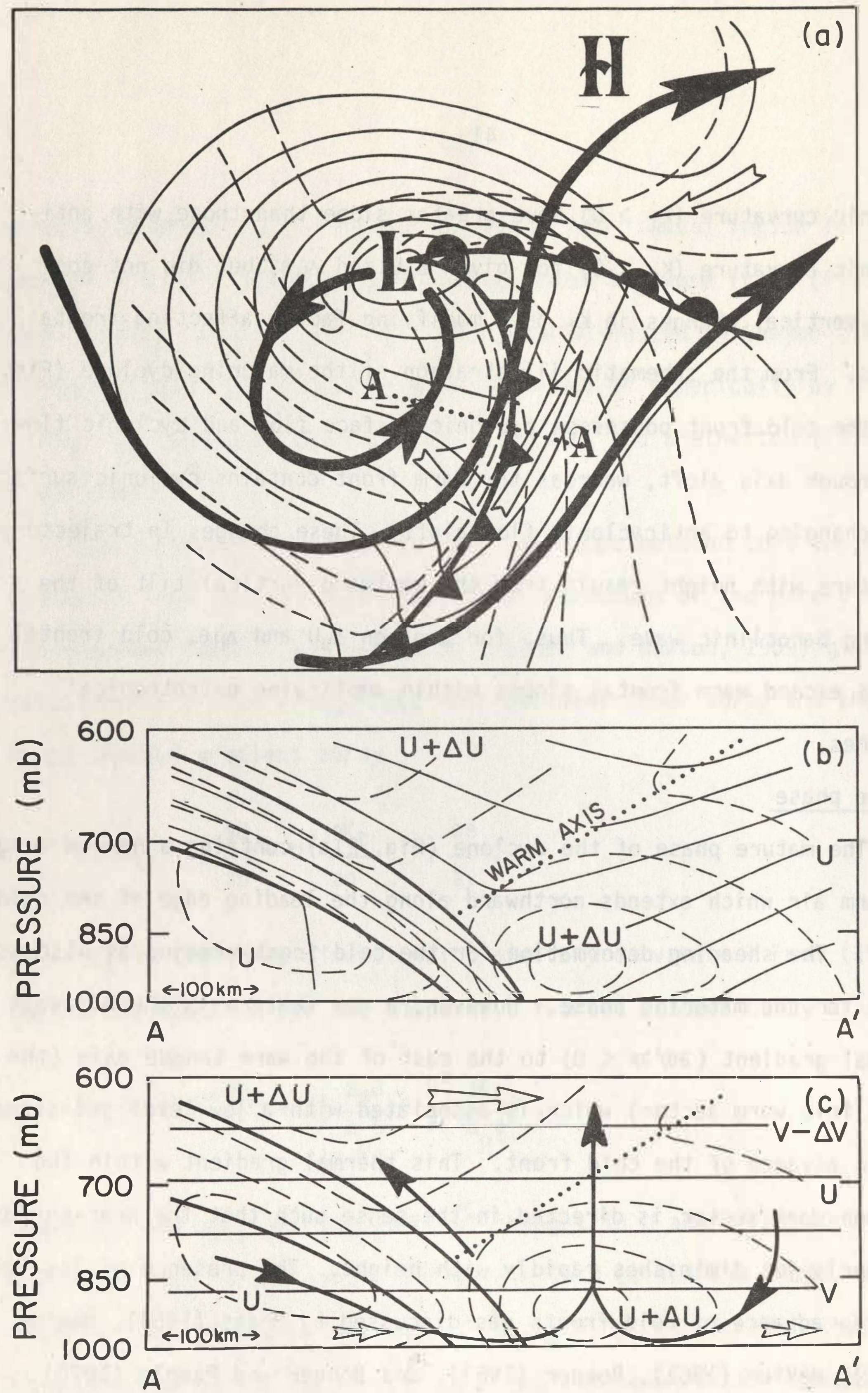

Fig. 21. (a) Same as Fig. 13(a), but for the mature cyclone. (b) Cross-section along the line AA' across the cold front and warm tongue of (a). Frontal boundaries, heavy solid lines, along front geostrophic wind U, dashed lines; potential temperature, thin solid lines; axis of thermal wave, dotted line. (c) Secondary circulation with ($\partial V/\partial p > 0$) for (b) with arrows and isopleths, same as Fig. 13(b).

the result of the boundary-layer nocturnal oscillations studied by Blackadar (1957). Djuric and Damiani (1980) showed that the oscillation was most noticeable in the vicinity of these low-level jets. The warm tongue and low-level jet in advance of the surface cold front are also a distinct feature of the mature cyclone which develops from the Eady wave numerical simulations of Hoskins and West (1979) and Hoskins and Heckley (1981). The cross section through the cold front (Fig. 21b) shows the axis of the warm tongue sloping eastward with increasing height ahead of the front with the low-level jet beneath. The earliest description of the warm air leading the cold front aloft was derived from the serial ascents within selected European cyclones (Bjerknes and Palmén, 1937). Hoskins and Heckley (1981) postulated that a fundamental difference between warm and cold fronts is the forward tilt of the temperature wave with height for cold fronts and the backward tilt for warm fronts. The vertical tilt of the temperature wave is a necessary feature of the amplifying baroclinic wave.

The cross section of the along- and cross-front geostrophic velocity components for the cold front/low-level jet structure of Fig. 21a,b is shown in Fig. 21c. The eastward-sloping temperature wave and associated low-level jet creates additional shearing deformation circulation forcing in advance of the cold front. The combined frontal/low-level jet forcing drives a secondary circulation in which the surface ageostrophic flow is directed toward the front from both the warm and cold sides (an enhancing mechanism for the scale contraction of cold fronts) and the frontal ascent is directed vertically at the leading edge of the front. This circulation is conducive to the development of narrow deep cloud systems which are characteristic of mature cold fronts. For the case in which the circulation forcing is dominated by the deformations of a low-level jet in advance of the cold front, the ascending branch of the low-level jet circulation precedes the cold front and the associated cloud and precipitation systems are called "prefrontal."

5. Coupled Upper- and Lower-Tropospheric Geostrophic Deformations

In the preceding discussions, we have treated separately the secondary circulations forced by geostrophic deformations within the middle (upper fronts) and lower (surface fronts) troposphere. There are, however, instances when upper- and lower-tropospheric forcings act simultaneously within the same region, and depending upon their vertical orientation produce significantly different secondary circulation regimes. To illustrate this point, consider the vertical alignment of the exit region of an upper-level jet front with a surface cold front and low-level jet at its leading edge when (1) the upper-jet exit is displaced to the west of the surface front, and (2) the upper-jet exit is displaced to the east of the surface front.

When a shearing deformation cold front and low-level jet (Fig. 22a) is situated in advance of the geostrophic stretching deformation (difluence) of an upper-level jet exit, the relative positions of the upper- and lower tropospheric geostrophic deformations, shown in Fig. 22a, forces a secondary circulation (Fig. 22b) which possesses predominantly lateral displacements. The thermally indirect circulation in the upper-jet exit overlies the direct circulation of the surface front and low-level jet, which suppresses deep ascent at the leading edge of the surface front through (1) mid-troposphere divergence where the descending branch of the upper circulation impinges upon the shallow ascent at the surface front, and (2) the convectively stable stratification of the upper front acts to inhibit the vertical development of deep convection.

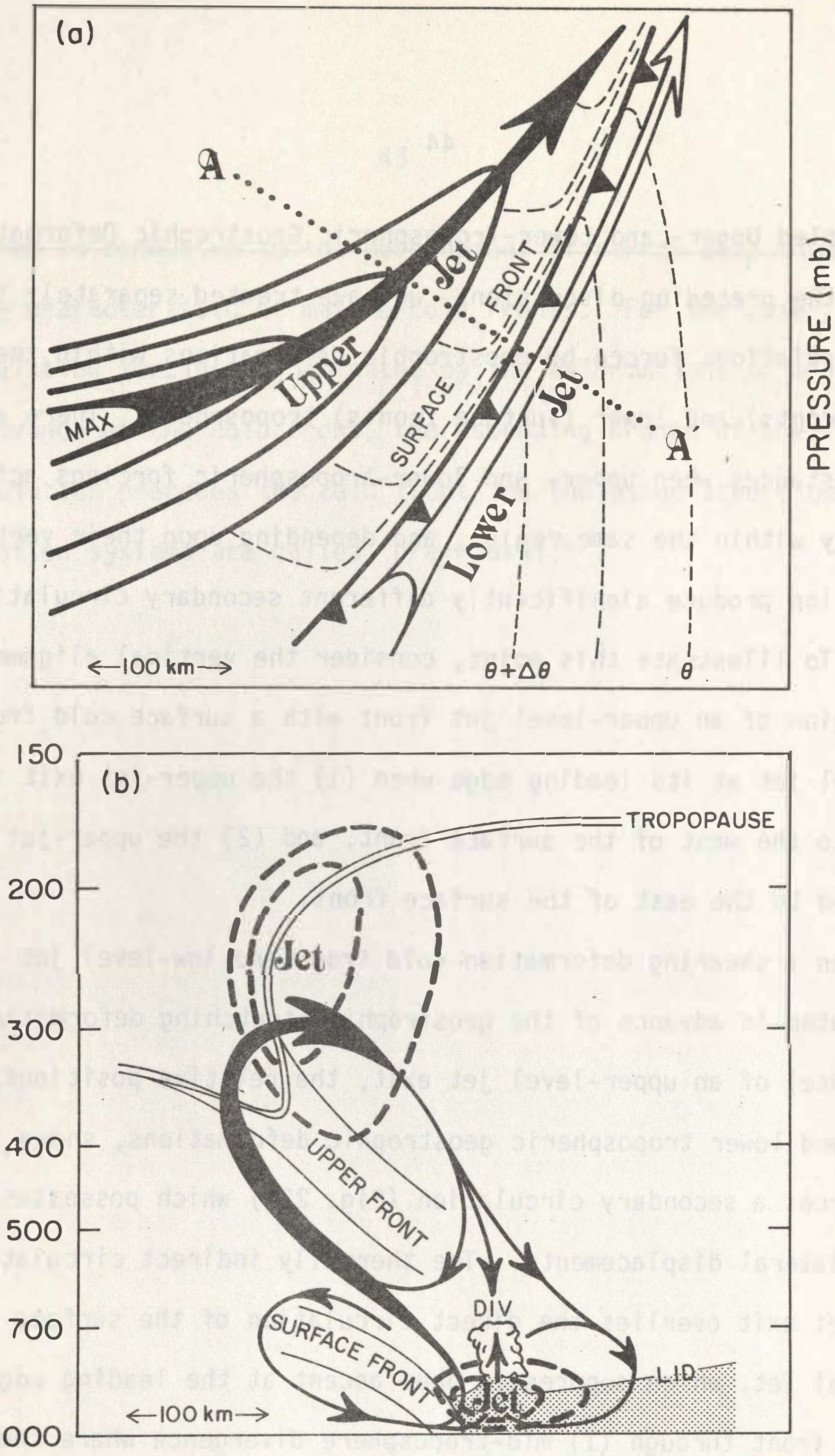

Fig. 22. Vertically uncoupled upper- and lower-tropospheric jet-front systems and their associated secondary circulations. (a) Upper jet-front exit region displaced to the west of a surface front and low-level jet. Upper jet (isotachs, heavy solid lines), upper-jet axis, solid arrow; lower jet axis, open arrow; surface potential temperature, thin dashed line; line AA', projection for cross section. (b) Cross section along the line AA' of (a). Upper and lower jet isotachs, heavy dashed line; potential vorticity tropopause, double thin lines; upper- and lower-level frontal surfaces, thin solid lines; moist layer, stippled area, streamlines with heavy arrows; forced secondary circulation.

As the upper-level jet moves eastward, it eventually overlies the surface front and lower-level jet. This pattern of intersecting upper- and lower-level jet streams (Fig. 23a) has been shown by Beebe and Bates (1955), Newton (1963), and Uccellini and Johnson (1979) to be a classical configuration for triggering the release of convective and potential instability. The vertical cross section through the intersecting jets (Fig. 23b) shows that the upper and lower circulations are vertically aligned, producing a deep narrow plume of ascending motion near the leading edge of the surface front. The ascent is located within a layer of convective instability as the differential motion between the upper and lower fronts results in a substantial destabilization of the thermal lapse rate. The destabilization aloft coupled with the decrease in moisture with height above the low-level jet are the thermodynamic components of the potential instability which is released by deep mesoconvection. The dynamical "trigger" for this release is the vertical alignment of upper- and lower-level geostrophic deformations (Fig. 23a) which "uncoils" the serpentine circulation of the previously non-aligned forcings.

In the above discussion of surface fronts within the developing extratropical cyclone, we have attempted to illustrate the dependence of the frontal secondary circulations upon the space- and time-variant geostrophic deformations. Let us next treat some of the not-so-classical frontal phenomena.

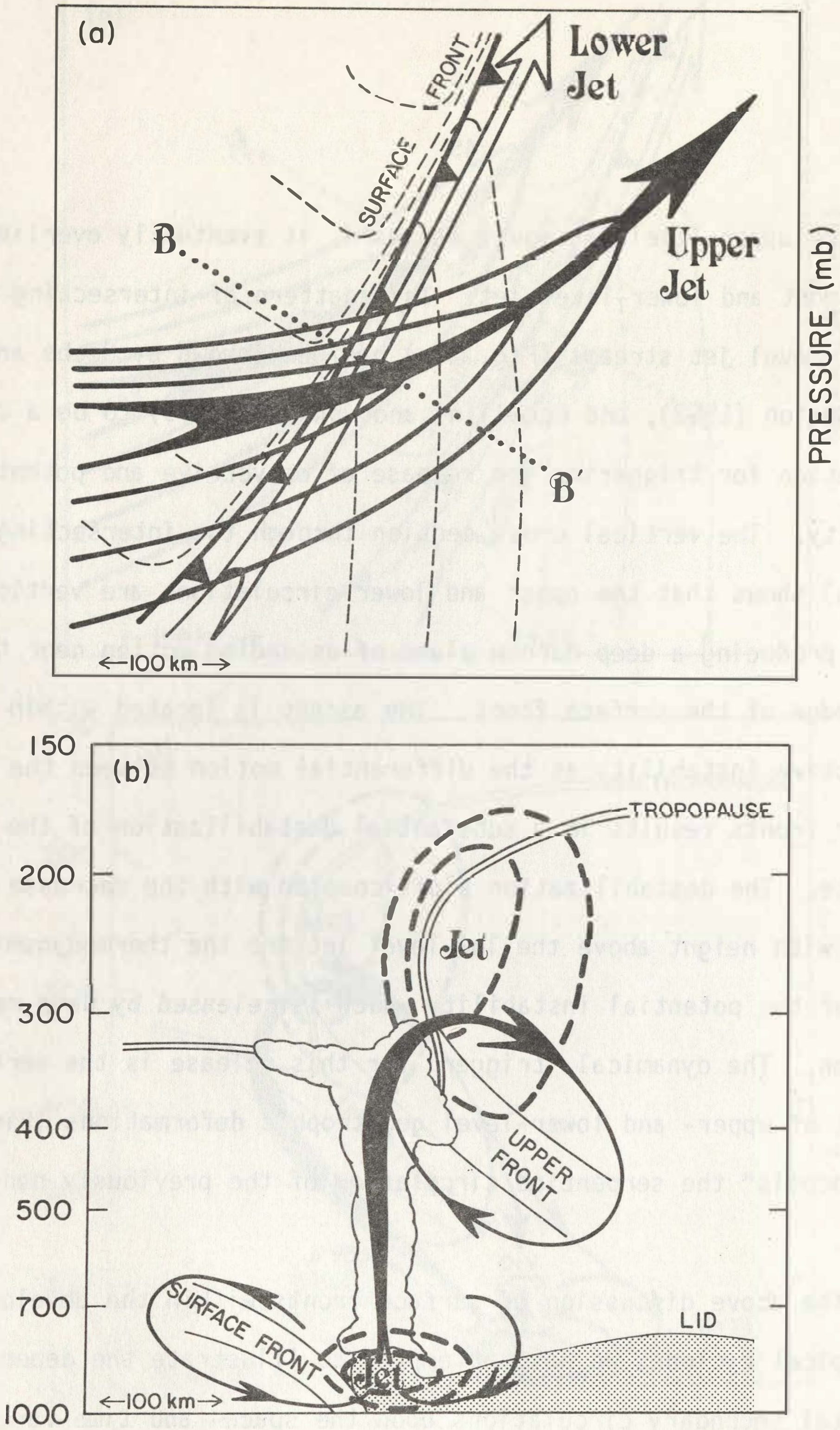

Fig. 23. Vertically coupled upper- and lower-tropospheric jet front systems and their associated secondary circulations. (a) Upper jet-front exit situated above the surface front and low-level jet. Line BB', projection for (b). (b) Cross section along the line BB' of (a). Isopleths, arrows, and stippling same as Fig. 3.1.22.

6. Dryline Fronts

Because of its unique combination of topography and climatic variations, the Great Plains of the United States is a region conducive to the formation of drylines and associated potential instability. These climatic and topographic variations range from the moist coastal plains of southern Texas to the semi-arid and desert plateaus of New Mexico and Colorado. Drylines appear as horizontal discontinuities in moisture which are confined to the lowest 1 to 3 km above the earth's surface. These discontinuities tend to form at the confluence of moist air flowing northward from the Gulf of Mexico and the much drier southwesterly flow which descends from the elevated desert plateau. The junction of these two air currents along the sloping topography gives the surface position of the dryline. In the extreme, dryline moisture discontinuities may occur over horizontal distances of 1 km with dew-point temperature gradients exceeding 5 K km^{-1} (Schaefer, 1974b). The vertical extent of the moist flow to the east of drylines is confined by a pronounced temperature inversion, often referred to as the "capping" inversion or lid. The inversion inhibits the development of convective cloud systems while allowing the progressive buildup of high wet-bulb potential temperatures beneath in the vicinity of the dryline (Fulks, 1951; Carlson and Ludlam, 1968).[1]

---

[1] This process contributes to an increase of the temperature achievable upon condensation of air parcels ascending from the lower moist layer, and thus to the development of potential instability in the lower- to middle-troposphere as a whole. It has been described as an ingredient that commonly precedes outbreaks of severe convection over the southern Great Plains (Fawbush and Miller, 1954; Newton, 1963), although actual release of the potential instability depends upon other dynamical processes.

Equations (18) and (19) contain geostrophic, ageostrophic, and turbulent processes which force the horizontal and vertical development of dryline-capping inversion moisture gradients. Expansion of (18) shows that horizontal gradients in moisture (∂q/∂y) are forced by geostrophic stretching and shearing deformations (1), horizontal divergence and vertical tilting by the secondary (ageostrophic motions) (2), and horizontal gradients in the vertical flux divergence of moisture (3)

$$\frac{d}{dt}\left(\frac{\partial q}{\partial y}\right) = \underbrace{\left(\frac{\partial U}{\partial x}\frac{\partial q}{\partial y} - \frac{\partial U}{\partial y}\frac{\partial q}{\partial x}\right)}_{(1)} + \underbrace{\left(\frac{\partial v_a}{\partial y}\frac{\partial q}{\partial y} + \frac{\partial \omega}{\partial y}\frac{\partial q}{\partial p}\right)}_{(2)}$$

$$\underbrace{- \frac{\partial}{\partial y}\left(\frac{\partial \overline{q'\omega'}}{\partial p}\right)}_{(3)} . \tag{41}$$

Expansion of (19) shows that vertical gradients in moisture (∂q/∂p) evolve in response to vertical shear of the geostrophic motions (1), horizontal divergence and vertical shear of the horizontal ageostrophic motion (2), and vertical gradients in the vertical flux divergence of moisture (3)

$$\frac{d}{dt}\left(\frac{\partial q}{\partial p}\right) = \underbrace{-\left(\frac{\partial U}{\partial p}\frac{\partial q}{\partial x} + \frac{\partial V}{\partial p}\frac{\partial q}{\partial y}\right)}_{(1)} + \underbrace{\left(\frac{\partial v_a}{\partial y}\frac{\partial q}{\partial p} - \frac{\partial v_a}{\partial p}\frac{\partial q}{\partial y}\right)}_{(2)}$$

$$\underbrace{- \frac{\partial}{\partial p}\left(\frac{\partial \overline{q'\omega'}}{\partial p}\right)}_{(3)} . \tag{42}$$

Figure 24 presents the synoptic soundings and vertical cross-section analysis illustrating the intersection of a capping inversion with the sloping topography over the Texas Panhandle. The analysis shows the decreasing depth of the moist layer as the topography slopes upward to the west to intersect the inversion. The rapid decrease of water vapor mixing ratio across the lid plus the near-adiabatic lapse rate above the inversion illustrate convective and conditional instabilities, respectively, which together give rise to potential instability. Figure 25 shows the plan view of the intersection of the capping inversion of Fig. 24 with the earth's surface. The intersection forms the surface dryline separating the dry desert flow from the moist air from the Gulf of Mexico.

The role of differential surface heating and the turbulent vertical fluxes of heat and momentum associated with dryline intensification has been discussed and numerically modeled by Schaefer (1974a). It was noted that because of the west-east variation in depth of the surface moist layer across the sloping terrain, the western portion of a capping inversion is easily destroyed where the moist layer is shallow. To the east, where the moist layer is deeper, additional surface heating and turbulent mixing are required to eliminate the inversion. The observed scale contraction of drylines occurs across the boundary between strong and weak vertical mixing [i.e., where term 3 of (41) is large]. Figure 26 illustrates the vertical structure of an Oklahoma dryline which has undergone a scale contraction down to less than 1 km between the moist and dry flow regimes. This analysis, after L. D. Sanders (U.S. Weather Bureau, 1961),

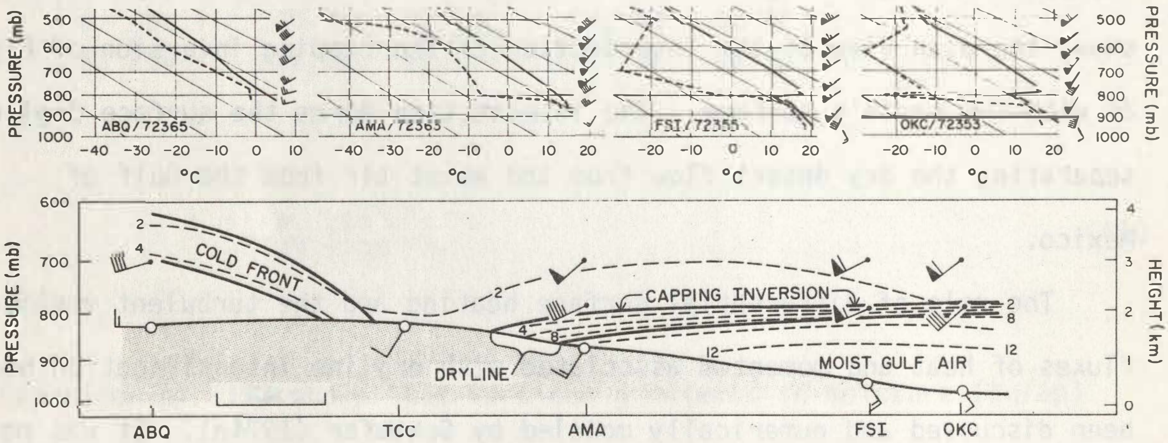

Fig. 24. Cross section through a capping inversion-dryline along the line BB' of Fig. 3.1.25 at 1200 GMT 3 April 1981. (a) Rawinsonde observations from Albuquerque, New Mexico (ABQ/72365), Amarillo, Texas (AMA/72363), Fort Sill, Oklahoma (FSI/72355) and Oklahoma City, Oklahoma (OKC/72353). Temperature (C, solid line); dewpoint (C, dashed line); wind velocity vectors (flag = 50 kts, barb = 10 kts, half barb = 5 kts); dry adiabats (C, sloping lines). (b) Water vapor mixing ratio (g Kg^{-1}, dashed lines); boundaries of capping inversion and cold front, heavy solid lines; wind vectors, same as (a); ground topography, stippled.

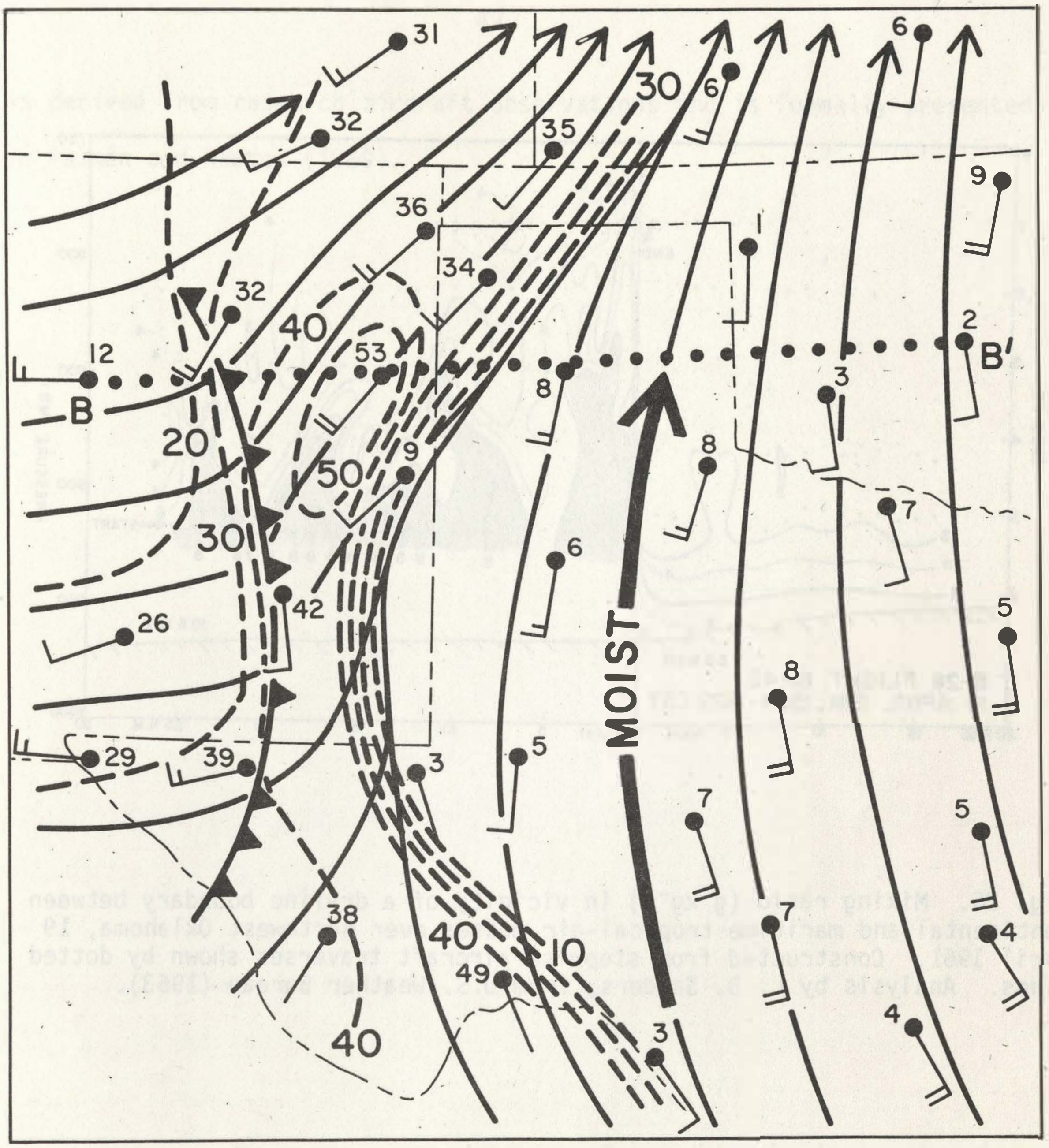

Fig. 25. Surface dewpoint temperature depression (F, dashed lines) and streamlines at 1200 GMT 3 April 1981. Cross-section projection of Fig. 24, dotted line BB'; cold front, spiked solid lines; Gulf of Mexico moist flow, heavy solid arrow.

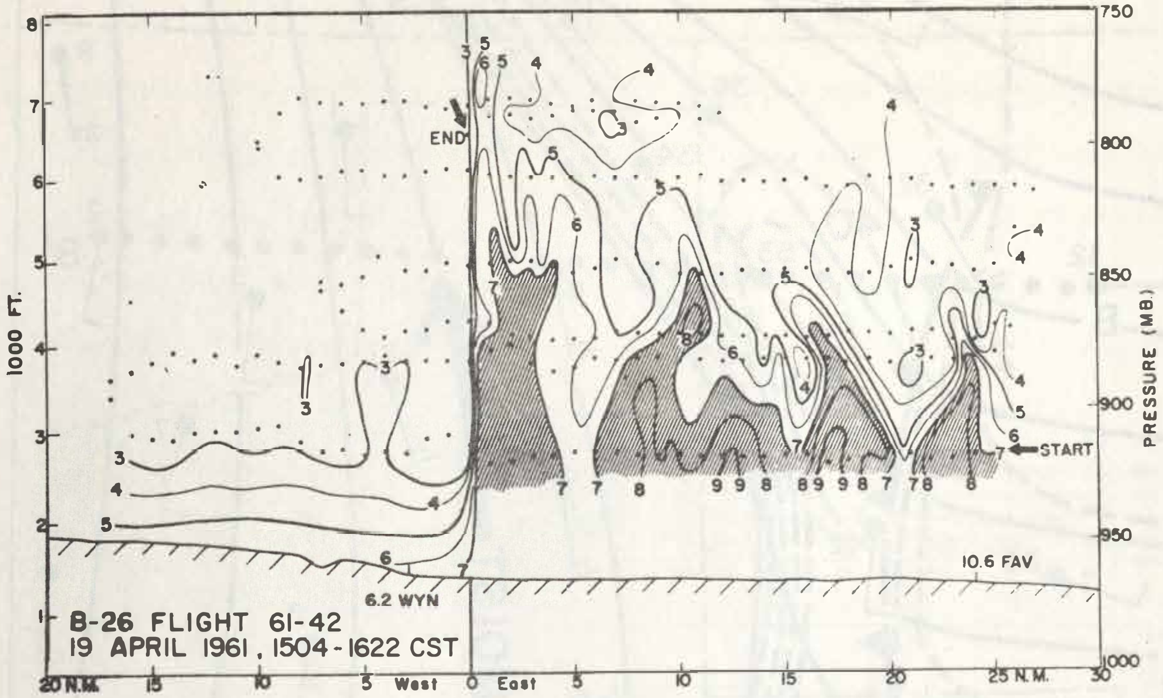

Fig. 26. Mixing ratio (g kg^{-1}) in vicinity of a dryline boundary between continental and maritime tropical-air masses over northwest Oklahoma, 19 April 1961. Constructed from stepwise aircraft traverses shown by dotted lines. Analysis by L. D. Sanders, from U.S. Weather Bureau (1963).

is derived from research aircraft observations and is formally presented in Palmén and Newton (1969).

7. Orographic-Frontal Interactions

Interactions between frontal and orographic flows produce mesoscale structures which affect weather events to the lee of the Rocky Mountains. One such example involves the interaction between cold air outbreaks which propagate southward in the lee and impinge upon the elevated topography which is under the action of downslope flow. The juxtaposition of cooler easterly flow with warm westerly downslope Chinook flow produces extremely sharp lee frontal discontinuities. Depending upon the relative strengths of the two air flows, dramatic differences can occur in the resulting mesoscale circulations and associated cloud and precipitation systems.

An example of frontal-lee flow interaction was documented by the Prototype Regional Observing and Forecasting Service (PROFS) experimental mesometeorological network situated in the vicinity of Denver, Colorado. At 1000 GMT 3 December 1981 (Fig. 27a), the PROFS network indicated westerly and northwesterly surface flow down the mountain slope with the associated adiabatically warmed air in the lee. During the early morning hours, surface temperatures approaching 50 F were found along a north-south axis near the 6,000 ft elevation. The northeastern sector of the network indicated the entry of colder (< 35 F) air into the region associated with a southward propagating cold front. The temperature analysis for this and subsequent figures is performed only for those stations situated below the 6,000 ft level. At 1100 GMT (Fig. 27b), the cold upslope and warm downslope flows impinged along a north-south confluent asymptote and the scale contraction of the surface thermal gradient was

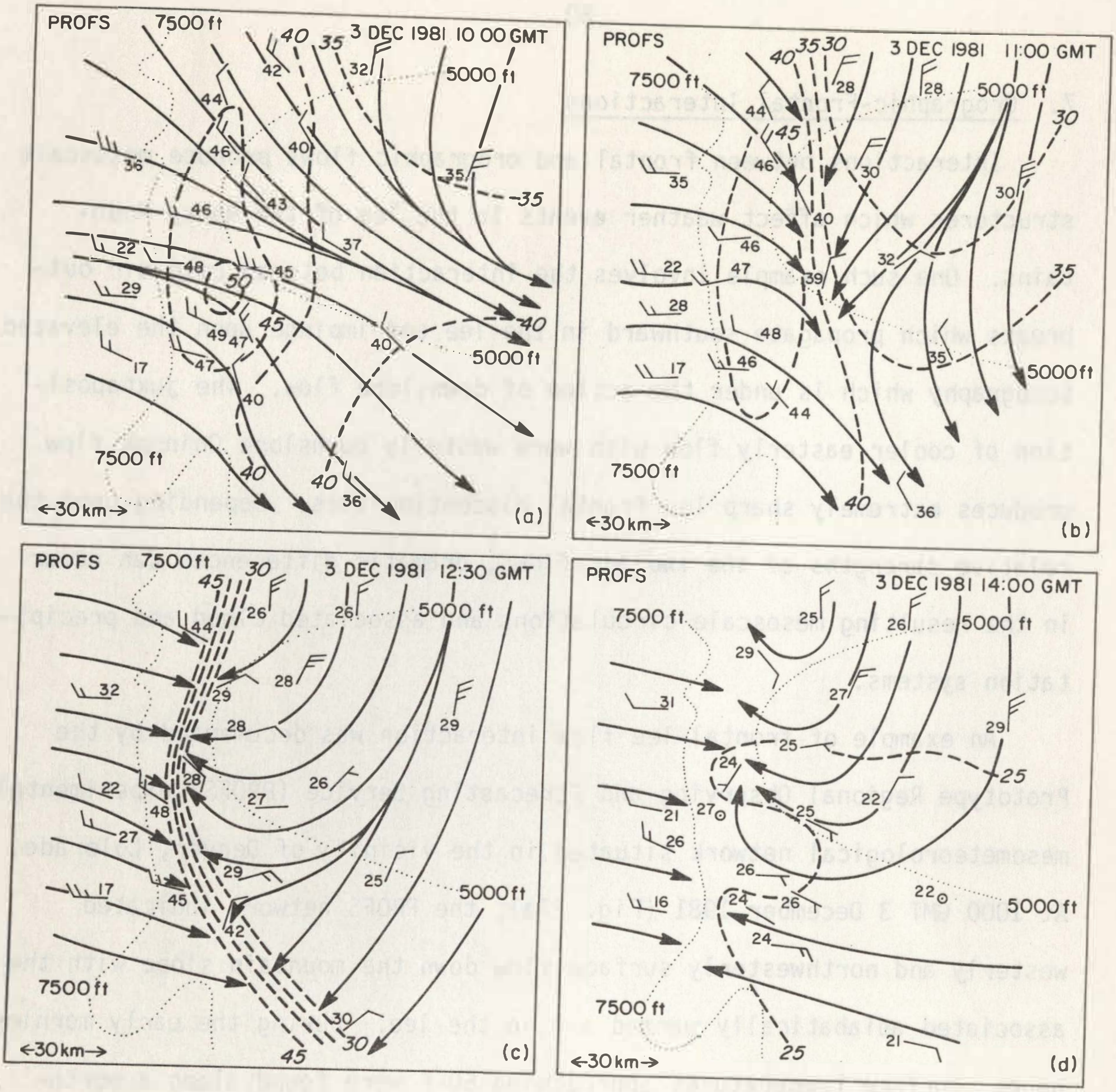

Fig. 27. Formation of a surface cold front to the lee of the Colorado Rockies as obtained from the Prototype Regional Observing and Forecast Service (PROFS) over northeastern Colorado. Surface temperature (°F, dashed lines), and surface wind streamlines, solid lines; 5,000 and 7,500 ft surface elevation, dotted lines.

well under way. By 1230 GMT (Fig. 27c), an intense surface front extended down the lee containing thermal gradients of 30 F in 15 km across the front. In the final phase of the evolution (Fig. 27d), the surface front continues its westerly propagation against the downslope flow and rides up the topography to above the 6,000 ft elevation, and all lee observing stations are within the cold air. Lilly (1981) discussed the interaction of mountain upslope flows with upper-level cross-mountain westerly flows. His results suggest the importance of turbulence in the shear layer between the up- and downslope flows in entraining cold air up the slope and up into the reverse westerly flow. The greater the entrainment, the more intense the resulting upslope motion.

Another example of orographic-frontal interactions is the dryline fronts which form north of Texas-Oklahoma in response to mountain downslope flow to the lee of the Rockies. During late spring and summer, weak synoptic waves pass across the Colorado and Wyoming Divide initiating dry downslope winds which impinge upon moist southerly Gulf flow on the westerly side of the quasistationary anticyclone over the central and eastern United States. Sharp dryline fronts form in the confluence and convergence of the westerly downslope flow with moist southern flow to the east of the lee. Once formed, the Lee Dryline Front (LDF) propagates eastward onto the Plains where mesoconvective systems form in response to the secondary circulations of the LDF combined with high low-level moisture and potential instability of the flow around the back side of the continental anticyclone.

An early study by Fujita (1958) composited surface observations, radar and research aircraft measurements to describe the formation and propagation of a lee dryline front over eastern Wyoming and western Nebraska on 11 June 1956. Figure 28 illustrates the evolution of the LDF over a 6 h interval. The sequence begins with LDF formation just east of Cheyenne, Wyoming (CYS), and culminates with the development of convection ahead of the lee-dryline. It is of interest to note that the spawning ground for midwestern Meso Convective Complexes (MCCs) is just east of the steep topography which characterizes the Rocky Mountain lee in Colorado and Wyoming (Cotton, 1982; Maddox, 1982). We suggest that the interaction of transient synoptic waves with steep mountains can produce frontal structures in the lee which occasionally provide the triggering mechanism for both linear- and complex-form mesoscale convective storm systems.

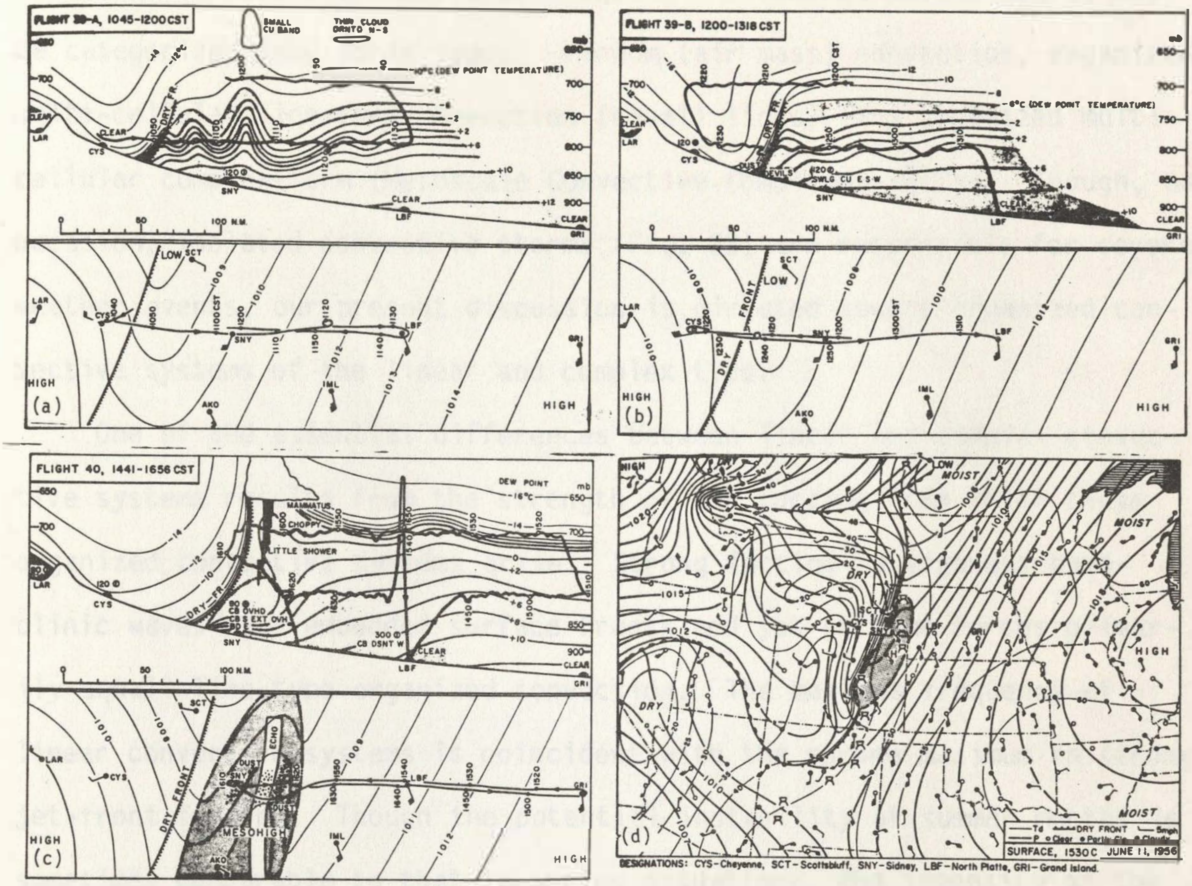

Fig. 28. Formation and progression of a lee dryline front east of Cheyenne, Wyoming (CYS), on 11 June 1956 (after Fujita, 1958). (a), (b) and (c), Cross-sections of dewpoint temperature (C), surface pressure (mb), wind vectors and research aircraft flight tracks. (d) pressure (mb) and dew-point (C) at 1530 CST.

8. Organized Mesoconvective Systems

The convective systems that frequent the central United States may be categorized into three types: random (air mass) convection, organized multi-cellular line-form convection (squall lines), and organized multi-cellular complex-form (Mesoscale Convective Complexes--MCCs). Though, on occasion, isolated convective storms (Fig. 29) are responsible for severe weather events, our present discussion is directed toward organized convective systems of the linear and complex type.

One of the essential differences between linear and complex convective systems results from the strength of the forcing from which these organized convective systems arise. Strong forcing by vigorous baroclinic waves with embedded surface fronts and jet streams forces primarily squall-line-type organized convection. The maximum frequency of linear convective systems is coincident with the spring maximum in strong jet-front forcing. Though the potential instability of summer months is sometimes comparable to that in spring situations, the intensity of the forcing is greatly reduced. It is during the summer months of weak tropospheric flow and weak forcing that MCCs become the dominant organized convective systems over the central United States. An example of the development of a Texas-Oklahoma squall line through strong frontal forcing is presented in section 3.1.7, Case study: 3-4 April 1981. The reader is referred to Newton (1950), Bergeron (1954), Newton and Fankhauser (1964), and Palmén and Newton (1969) for comprehensive discussions of squall-line convection.

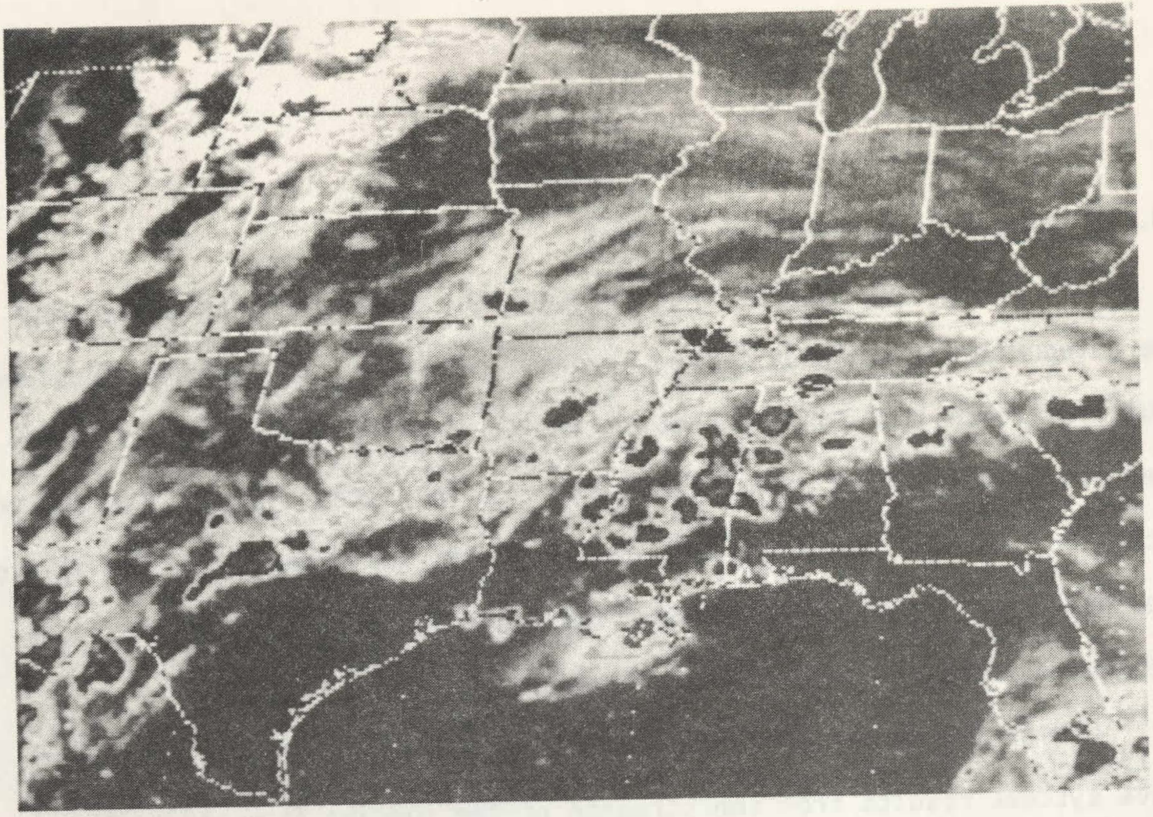

Fig. 29. Enhanced infrared satellite image at 2000 GMT 16 August 1981 illustrating disorganized airmass convection over the southern United States.

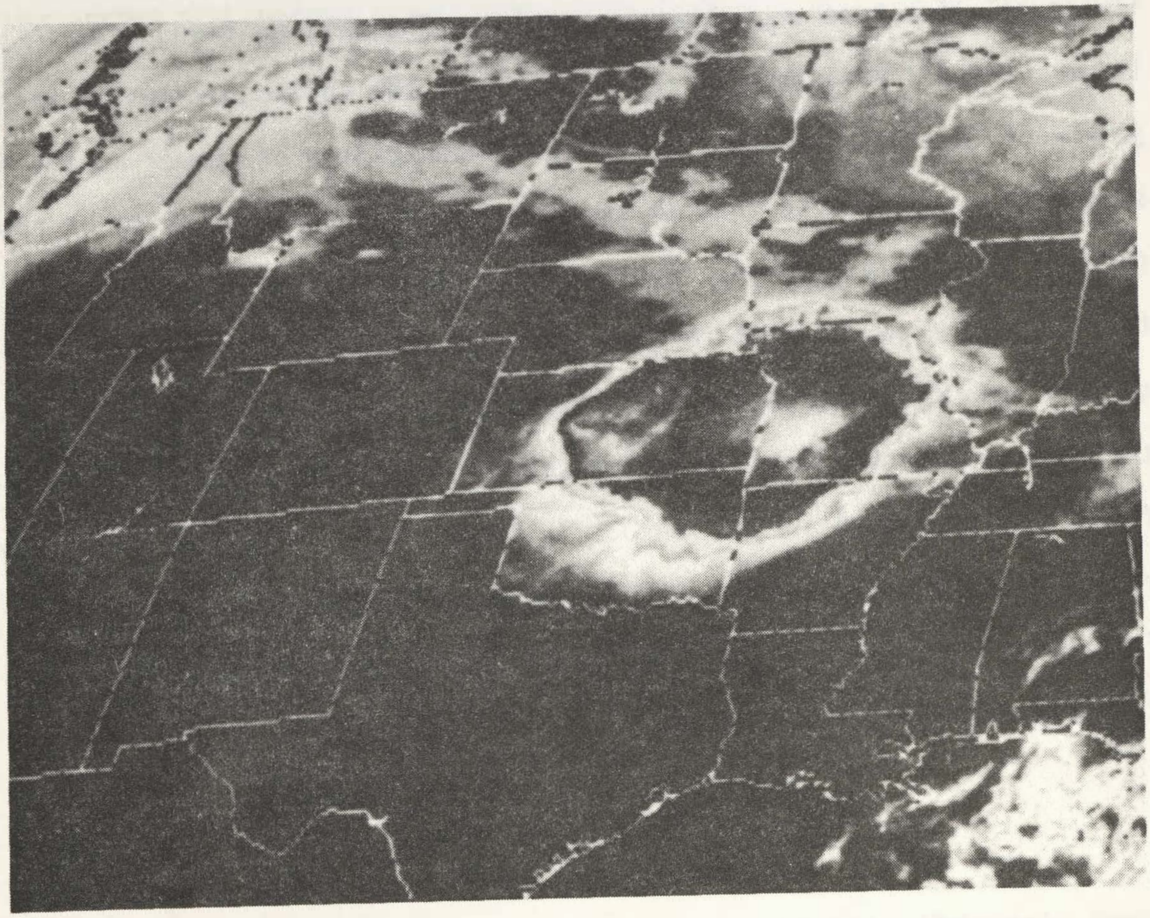

Fig. 30. Enhanced infrared satellite image showing a Mesoscale Convective Complex (MCC) over the central United States at 1500 GMT 22 June 1981 (after Maddox, 1982).

Mesoscale Convective Complexes (MCCs)

Complex-form, organized convection over the central United States was described by Maddox (1980, 1981) from satellite infrared (IR) cloud images. The cloud top IR images from these cloud complexes differed dramatically from isolated or squall-line convection in that the space and time scales over which MCCs maintain their organization approach the synoptic scale. Table 2 (after Maddox, 1980) summarizes the spatial and temporal characteristics of MCCs from the analysis of enhanced IR satellite imagery.

Table 2 **Mesoscale Convective Complex (MCC) (based upon analyses of enhanced IR satellite imagery).**

Physical Characteristics	
Size:	**A--Cloud shield with continuously low IR temperature $\le -32^\circ C$ must have an area $\ge 100\ 000\ km^2$** **B--Interior cold cloud region with temperature $\le -52^\circ C$ must have an area $\ge 50\ 000\ km^2$**
Initiate:	**Size definitions A and B are first satisfied**
Duration:	**Size definitions A and B must be met for a period ≥ 6 h**
Maximum extent:	**Contiguous cold cloud shield (IR temperature $\le -32^\circ C$) reaches maximum size**
Shape:	**Eccentricity (minor axis/major axis) ≥ 0.7 at time of maximum extent**
Terminate:	**Size definitions A and B no longer satisfied**

A classical example of an MCC over the central region (Maddox, 1982) is presented in Fig. 30. The enhanced IR imagery shows the high-level outflow from the convective cloud shield covering portions of the five states. The coldest IR temperatures at the top of the complex indicate the location of the highest convective elements. The National Weather Service radar summary at 1345 GMT 22 June 1981 (Fig. 31) shows the areal distribution of precipitating convective elements which are embedded within the complex. In this case, there is no evidence for linear organization of the convection and the scale of the precipitation approaches the scale of the IR cloud signature of the MCC.

By combining ten examples into a single conceptual model, Maddox (1982) established the conditions associated with the initiation, maintenance, and decay of midwestern United States MCCs. Figure 32 shows the genesis phase of MCC evolution. The surface composite (Fig. 32a) shows the east-west-oriented surface front with weak frontal convergence over the genesis region. The 200 mb flow (32b) contains a weak (32 m s^{-1}) jet streak to the northwest of the genesis region. MCC formation takes place within a region of preexisting weak frontal forcing.

The composite analysis for the fully developed MCC is shown in Fig. 33. At this stage, the MCC has propagated eastward along the surface front (Fig. 33a) and is characterized by weak divergence as a result of surface outflow from convective downdrafts. The 200 mb flow (Fig. 33b) shows a dramatic increase in the speed of the anticyclonically curved jet streak, and divergence is found at the upper levels of the complex.

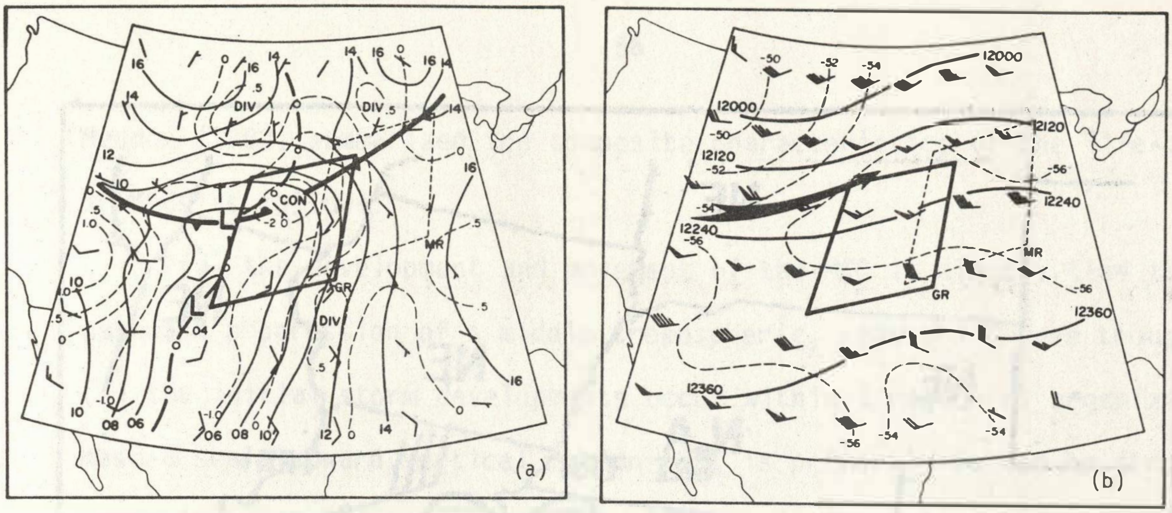

Fig. 32. (a) Composite analysis of surface features prior to MCC development. Surface winds are plotted at every other grid point (full barb = 5 m s^{-1}). Isobars of surface pressure (mb, solid lines), surface velocity divergence (10^{-5} s^{-1}, dashed lines). (b) Composite analysis of the 200 mb height field (m, solid lines) and velocity divergence (10^{-5} s^{-1}, dashed lines) prior to MCC development. Jet stream axis, heavy arrow; wind vectors, flag = 25 m s^{-1} (after Maddox, 1982).

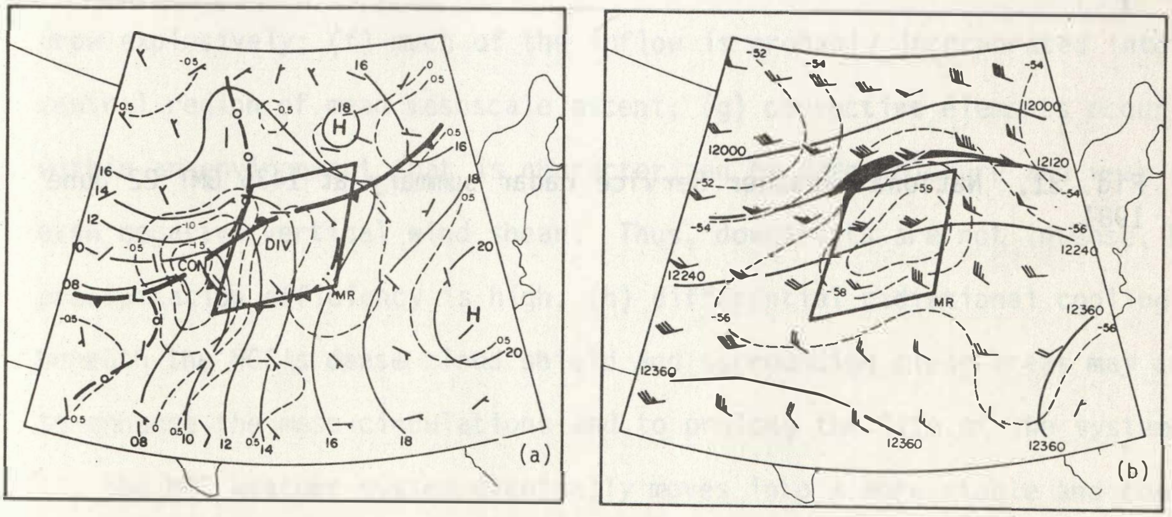

Fig. 33. Same as Fig. 20 but for the mature MCC.

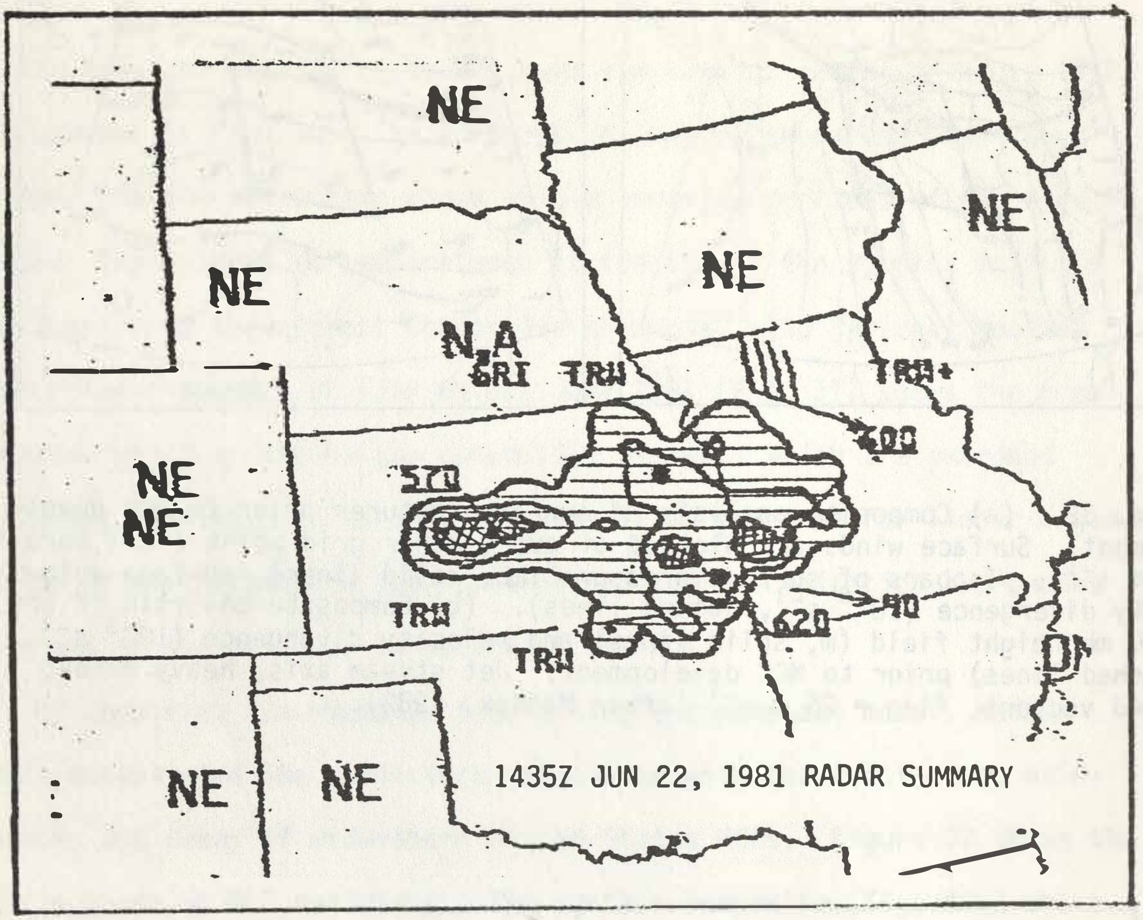

Fig. 31. National Weather Service radar summary at 1435 GMT 22 June 1981.

Maddox (1982) summarized the composite characteristics of the life-cycle of MCCs as follows:

"(a) the development and movement of the MCC is closely tied to the eastward progression of a middle tropospheric, weak short-wave trough; (b) the initial storm developments occur within a region of organized meso-α scale upward vertical motion that is primarily forced by strong lower-tropospheric warm advection; (c) the large-scale setting provides a conditionally unstable thermodynamic structure over a large region ahead of, and to the right of, the advancing short wave; (d) the nocturnal increase in speed and significant veering of the low-level winds enhance both the warm advection and influx of moist unstable air, while radiative cooling decouples the entire system from the near-surface layer; (e) individual storms, clusters of storms, and features of their nearby environment interact synergistically, allowing the convective system to grow explosively; (f) much of the inflow is probably incorporated into a central region of mean mesoscale ascent; (g) convective elements occur within an environment that is characterized by deep moisture and weak or even negative vertical wind shear. Thus, downdrafts are not intense, but precipitation efficiency is high; (h) differential radiational cooling beneath the MCC's dense cloud shield and surrounding clear areas may act to enhance the meso-circulations and to prolong the life of the system; (i) the MCC weather system eventually moves into a more stable and convectively less favorable environment, thus initiating its demise; and (j) as potentially cool air flows into the system, a deep meso-downdraft develops and the MCC decays."

9. Case Study: 3-4 April 1981

A severe weather event which occurred over the southwestern portion of the central United States on 3-4 April 1981 was selected to illustrate the mutual dependence of the macro-β through micro-γ phenomena and to show how many of the phenomena discussed so far interact as part of a complete atmospheric system. During the early morning hours of 3 April 1981, the synoptic flow over the western United States was dominated by a large-amplitude wave with its trough axis extending from Idaho to Arizona. The 1200 GMT 3 April rawinsonde observations over the southwest United States and northern Mexico revealed an 80 m s^{-1} jet streak which was propagating through the wave and was located in the southwesterly flow in advance of the trough axis. A well-developed mid-tropospheric front beneath the jet (Fig. 20) had its maximum horizontal thermal gradient and wind shear concentrated over New Mexico. The exit region of the jet (Fig. 20) is similar to the schematic of Fig. 6a, as the solenoids formed by the temperature and speed isopleth intersections give evidence for a thermally indirect circulation forcing in the exit. In the lower troposphere, a low-level (surface) front (Fig. 19) was oriented at a large angle to the upper jet and, as described in section 3, contained a shearing deformation forcing for a thermally direct secondary circulation about the front. The 850 mb wind vectors (Fig. 19) showed evidence for a low-level southerly jet stream to the east of the leading edge of the front.

The 1200 GMT surface observations (Fig. 25) showed the surface front in the lee of the New Mexico mountains during its eastward progression toward the moist southerly flow from the Gulf of Mexico. A narrow tongue of dry air was sandwiched between the advancing front and the moist air over central and east Texas. A marked dryline front had formed between the dry southwesterly pre-cold frontal flow and the moist Gulf flow where the western extension of the moist layer and capping inversion intersected the sloping topography. The cross-section analysis of water vapor mixing ratio (Fig. 24b) at 1200 GMT shows the advancing cold front between Albuquerque (ABQ) and Tucumcari (TCC), New Mexico, and the capping inversion which confined the 12 g kg^{-1} moist Gulf air to the surface boundary layer. The potential temperature gradient across the cold front was 7 K, with θ ranging from 293 to 300 K between the trailing and leading surfaces. Surface mixing ratios between the cold front and dryline front were less than 3 g kg^{-1}.

By 1700 GMT (Fig. 34), the front had advanced into central Texas and merged with the moisture gradient of the dryline forming a pronounced surface confluent asymptote between the westerly flow behind and the southerly flow ahead of the cold Front-Dryline Merger (FDM). Between 1630 and 1745 GMT, the NCAR Sabreliner research aircraft measured the wind velocity, potential temperature, mixing ratio, and turbulence along the line AA' of Fig. 34. The aircraft measurements, surface observations, and 1200 GMT 3 April upper-air sounding were analyzed in cross section (Fig. 35) through the FDM with space-time adjustment to 1700 GMT 3 April. The cross section shows that the 7 K potential temperature differential across the front at 1200 GMT as contained in the soundings of Fig. 24 was diminished by surface heating and boundary-layer heat fluxes such that by 1700 GMT the FDM appeared as a moisture gradient and a wind shift from west to southwest. The FDM was a virtual temperature front whose mass-momentum balance was related to virtual potential temperature gradients rather than the potential temperature gradients of classical frontal structures. The dry southwesterly flow that extended upward from the surface between the cold front and dryline at 1200 GMT (Fig. 24b) was occluded aloft in the merger process. Evidence for the sense of the mass circulation about the FDM (similar to that postulated in Fig. 18) is found in the vertical deformation of the mixing ratio isopleths in Fig. 35. Low mixing ratios from aloft were drawn down the trailing edge of the FDM with the moist Gulf ratios being lifted at the leading edge. At this stage of the mesoscale evolution, the 840 and 800 mb flight legs of the Sabreliner encountered a narrow line of non-precipitating cumulus congestus within the elevated moist region in advance of the FDM. The uppermost flight leg at 715 mb was made entirely within cloud-free air. The visible satellite imagery (Fig. 36) shows the "rope cloud" signature of this narrow cumulus congestus line. Verification of the non-precipitating character of the system is found in the echo-free WSR-57 radar return over the area of the FDM (Fig. 37a).

The analyses and observations described above illustrate the precursors to the onset of a severe mesoconvective activity in addition to the development of surface boundary-layer processes that produced 50 kt surface winds and a duststorm to the west of the severe convection. The mesoconvective activity developed between 1735 and 1835 GMT, beginning at the northern portion of the FDM. The radar return at 1835 GMT (Fig. 37b) revealed that a full-blown 46,000 ft mesoconvective system with embedded

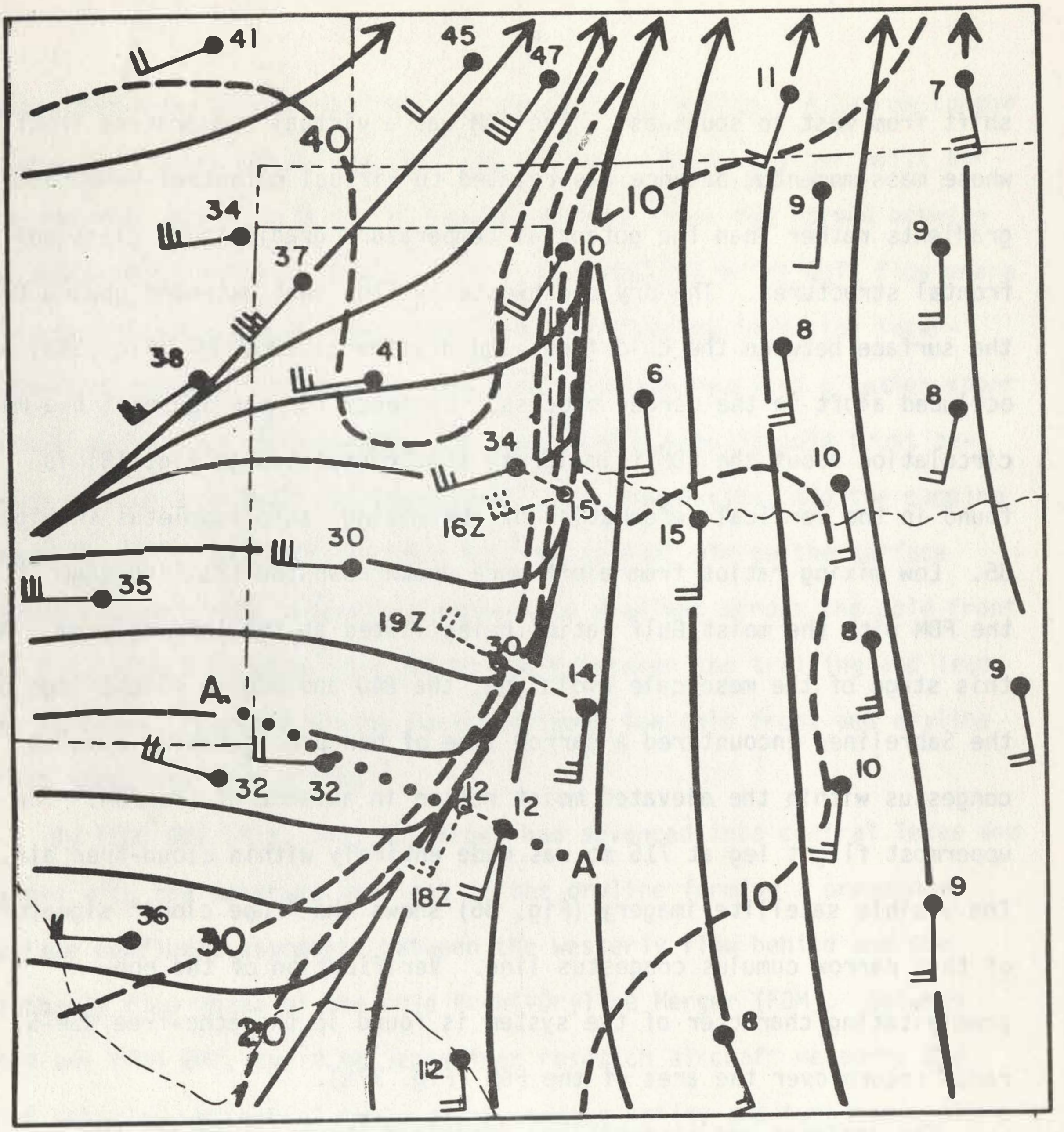

Fig. 34. Same as Fig. 25 but for 1700 GMT. Line AA', projection line for Fig. 35 Sabreliner flight section.

solid line structure had developed from the rather innocuous congestus line of the previous hour. This convective system produced hail and tornadoes over the eastern portions of Kansas and Oklahoma between 2000 GMT and its eventual decay after 0300 GMT 4 April 1981. The satellite images at 1745 (Fig. 38) show the cirrus outflow at the top of the convective elements of Fig. 37b. This example illustrates the short time interval (~1 h) over which the potential instability of the moist layer is released by the "triggering" of the mesoscale forcing.

A marked transformation in the surface boundary-layer flow behind the eastward-moving FDM-mesoconvective system was well under way by 2100 GMT (Fig. 39). The westerly surface wind speeds, which were less than 20 kts behind the cold front during the early morning hours (Fig. 25), had increased to greater than 40 kt with surface gusts exceeding 50 kt at some stations. Blowing dust and limited visibility covered eastern New Mexico and western Oklahoma and Texas. Surface dew-point depressions exceeding 45 F (Fig. 39) occurred over the Texas Panhandle as the dry air which had been occluded aloft in the frontal-dryline merger (Figs. 34 and 35) was mixed downward to the surface by the intense surface boundary-layer turbulence. Evidence for the finescale structure in the boundary-layer mixing is shown in the high-resolution satellite imagery (Fig. 40) which contains complex billow and cellular structure within the dust over west Texas.

During the late afternoon of 3 April, the NCAR Sabreliner executed a second flight to map the ageostrophic flow at jet stream levels adjacent to deep line-form convection. After taking these data (the discussion of

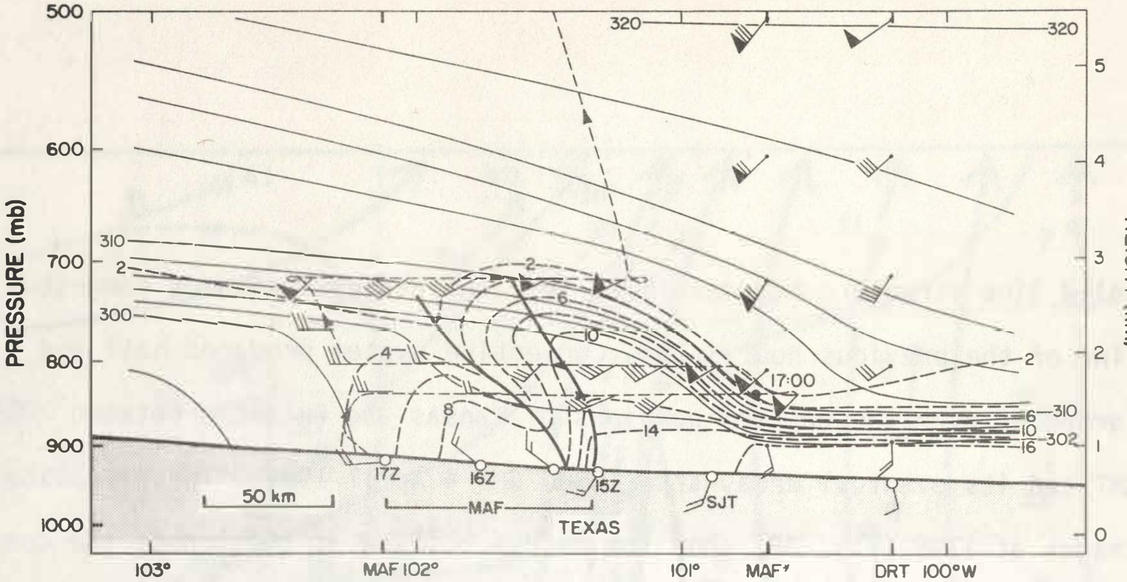

Fig. 35. Cross-section of potential temperature (K, solid lines) and moisture mixing ratio (g Kg^{-1}, thin dashed lines) through the cold front-dryline merger at approximately 1700 GMT 3 April 1981 along the line AA' of Fig. 34. Sabreliner flight track, dashed line. 1300 GMT rawinsonde observations from Midland, Texas (MAF) and Del Rio, Texas (DRT) and surface winds from Midland were space-time adjusted to the 1700 GMT Sabreliner observations. Wind vectors, flag = 25 m s^{-1}, barb = 5 m s^{-1}, half barb = 2.5 m s^{-1}.

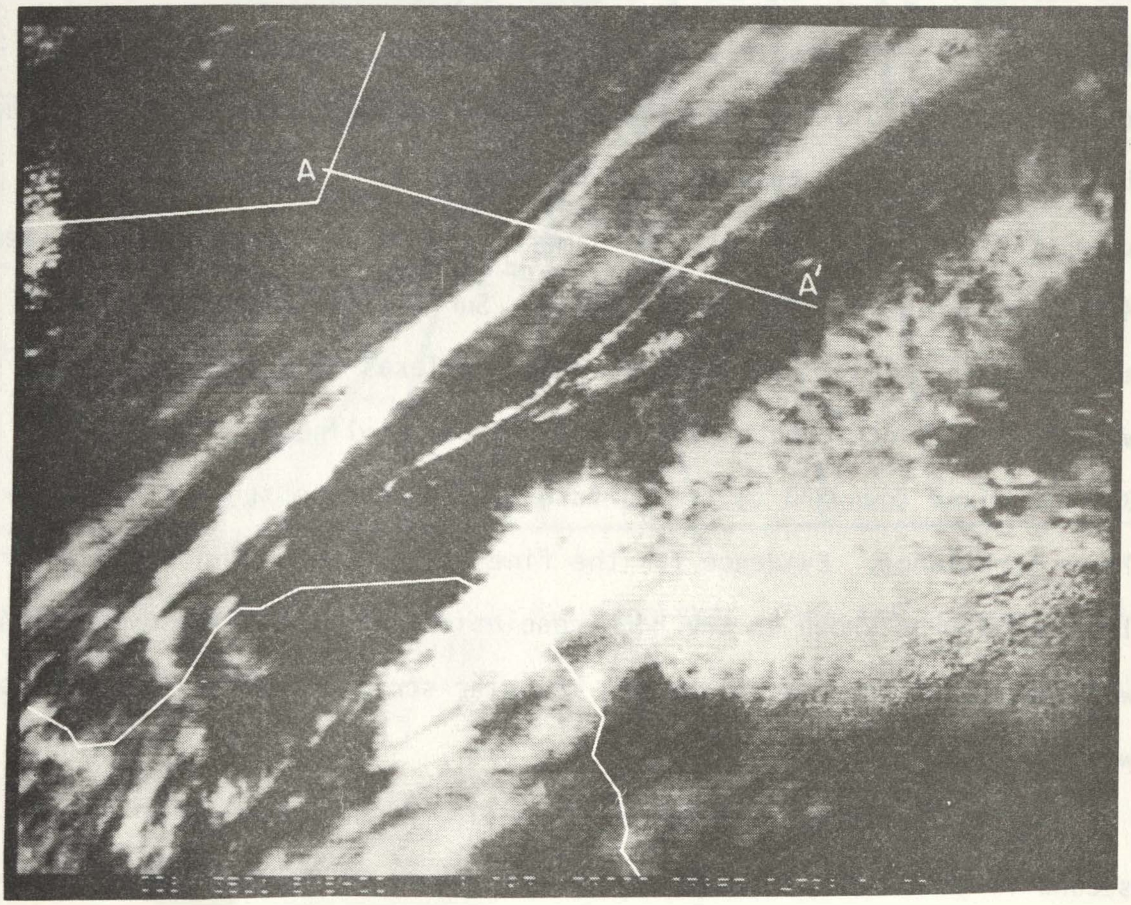

Fig. 36. GOES visible image at 1700 GMT 3 April 1981 over Texas showing cumulus congestus "rope" cloud line at the leading edge of the frontal-dryline merger in Fig. 3.1.34. Line AA', same as Fig. 34. (Courtesy of Dr. Fred Mosher, McIDAS, University of Wisconsin.)

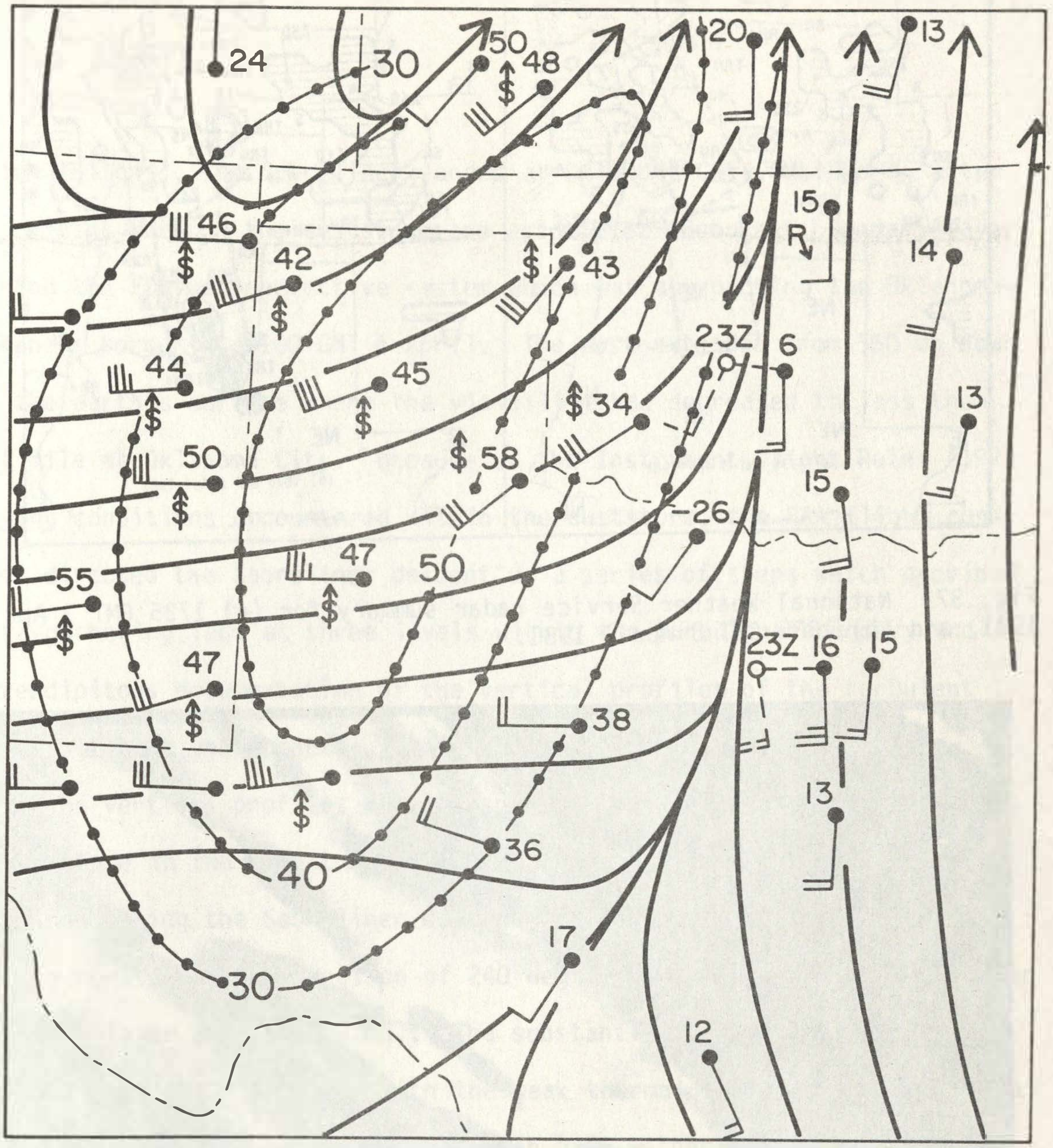

Fig. 39. Surface streamline analysis (solid lines) and maximum surface wind gust (dotted lines) at 2100 GMT 3 April 1981. Surface dewpoint depression (F) plotted by wind vectors.

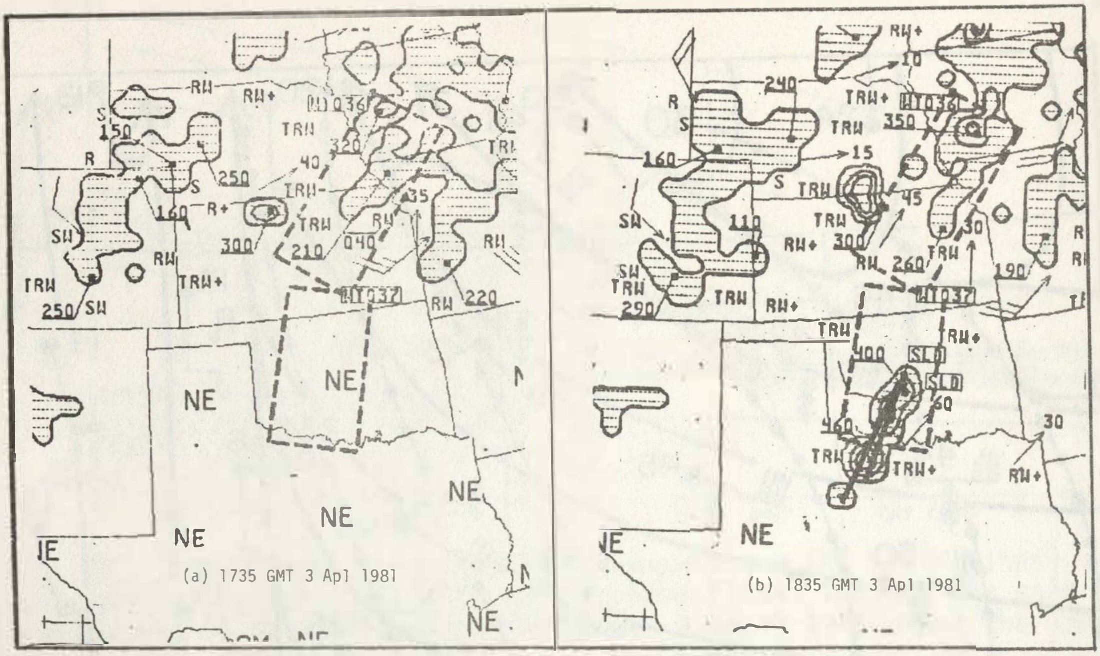

Fig. 37. National Weather Service radar summary for (a) 1735 GMT 3 April 1981, and (b) 1835 GMT 3 April 1981.

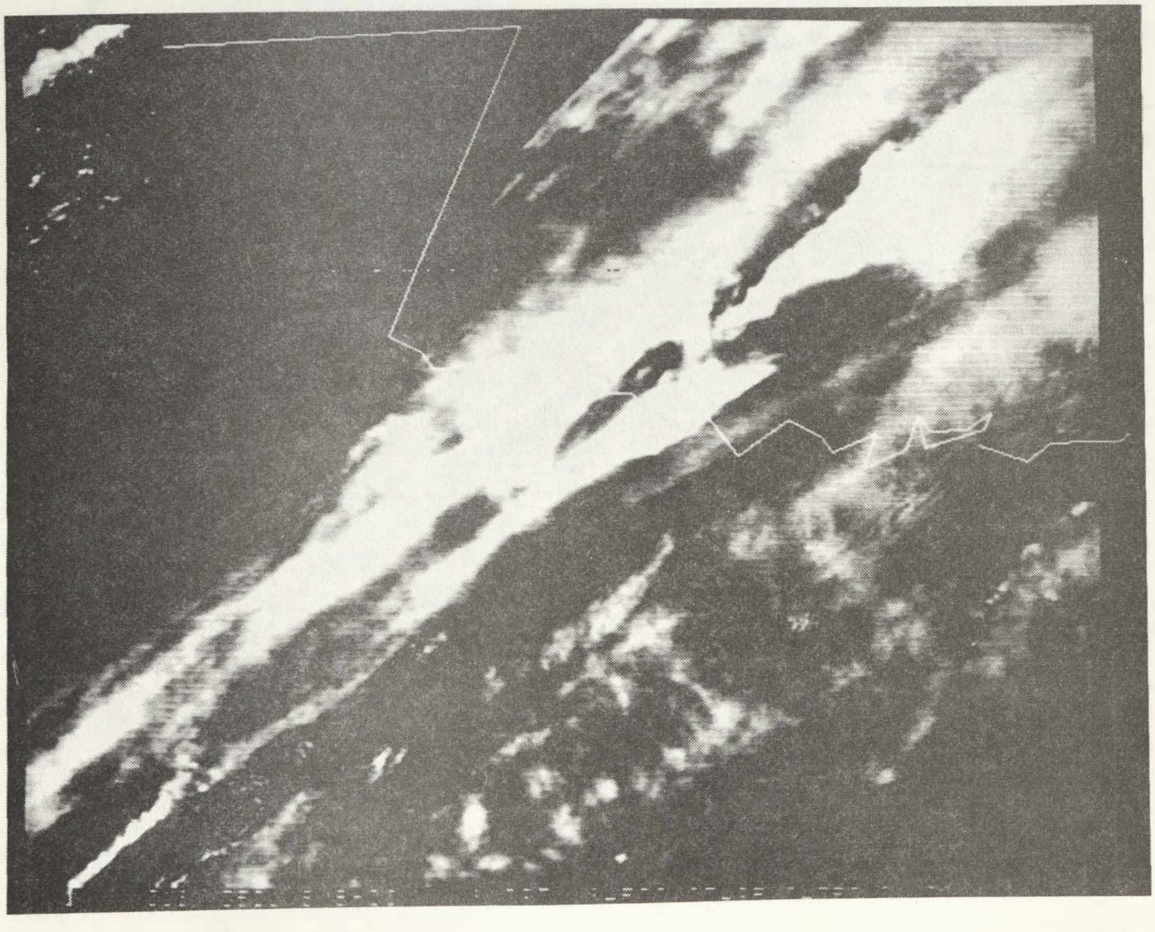

Fig. 38. Same as Fig. 36 but for 1745 GMT 3 April 1981.

which follows), the Sabreliner landed at Oklahoma City, Oklahoma, after descending through the duststorm and associated turbulent boundary layer behind the FDM-mesoconvective system which was approaching the Oklahoma-Arkansas border at 0100 GMT 4 April. The dust extended from 550 mb down to the earth's surface where the visibility had decreased to less than 1/4 mile at Oklahoma City. Because of the Instrument Flight Rules (IFR) flying conditions encountered within the duststorm, the FAA flight control directed the Sabreliner descent as a series of steps which provided data-gathering legs at three levels within the turbulent boundary and a serendipitous documentation of the vertical profiles of the turbulent fluxes of heat and momentum within the turbulent layer.

The vertical profiles of wind speed, wind direction, and potential temperature in the lowest 100 mb of the boundary layer (Fig. 41) were obtained during the Sabreliner descent to landing. The profiles show a nearly constant wind direction of 240 deg and weak thermal stratification over the layer (870 to 950 mb). The substantial vertical wind shear of 17 m s^{-1} $(50 \text{ mb})^{-1}$ combined with the weak thermal stratification gives a gradient Richardson number of less than 0.25 within the turbulent layer.

The traces of the 240 deg wind velocity component U and vertical velocity over the two-minute flight segment at 864 mb within the turbulent boundary layer (Fig. 42a) show the anticorrelation between the horizontal and vertical velocity components which is characteristic of a downward momentum flux within turbulent layers in which $\partial U/\partial p < 0$. The running integral of the covariance between the horizontal velocity perturbations U' and vertical velocity perturbations w' (Fig. 42b), gives a

Fig. 40. GOES visible image at 2345 GMT 3 April over Texas and western Oklahoma. Bright images are clouds. Granular structure over and to the south of the Texas Panhandle is dust. (Courtesy of Dr. Fred Mosher, University of Wisconsin.)

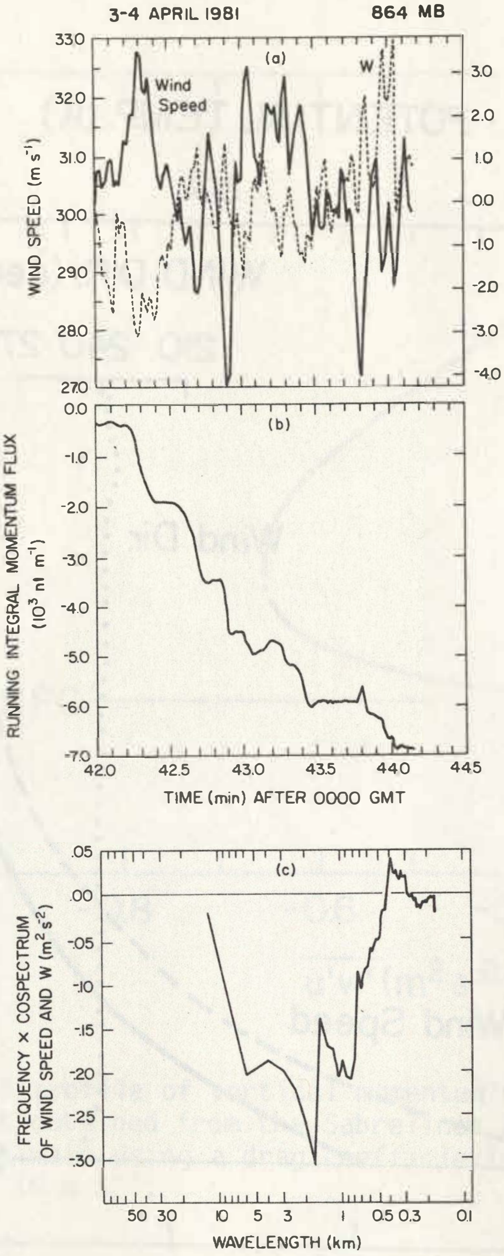

Fig. 42. Sabreliner measurements in surface boundary-layer turbulence at 864 mb on 4 April 1981. (a) Traces of the 240 deg component of the horizontal wind velocity U and the vertical velocity w between 0042.5 GMT and 0044.5 GMT. (b) Running spatial integral of momentum flux. (c) Frequency-weighted cospectrum of U and w.

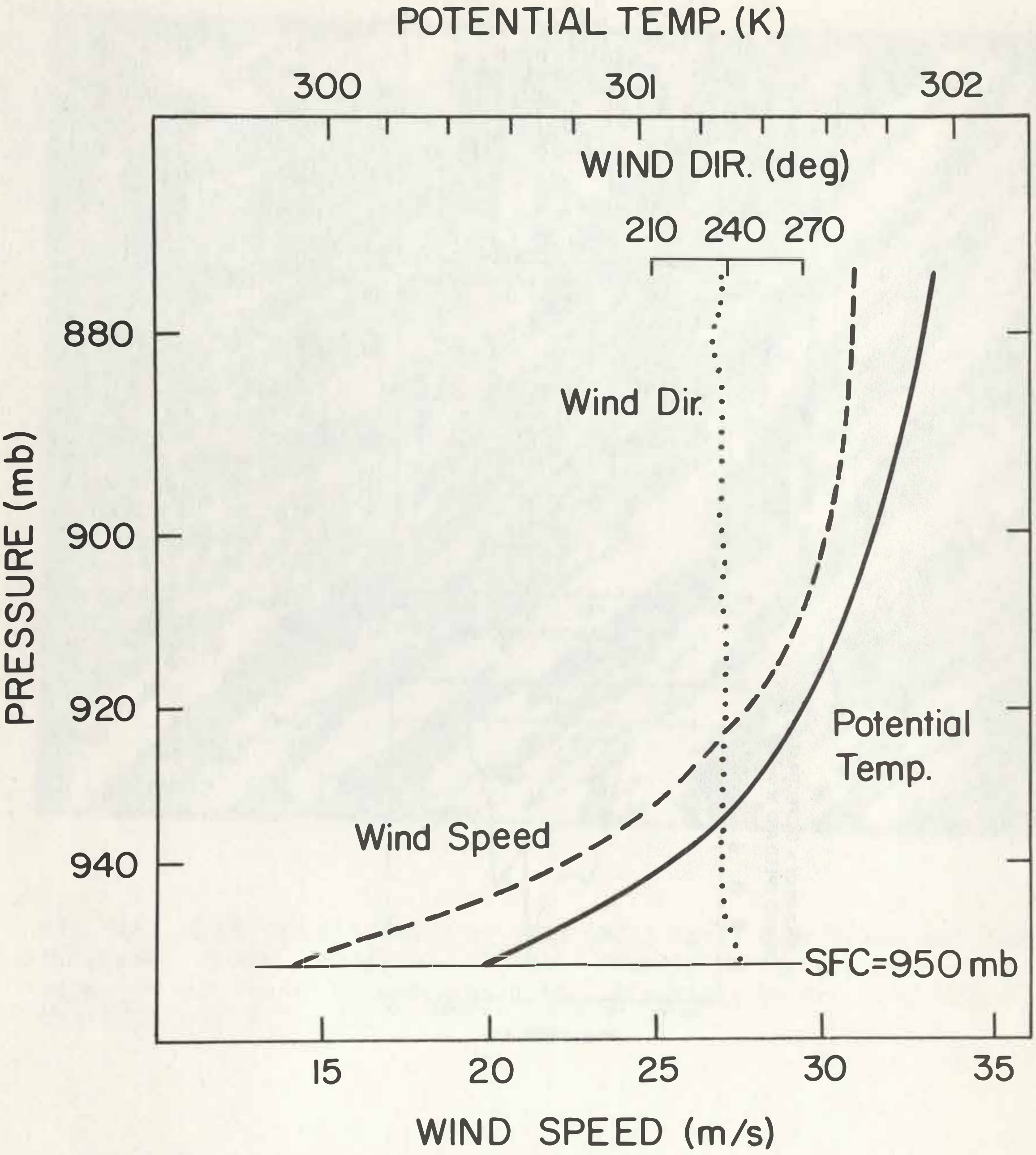

Fig. 41. Vertical profiles of wind speed (dashed), wind direction (dotted) and potential temperature (solid) during the Sabreliner descent into Oklahoma City, Oklahoma, after 0040 GMT 4 April 1981.

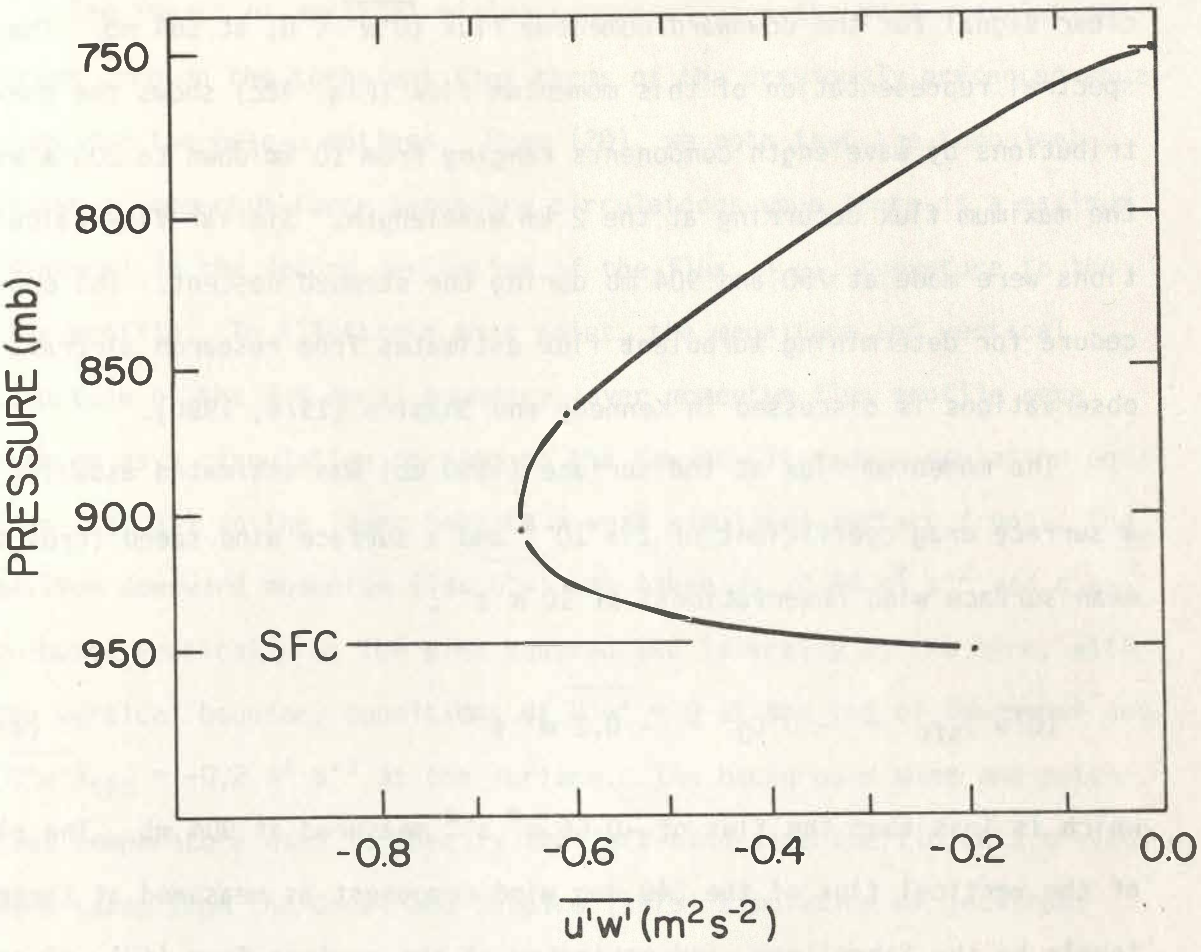

Fig. 43. Vertical profile of vertical momentum flux (m^2 s^{-2}) of the 240 deg wind component obtained from the Sabreliner aircraft measurements and a surface flux estimate using a drag coefficient of 2×10^{-3} and the surface mean wind of 10 m s^{-1}.

clear signal for the downward momentum flux ($\overline{U'w'} < 0$) at 864 mb. The spectral representation of this momentum flux (Fig. 42c) shows the contributions by wavelength components ranging from 10 km down to 200 m with the maximum flux occurring at the 2 km wavelength. Similar flux calculations were made at 750 and 904 mb during the stepped descent. The procedure for determining turbulent flux estimates from research aircraft observations is discussed in Kennedy and Shapiro (1975, 1980).

The momentum flux at the surface (~950 mb) was estimated assuming a surface drag coefficient of 2×10^{-3} and a surface wind speed (from the mean surface wind observations) of 10 m s^{-1},

$$(\overline{U'w'})_{sfc} = - U^2 C_D = - 0.2 \text{ m}^2 \text{ s}^{-2} \tag{43}$$

which is less than the flux of -0.66 m^2 s^{-2} measured at 904 mb. The plot of the vertical flux of the 240 deg wind component as measured at three levels by the Sabreliner, and estimated at the surface from (43), gives the vertical profile of U'w' within the turbulent layer. The results (Fig. 43) show the maximum downward flux of -0.7 m^2 s^{-2} near 900 mb and significant curvature to the momentum flux profile. The profile curvature indicates a maximum of the second derivative of U'w' within the turbulent layer which has been previously observed by Kaimal *et al.* (1970) and Lenschow *et al.* (1980). Estimates of the downward heat flux within the 3-4 April turbulent boundary layer were negligible as the measurements were made in the late afternoon (~0000 GMT) at a time of weak solar surface heating and after the layer had become near-adiabatic.

The impact of vertical mixing processes upon the meso-α evolutions occurs through the turbulent flux terms of the previously presented equations for the meso-α motions. From (20), we note that the turbulent fluxes of momentum force secondary circulations when there is a maximum (minimum) in the second derivative of the flux, i.e., curvature to the flux profile. To illustrate this point, the magnitude and vertical structure of the 3-4 April boundary-layer momentum flux profile were entered as a circulation forcing to the Sawyer-Eliassen circulation equation (Eq. 20) in the layer beneath a weak simulated surface front. The maximum downward momentum flux $\overline{U'w'}$ was taken as -0.66 $m^2\ s^{-2}$ and distributed vertically as the sine squared and laterally as the sine, with the vertical boundary conditions of $\overline{U'w'} = 0$ at the top of the layer and $(\overline{U'w'})_{sfc} = -0.2\ m^2\ s^{-2}$ at the surface. The background wind and potential temperature used to specify the left-hand-side coefficients of (20) were taken from the Gidel and Shapiro (1979) simulation of jet-front development. The imposed boundary-layer forcing (Fig. 44a) produced a thermally direct solenoidal circulation (Fig. 44b) within the boundary layer. The horizontal ageostrophic component to the circulation (Fig. 44c) near the surface is 7 m s^{-1} and is directed toward the rear of the surface front. The sense of the surface ageostrophic flow is to enhance the convergence at the leading edge of the front and for a north-south-oriented front, increases the westerly flow behind the front. The results suggest that the development of the strong westerly surface wind and associated duststorm between 1200 and 2100 GMT (Figs. 25 and 39,

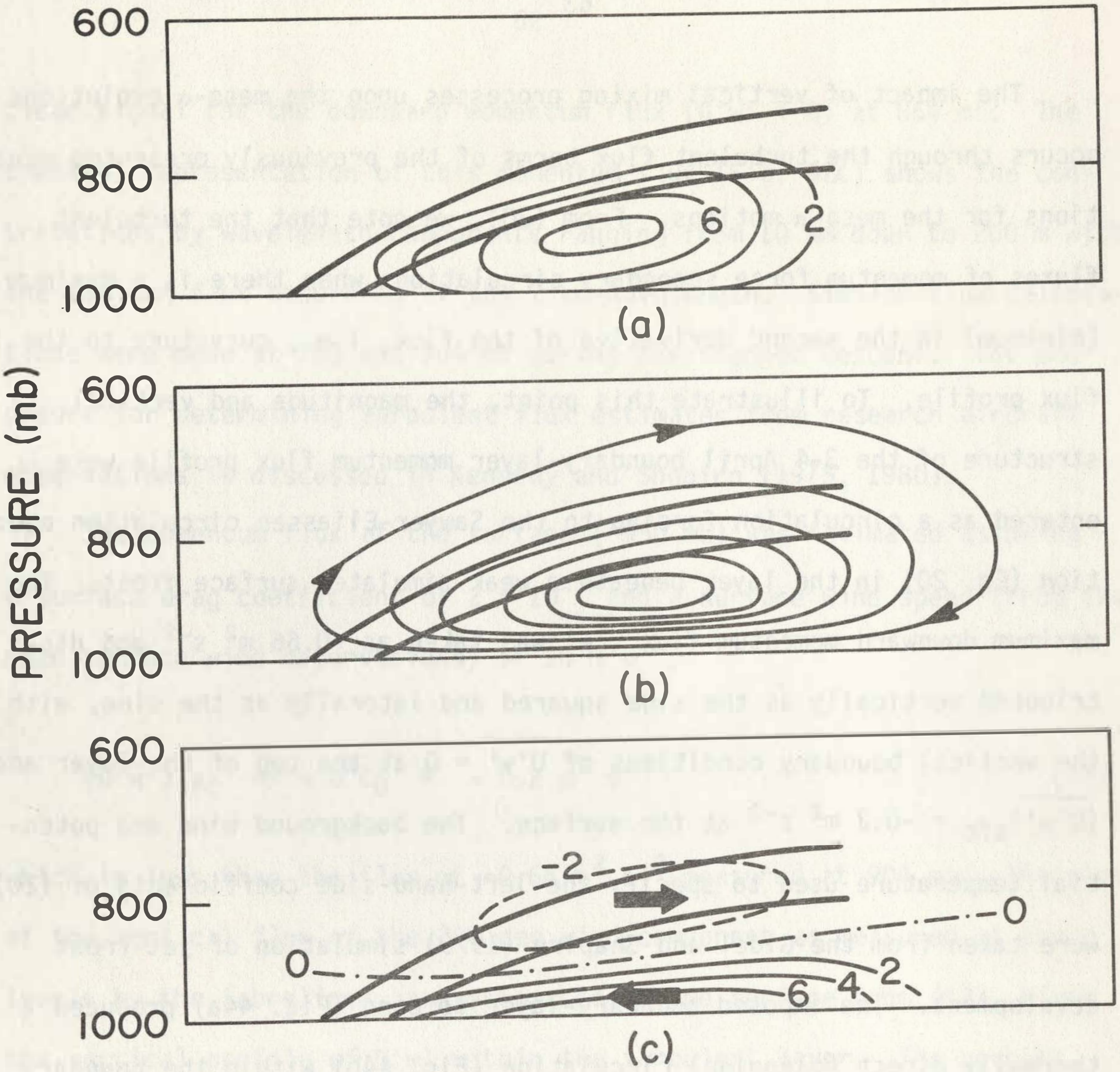

Fig. 44. Secondary circulation forced by a boundary-layer vertical momentum flux beneath a surface cold front. Frontal boundaries, heavy solid lines. (a) Momentum flux forcing (10^{-5} s^{-2}). (b) Streamfunction of the secondary circulation (m s^{-1} mb^{-1}) isoline interval = 200 m s^{-1} mb^{-1}. (c) Horizontal ageostrophic velocity component v_a (m s^{-1}); heavy arrows show direction of v_a.

respectively) is related to the development of a secondary circulation induced by a maximum of downward momentum flux within the surface boundary layer. Furthermore, the frontal convergence and the ascent at the leading edge of the front are enhanced by this boundary-layer forcing and may play a significant role in the triggering and maintenance of the pre-frontal squall line.

The second flight of the Sabreliner departed Albuquerque, New Mexico, at 2200 GMT. The aircraft ascended to 243 mb and executed a series of flight legs along a sawtoothed track to measure the wind velocity and geopotential height distribution of the southwesterly jet stream over Texas and Oklahoma. In previous studies, Shapiro and Kennedy (1981) and Brown et al. (1981) combined research aircraft inertial wind and radar altimeter height measurements to obtain estimates of jet stream ageostrophic winds over flat terrain (water). This technology was later applied over irregular terrain (Shapiro and Kennedy, 1982) by charting the path of the aircraft over high-resolution (~ 1 km) digital topographic maps and removing the undulations of the underlying terrain from the radar altimeter data.

Figure 45 presents the 243 mb wind velocity analysis of the Sabreliner measurements supplemented with the 250 mb rawinsonde observations from 0000 GMT 4 April which shows a >80 m s^{-1} jet core over western Oklahoma. The mesoconvective system on the anticyclonic shear side of the jet shown in the 2345 GMT 3 April radar return contained convective elements extending to the 150 mb level during the period of the aircraft observations. The analysis of the terrain-corrected radar altimeter

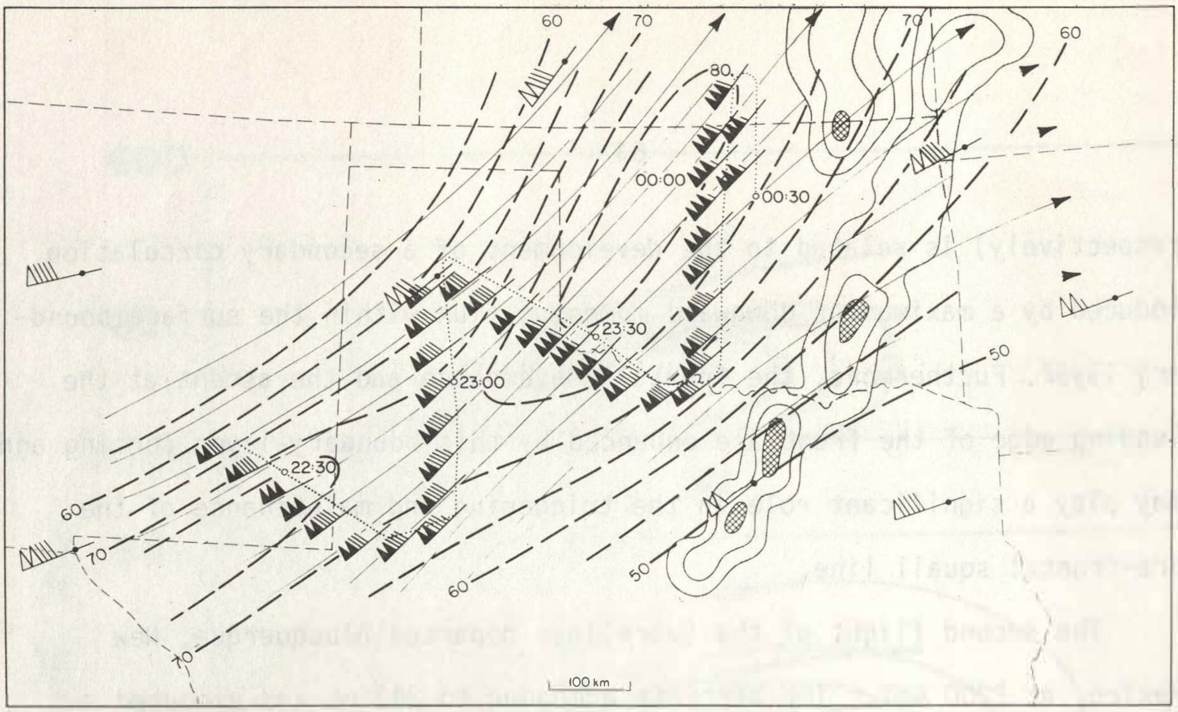

Fig. 45. 243 mb analysis of wind speed ($m\ s^{-1}$, heavy dashed lines) and wind direction (streamlines, thin solid lines) at approximately 0000 GMT 4 April 1981. Wind vectors, flag = 25 $m\ s^{-1}$. Sabreliner flight track, dotted line. Rawinsonde 250 mb wind observations, open flags. Selected Sabreliner wind observations plotted along the flight track. National Weather Service radar shown for three levels of reflectivity intensity: level 1, shaded; level 2, clear; level 3, cross-hatched (after Shapiro and Kennedy, 1982).

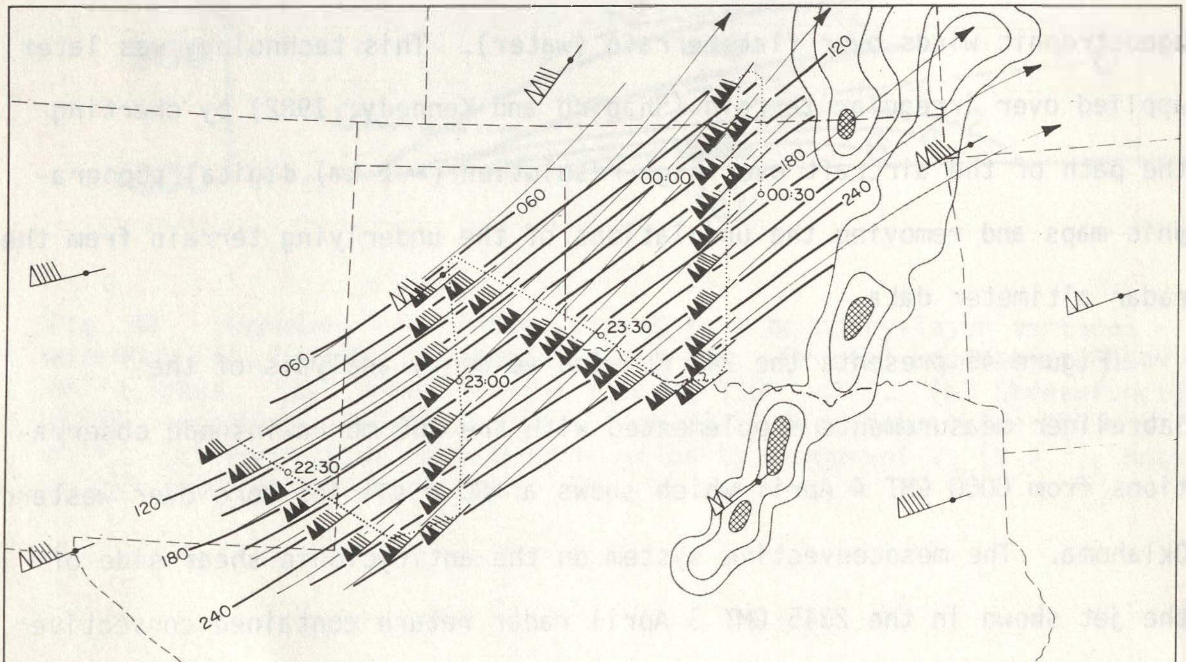

Fig. 46. Analysis of terrain-corrected D-value height for Fig. 45. Streamlines, wind vectors, radar reflectivity, same as Fig. 45 (after Shapiro and Kennedy, 1982).

heights (Fig. 46) shows a substantial deviation of the observed wind flow (streamlines) from the geostrophic flow (height lines). The magnitude of this cross-contour (ageostrophic) flow reaches 16 m s^{-1} and is in the kinetic-energy-generating sense being directed form higher to lower heights. This observed ageostrophic flow cannot be explained through parcel acceleration dynamics as the ageostrophic flow is largest at the core of the jet where one would expect to find minimal velocity accelerations and associated cross-contour ageostrophic motions.

A synoptic view of the 3-4 April 1981 jet streak is presented in Fig. 47. The streamline and height analysis (Fig. 48) shows the deflection of the observed wind toward lower heights behind the mesoconvective system (as in Fig. 46) and the deflection toward higher heights downstream from the convection. Studies by Ninomiya (1971) and Fritsch and Maddox (1981) suggest that jet stream intensifications and ageostrophic deflections are induced by internal processes within mesoconvective systems, i.e., diabatic heating through the latent heat of condensation. Newton (1950) described how momentum fluxes by the vertical air currents within convective systems force secondary (ageostrophic) circulations when the convection takes place within an environment containing vertical wind shear.

The feedback of mesoconvective processes into the jet-front motions may be illustrated by considering simulated mesoconvective diabatic heating and vertical momentum flux distributions as forcings to the Sawyer-Eliassen circulation equation (Eq. 20). From the right-hand side of Eq. (20), we note that secondary circulations are forced by lateral gradients

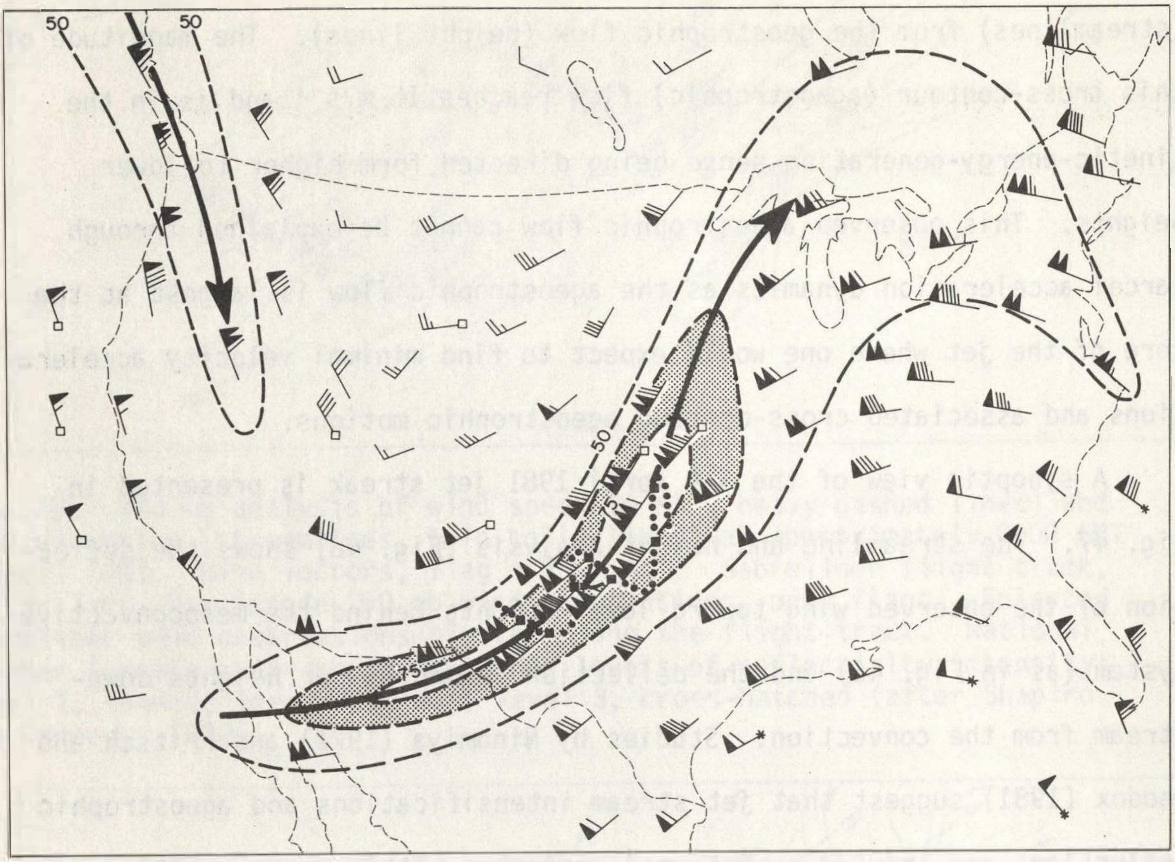

Fig. 47. 250 mb wind speed analysis (m s^{-1}, dashed lines) at 0000 GMT 4 April 1981. Rawinsonde wind velocities (flag = 25 m s^{-1}, barb = m s^{-1}, half barb = 2.5 m s^{-1}), commercial airline wind reports (open box vectors), satellite cloud motion winds (astrisked vectors), Sabreliner research aircraft winds at 243 mb (closed box vectors). Jet stream axis (heavy solid arrow) and 62.5 to 75.0 m s^{-1} wind speed interval (stippled area) (after Shapiro and Kennedy, 1982).

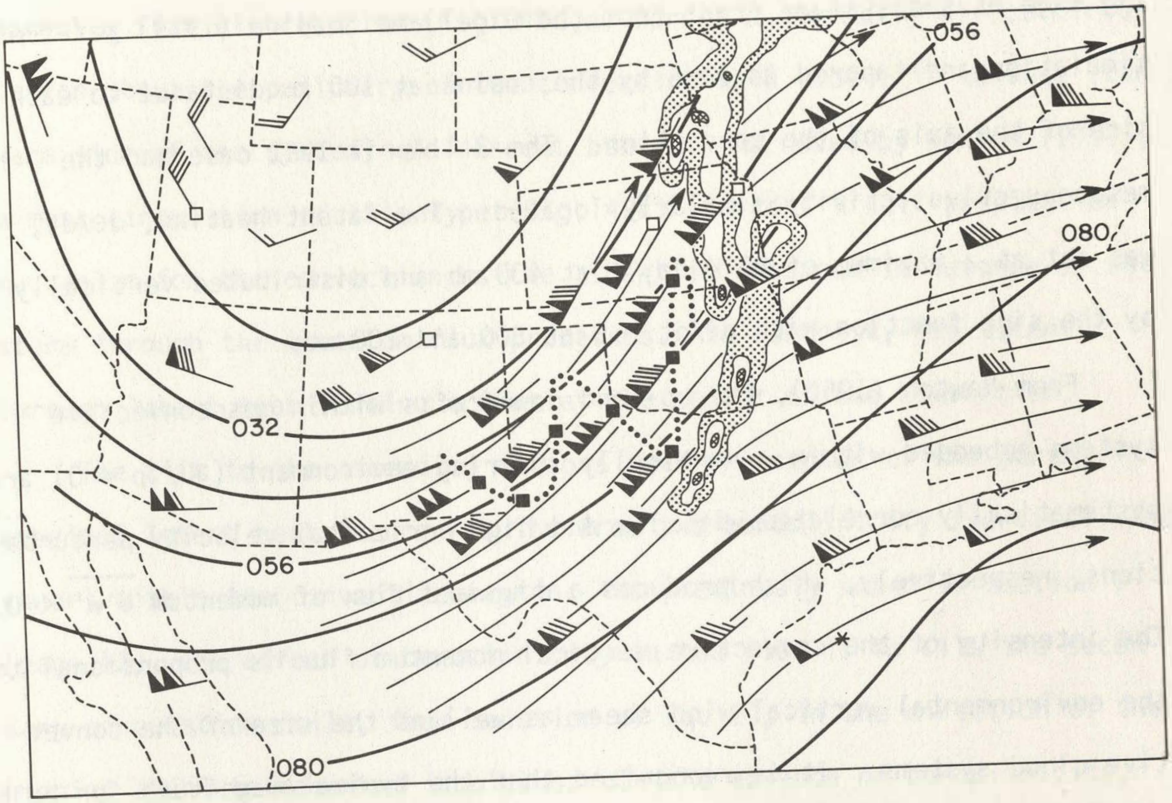

Fig. 48. 250 mb height analysis (m, heavy lines) and streamlines, thin lines for Fig. 47.

in diabatic heating and the previously discussed presence of an elevated maximum (minimum) in the vertical momentum flux. The simulated convection was placed to the anticyclonic shear side of the jet over the leading edge of the surface front from the Gidel and Shapiro (1979) jet-front simulation and tapered to zero by the cosine at 100 km distance to each side of the axis of the convection. The 3-4 April 1981 case had the mesoconvective activity similarly located. The latent heating, $d\Theta/dt$, was set at a maximum of 80 K day^{-1} at 400 mb and distributed vertically by the sine function with $d\theta/dt = 0$ at 800 and 200 mb.

From Newton (1950), the up- and downdrafts within mesoconvective systems embedded within a vertically shearing environment ($\partial U/\partial p \neq 0$) are systematically correlated with low and high horizontal velocity perturbations, respectively, which produces a downward flux of momentum $\overline{U'w'} < 0$. The intensity of the convective vertical momentum flux is proportional to the environmental vertical wind shear as well as the size of the convective cloud systems. It is recognized that the typical magnitude for both the horizontal and vertical velocity perturbations within cumulonimbus up- and downdrafts is on the order of 10 m s^{-1}. What is not established is the percentage of a given mesoconvective area, A, which is covered by perturbations of this magnitude. For the present study, we set $A = 0.25\% = 0.0025$ and $\overline{U'w'} = -10^2\ \mathrm{m}^2\ \mathrm{s}^{-2}$ at the mesoconvective axis, with a maximum at 400 mb tapered laterally and vertically to zero in the same manner as was done for the imposed latent heating distribution.

The results of imposing the above-described mesoconvective latent heating and vertical momentum flux distributions as secondary circulation forcings to (20) are shown in Fig. 49. The latent heating (Fig. 49a, b) forces an ascending plume along the axis of maximum heating with compensating sinking motions on the periphery of the convection. The imposed momentum flux distribution (Fig. 49c,d) forces a thermally direct circulation about the periphery of the convection with ascent in advance (the warm side of the system) and descent behind. As noted by Newton (1950), a mass circulation of this type (Fig. 49c) provides a self-propagation mechanism for the convection as the ascent is enhanced in advance of the storm through the momentum flux processes. In contrast, the ascent through latent heat forcing occurs at the center of the convection.

The tilt to the ascending motions near the center of the parameterized latent heat source results from the baroclinicity (vertical wind shear) within the convective region. As previously noted in section 2 (page 13), the effect of baroclinicity in the flow is to tilt the secondary circulation cells, from solution of Eq. 20, in the direction of the sloping absolute momentum isopleths. In the absence of baroclinicity, the diabatically forced ascent (and descent) is vertical oriented, i.e., non-sloping. The tilt in the diabatically forced circulation places the low-level convergence slightly ahead of the region of maximum heating and therefore may contribute to the forward propagation of the mesoconvective system. Furthermore, evaporative cooling of precipitation within convective downdrafts (not included in this study), though not as strong as the condensation heating, may also contribute to the diabatically forced circulations. Downdraft cooling below and to the rear of the condensation heating partially compensates for the lower tropospheric heating and also tilts the net heating along the axis of the sloping convective

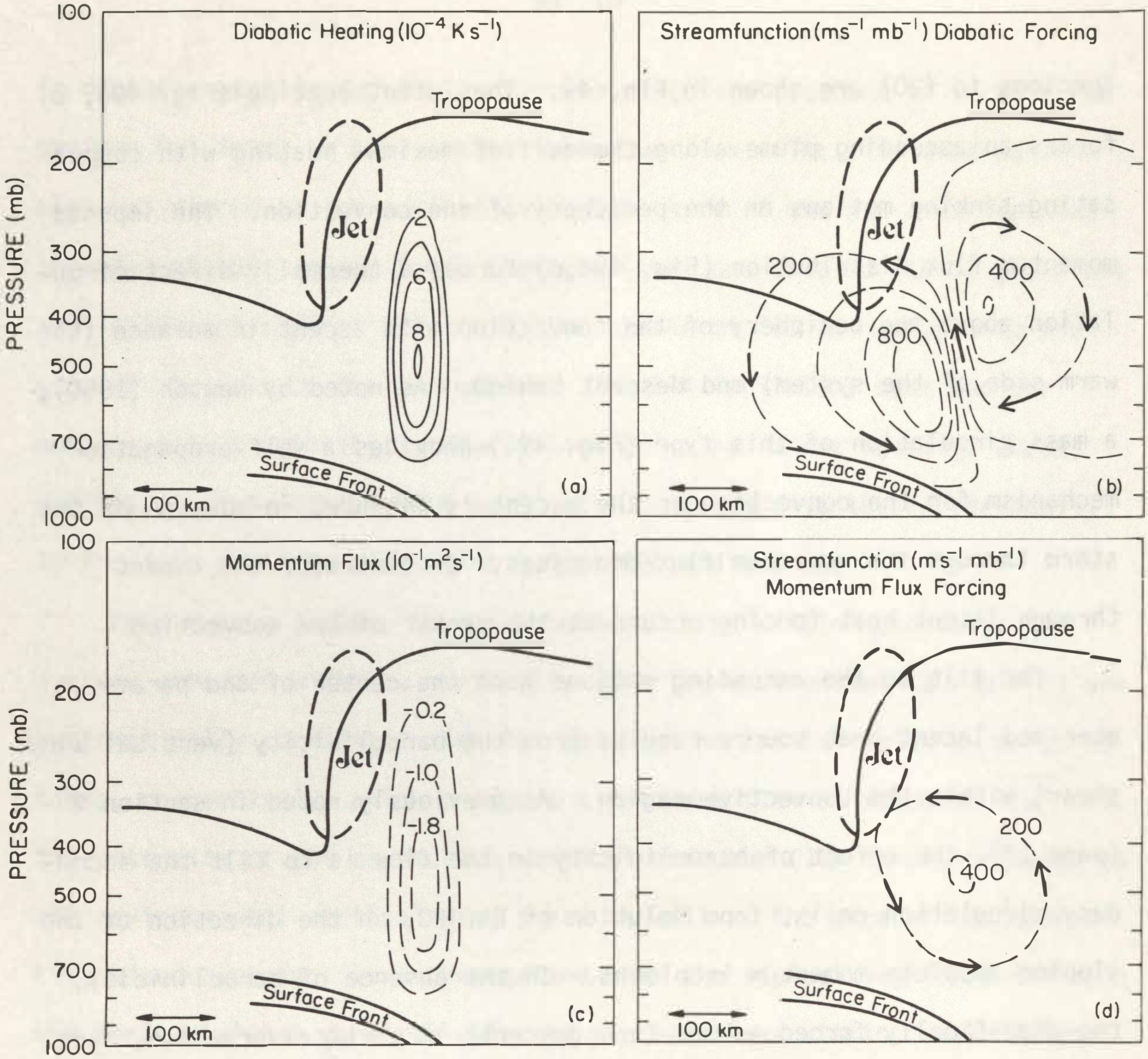

Fig. 49. Simulated mesoconvective forcing of the secondary circulation in the vicinity of jet stream-frontal zone system. (a) Convective diabatic (latent) heating, 10^{-4} K s^{-1}. (b) Circulation streamfunction (m s^{-1} mb^{-1}) for (a) heating. (c) Convective vertical momentum flux, 10^{-1} m^2 s^{-2}. (d) Circulation streamfunction (m s^{-1} mb^{-1}) for (c) momentum flux. Tropopause and surface frontal boundaries, heavy solid lines. The 40 m s^{-1} isotach of the upper-level jet, heavy dashed line.

updraft, as in the squall-line composited by Newton (1950). Because of the choice of magnitudes for the mesoconvective heating and momentum flux parameters, the heating dominated the momentum flux forcing in the present simulation.

The results from the combined heat and momentum forcing (Fig. 50) illustrate the feedback of the mesoconvective processes into the dynamics of the jet stream. The convective processes have forced a secondary circulation which acts to increase the kinetic energy of the upper jet. The horizontal component of the ageostrophic flow (Fig. 50d) is directed across the jet core from the anticyclonic to the cyclonic shear side of the jet and has a maximum value of 8 m s^{-1} in the vicinity of the jet core. This result is consistent with both direction and order of magnitude of the measured ageostrophic flow behind the 3-4 April 1981 mesoconvective system (Fig. 46).

The impact of diabatically forced secondary circulations upon mesoconvective evolutions is to accentuate the intensity of the pre-existing geostrophically forced low-level convergence and midtropospheric ascent within the region of either linear- or complex-form mesoconvection. The impact of the convective vertical momentum flux upon mesoconvective evolutions is very much affected by the environmental vertical wind shear. As noted earlier, the circulation forced by the convective momentum flux creates low-level convergence and ascent in advance of the convection and suppresses convective buildups in the rear, thus providing the self-propagation mechanism as described by Newton (1950). For the case of strong geostrophic forcing of squall-line convective systems, the convective momentum flux processes cause the convection to propagate at a

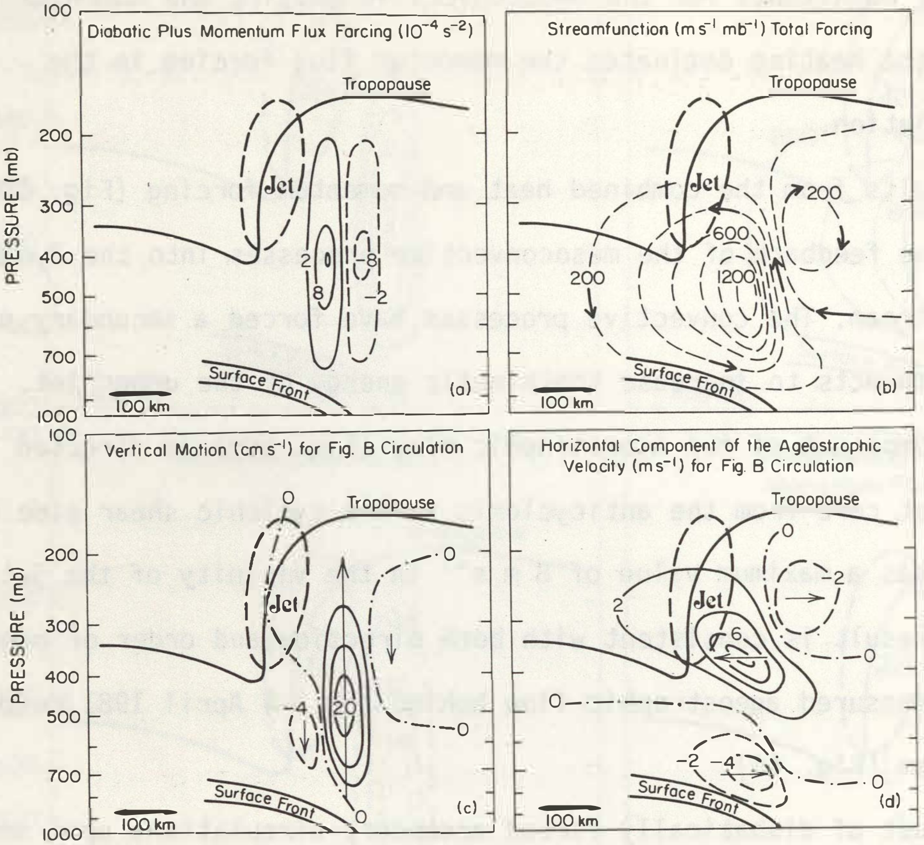

Fig. 50. Mesoconvectively forced secondary circulation for the simulated diabatic heating plus vertical momentum flux distributions of Fig. 49. Front, tropopause and jet, same as Fig. 49. (a) Total forcing function, diabatic plus momentum flux 10^{-4} s^{-2}. (b) Total circulation streamfunction (m s^{-1} mb^{-1}) for (a) forcing. (c) Vertical motion (cm s^{-1}) for (b) circulation (d0 horizontal component (m s^{-1}) of the (b) circulation.

faster speed than the geostrophic deformations which initially triggered the convection. The result is that the squall line propagates out away from the region of meso-α forcing (prefrontal moisture convergence and potential instability) and eventually dissipates. Because weakly forced MCCs evolve within weakly sheared environments, they do not possess the strong self-propagation characteristics of squall-line convective systems and hence are not as prone to propagate away from the region of meso-α forcing. We suggest that the duration of MCC versus squall-line convection (12-24 h versus < 12 h, respectively) is related in part to the effect of convective momentum flux processes upon the motion of organized mesoconvective systems. Finally, it is essential that cumulus parameterizations within mesoscale numerical prediction models include the effect of convective momentum fluxes so that they may properly simulate and predict the motion and life cycle of the parameterized convective precipitation processes and their feedbacks into the larger scales of motion.

In summary, this case study illustrates the diversity and complexity of the multiscale processes, their interactions and feedbacks which contribute to the evolution of severe weather events. Given our present level of understanding of these processes and the recent technological advances in atmospheric observing systems, we may proceed to the next quantum in describing, diagnosing, understanding, and predicting the continuous spectrum of macro-β through micro-γ motions that give rise to weather events such as occurred during 3-4 April 1981.

10. Suggested Key Research Issues

We now present suggestions as to some key research issues which should be addressed in our quest for future scientific achievements in understanding and predicting mesoscale weather events.

- Determine the effect of space-time varying geostrophic deformations within cyclones upon the evolution of jet stream and frontal zone systems and their associated precipitation. What is the sensitivity of jet-front systems to larger-scale forcings within and outside of the mesoscale domain?
- Establish the impact of processes within fronts and jet streams upon larger-scale synoptic and planetary systems (i.e., cyclogenesis and blocking). Is it necessary to incorporate mesoscale observations, mesoscale grid resolution, and their physical processes into medium-range numerical weather prediction?
- Investigate the vertical coupling between upper- and lower-troposphere jet-front systems and its effect upon the initialization and maintenance of severe organized mesoconvective systems. What are the "triggering" mechanisms for organized mesoconvective systems?
- Establish the importance of clear-air turbulence (CAT) upon the evolution of upper-level jet-front systems. Is it necessary to develop parameterizations of meso-β through micro-γ vertical mixing processes within elevated shear layers to simulate numerically and predict upper-tropospheric and lower-stratospheric jet stream dynamics?

- Quantify the role of tropopause folding and associated turbulent mixing in the exchange of chemical trace constituents across the tropopause. How much stratospheric ozone and anthropogenic pollution is transferred across the tropopause through meso- and microscale processes?
- Observe and parameterize planetary boundary-layer heat, momentum, and moisture fluxes during the development of low-level fronts, drylines, capping inversions, and organized mesoconvective systems. To what extent is Texas-Oklahoma squall-line formation tied to secondary circulations which are driven in part by boundary-layer turbulent flux processes?
- Investigate the evolution of orographically forced mesoscale systems (i.e., mountain waves, upslope precipitation systems, and downslope windstorms) and quantify the role of steep topography in promoting the onset of severe weather events. Is MCC formation initiated by the convergence of dry Rocky Mountain westerly downslope flow with potentially unstable southerly flow off the Gulf of Mexico?
- Understand the upscale development of MCCs from an isolated convective element within a weakly forced meso-α environment into a 100,000 km^2 area of mesoconvective activity sharing a common outflow anvil. Are MCCs extratropical counterparts of the tropical convective cloud clusters extensively studied during the GARP Atlantic Tropical Experiment (GATE)?

- Determine the impact of convective vertical momentum flux and convective diabatic heating upon the evolution of meso-α and macro-β systems. How do we parameterize cloud-scale momentum fluxes in synoptic-scale and mesoscale numerical weather prediction models?

Beebe, R. G., and F. C. Bates, 1955: A mechanism for assisting in the release of convective instability. Mon. Wea. Rev., 83, 1-10.

Bennetts, D. A., and B. J. Hoskins, 1979: Conditional symmetric instability--a possible explanation for frontal rainbands. Quart. J. Roy. Meteor. Soc., 105, 945-962.

Bergeron, T., 1928: Uber die dreidimensional verknupfende Wetteranalyse I. Geofys. Publ., 5, No. 6, 111 pp.

Bjerknes, J., 1919: On the structure of moving cyclones. Geofys. Publ., No. 1, 1-8.

Bjerknes, J., and H. Solberg, 1922: Life cycle of cyclones and the polar front theory of atmospheric circulation. Geofys. Publ., 3.

Bjerknes, J., and E. Palmén, 1937: Investigations of selected European cyclones by means of serial ascents. Geofys. Publ., 12, 1-61.

Blackadar, A. K., 1957: Boundary layer wind maxima and their significance for the growth of nocturnal inversions. Bull. Amer. Meteor. Soc., 38, 283-290.

Blumen, W., 1980: A comparison between the Hoskins-Bretherton model of frontogenesis and the analysis of an intense surface frontal zone. J. Atmos. Sci., 37, 64-77.

Bonner, W. D., and J. Paegle, 1970: Diurnal variations in boundary layer winds over the south-central United States in summer. Mon. Wea. Rev., 98, 735-44.

Bosart, L. F., 1970: Mid-tropospheric frontogenesis. Quart. J. Roy. Meteor. Soc., 96, 442-471.

Brown, E. N., M. A. Shapiro, P. J. Kennedy and C. A. Friehe, 1981: The application of airborne radar altimetry to measurement of height and slope of isobaric surfaces. J. Appl. Meteor., 20, 1070-1075.

Carlson, T. N., 1980: Airflow through midlatitude cyclones and the comma cloud pattern. Mon. Wea. Rev., 108, 1498-1509.

Charney, J., 1962: Integration of the primitive and balance equations. Proc. International Symposium on Numerical Weather Prediction, Tokyo, 131-152.

Danielson, E. F., 1968: Stratospheric-tropospheric exchange based upon radioactivity, ozone, and potential vorticity. J. Atmos. Sci., 25, 502-518.

Dutton, J. A., 1969: An energy budget for a layer of stratospheric CAT. Radio Sci., 4, 1137-1142.

Eliassen, A., 1948: The quasi-static equations of motion with pressure as independent variable. Geofys. Publ., 17, No. 3, 44 pp.

Eliassen, A., 1962: On the vertical circulation in frontal zones. Geofys. Publ. (V. Bjerknes Memorial Vol.), 24, 147-160.

Eliassen, A., and E. Kleinschmidt, 1957: Dynamic meteorology. Handbuch der Physik, Vol. 48, Berlin, Springer-Verlag, 1-154.

Emanuel, K., 1979: Inertial instability and mesoscale convective systems. Part 1: Linear theory of inertial instability in rotating, viscous fluids. J. Atmos. Sci., 36, 2425-2449.

Endlich, R., 1963: The detailed structure of the atmosphere in regions of clear air turbulence. Final Report, SRI Project No. 4055, Contract CW13-10324.

Fawbush, E. J., and R. C. Miller, 1954: The types of air masses in which North American tornadoes form. Bull. Amer. Meteor. Soc., 35, 154-165.

Fritsch, J. M., and R. A. Maddox, 1981a: Convectively driven mesoscale weather systems aloft. Part I: Observation. J. Appl. Meteor., 20, 9-19

Fujita, T., 1958: The structure and movement of a dry dry front. Bull. Amer. Meteor. Soc., 39, 574-582.

Gidel, L. T., 1978: Simulation of differences and similarities of warm and cold surface frontogenesis. J. Geophys. Res., 83, 915-928.

Gidel, L. T., and M. A. Shapiro, 1979: The role of clear air turbulence in the production of potential vorticity in the vicinity of upper tropospheric jet stream-frontal systems. J. Atmos. Sci., 36, 2125-2138.

Holton, J. R., 1979: An Introduction to Dynamic Meteorology. International Geophysics Series Vol. 23, Academic Press, New York, 391 pp.

Hoskins, B. J., 1971: Atmospheric frontogenesis models: Some solutions. Quart. J. Roy. Meteor. Soc., 97, 139-153.

Hoskins, B. J., 1974: The role of potential vorticity in symmetric stability and instability. Quart. J. Roy. Meteor. Soc., 100, 480-482.

Hoskins, B. J., 1975: The geostrophic momentum approximation and the semi-geostrophic equations. J. Atmos. Sci., 32, 233-242.

Hoskins, B. J., and I. Draghici, 1977: The forcing of ageostrophic motion according to the semi-geostrophic equations and in an isentropic coordinate model. J. Atmos. Sci., 34, 1859-1867.

Hoskins, B. J., and N. V. West, 1979: Baroclinic waves and frontogenesis. Part II: Uniform potential vorticity jet flows--cold and warm fronts. J. Atmos. Sci., 36, 1663-1680.

Hoskins, B. J., and W. A. Heckley, 1981: Cold and warm fronts in baroclinic waves. Quart. J. Roy. Meteor. Soc., 107, 79-90.

Kaimal, J. C., J. J. Wyngaard, D. A. Haugen, O. R. Coté, and Y. Izumi, 1976: Turbulence structure in the convective boundary layer. J. Atmos. Sci., 33, 2152-2169.

Kennedy, P. J., and M. A. Shapiro, 1975: The energy budgets in a clear air turbulence zone as observed by aircraft. Mon. Wea. Rev., 103, 650-654.

Kennedy, P. J., and M. A. Shapiro, 1980: Further encounters with clear air turbulence in research aircraft. J. Atmos. Sci., 37, 987-993.

Keyser, D., and R. A. Anthes, 1982: The influence of planetary boundary layer physics on frontal structure in the Hoskins-Bretherton horizontal shear model. J. Atmos. Sci., 39, in press.

Kung, E. C., 1977: Energy sources in middle-latitude synoptic-scale disturbances. J. Atmos. Sci., 34, 1352-1365.

Lenschow, D. H., J. C. Wyngaard, and W. T. Pennell, 1980: Mean-field and second-moment budgets in a baroclininc, convective boundary layer. J. Atmos. Sci., 37, 1313-1326.

Lilly, D. K., 1981: Doppler radar observations of upslope snowstorms. Preprints 20th Conference on Radar Meteorology, 3 December 1981, Amer. Meteor. Soc.

Lumley, J. L., and H. A. Panofsky, 1964: The structure of atmospheric turbulence. Interscience, 239 pp.

Maddox, R. A., 1980: Mesoscale convective complexes. Bull. Amer. Meteor. Soc., 61, 1374-1387.

Maddox, R. A., 1981: The structure and life cycle of midlatitude mesoconvective complexes. Atmos. Sci. Paper No. 3nd E. Kleinschmidt, 19 der Physik, Vol. 48, Berlin, Springer-Verlag, 1-154.

Maddox, R. A., 1982: Large-scale meteorological conditions associated with midlatitude mesoconvective complexes. Mon. Wea. Rev. (submitted).

McWilliams, J. C., and P. R. Gent, 1980: Intermediate models of planetary circulations in the atmosphere and ocean. J. Atmos. Sci., 37, 923-942.

Means, L. L., 1954: A study of the mean southerly wind-maximum in low-level associated with a period of summer precipitation in the middle west. Bull. Amer. Meteor. Soc., 35, 166-170.

Metcalf, J. I., 1975: Gravity waves in a low-level inversion. J. Atmos. Sci., 32, 351-361.

Murray, R., and S. M. Daniels, 1953: Transverse flow in the entrance and exit to jet streams. Quart. J. Roy. Meteor. Soc., 79, 236-241.

Namias, J., and P. F. Clapp, 1949: Confluence theory of the high tropospheric jet stream. J. Meteor., 6, 330-336.

Newton, C. W., 1950: Structure and mechanism of the prefrontal squall line. J. Meteor., 7, 210-222.

Newton, C. W., 1954: Frontogenesis and frontolysis as a three-dimensional process. J. Meteor., 11, 449-461.

Newton, C. W., 1956: Mechanisms of circulation change during lee cyclogenesis. J. Meteor., 13, 528-539.

Newton, C. W., 1963: Dynamics of severe convective storms. Meteor. Monogr., 5, 1-30.

Ninomiya, K., 1971: Mesoscale modification of synoptical situations from thunderstorm development as revealed by ATS III and aerological data. J. Appl. Meteor., 10, 1103-1121.

Orlanski, I., and B. B. Ross, 1977: The circulation associated with a cold front. Part I: Dry case. J. Atmos. Sci., 34, 1619-1633.

Palmén, E., and C. W. Newton, 1969: Atmospheric Circulation Systems. Academic Press, New York, 603 pp.

Pielke, R. A., 1974: A three-dimensional numerical model of the sea breeze over south Florida. Mon. Wea. Rev., 102, 115-139.

Reed, R. J., 1955: A study of a characteristic type of upper-level frontogenesis. J. Meteor., 12, 226-237.

Reed, R. J., and F. Sanders, 1953: An investigation of the development of a mid-tropospheric frontal zone and its associated vorticity field. J. Meteor., 10, 338-349.

Reed, R. J., and K. R. Hardy, 1972: A case study of persistent intense clear air turbulence in an upper level frontal zone. J. Appl. Meteor., 11, 541-549.

Roach, W. T., 1970: On the influence of synoptic development on the production of high level turbulence. Quart. J. Roy. Met. Soc., 96, 413-429.

Sanders, F., 1955: An investigation of the structure and dynamics of an intense surface frontal zone. J. Meteor., 12, 542-552.

Sawyer, J. S., 1956: The vertical circulation at meteorological fronts and its relation to frontogenesis. Proc. Roy. Soc. London, A234, 346-362.

Schaefer, J. T., 1974a: A simulative model of dryline motion. J. Atmos. Sci., 31, 956-964.

Schaefer, J. T., 1974b: The life cycle of the dryline. J. Appl. Meteor., 13, 444-458.

Shapiro, M. A., 1970: On the applicability of the geostrophic approximation to upper-level frontal-scale motions. J. Atmos. Sci., 27, 408-420.

Shapiro, M. A., 1974: A multiple-structured frontal zone jet stream system as revealed by meteorologically instrumented aircraft. Mon. Wea. Rev., 102, 244-253.

Shapiro, M. A., 1975: Simulation of upper-level frontogenesis with a 20-level isentropic coordinate primitive equation model. Mon. Wea. Rev., 103, 591-604.

Shapiro, M. A. 1976: The role of turbulent heat flux in the generation of potential vorticity in the vicinity of upper-level jet stream systems. Mon. Wea. Rev., 104, 892-906.

Shapiro, M. A., 1980: Turbulent mixing within tropopause folds as a mechanism for the exchange of chemical constituents between the stratosphere and troposphere. J. Atmos. Sci., 37, 994-1004.

Shapiro, M. A., 1981: Frontogenesis and geostrophically forced secondary circulations in the vicinity of jet stream-frontal zone systems. J. Atmos. Sci., 38, 954-973.

Shapiro, M. A., and P. J. Kennedy, 1982: Airborne radar altimeter measurements of geostrophic and ageostrophic winds over irregular topography. J. Appl. Meteor. (accepted).

Shapiro, M. A., A. J. Krueger and P. J. Kennedy, 1982: Nowcasting the position and intensity of jet streams with the Nimbus 7 total ozone mapping spectrometer. Nowcasting. Academic Press, London (in press).

Staley, D. O., 1960: Evaluation of potential-vorticity changes near the tropopause and the related vertical motions, vertical advection of vorticity, and transfer of radioactive debris from stratosphere to troposphere. J. Meteor., 17, 591-620.

Uccellini, L. W., 1975: A case study of apparent gravity wave initiation of severe convective storms. Mon. Wea. Rev., 103, 497-513.

Uccellini, L. W., and D. R. Johnson, 1979: The coupling of upper and lower tropospheric jet streaks and implications for the development of severe convective storms. Mon. Wea. Rev., 107, 682-703.

Williams, R. T., 1967: Atmospheric frontogenesis: A numerical experiment. J. Atmos. Sci., 24, 627-641.

Williams, R. T., 1974: Numerical simulations of steady state fronts. J. Atmos. Sci., 31, 1286-1296.